UTRC-R76-953200-25 COO-2277-8

UNITED TECHNOLOGIES RESEARCH CENTER
East Hartford, Connecticut

UTRC Report R76-953200-25
Semiannual Report
Under Contract E(11-1)-2277
February 1, 1976
through
June 30, 1976

Project Title: High-β Capture and Mirror Confinement of Laser Produced Plasmas

Name of Contractor: United Technologies Research Center

Reported By:

Allan F. Haught
A. F. Haught
Manager

D. H. Polk
D. H. Polk

W. J. Fader
W. J. Fader

R. G. Tomlinson
R. G. Tomlinson

Raymond A. Jong
R. A. Jong

W. B. Ard
W. B. Ard

A. E. Mensing
A. E. Mensing

T. L. Churchill
T. L. Churchill

J. H. Stufflebeam
J. H. Stufflebeam

F. J. Bresnock
F. J. Bresnock
Rensselaer Polytechnic Institute

C. R. Parsons
C. R. Parsons
Rensselaer Polytechnic Institute

MASTER

OT E(11-1)-2277
DISTRIBUTION OF THIS DOCUMENT IS UNLIMITED

Approved by:

Wayne G. Burwell
Manager of Energy Research

Date: June 30, 1976

DISCLAIMER

UTRC-R76-953200-25 C00-2277-8

Semiannual Report Under Contract E(11-1)-2277

For the Period February 1, 1976 through June 30, 1976

High-β Capture and Mirror Confinement of Laser Produced Plasmas

SUMMARY

The Laser Initiated Target Experiment (LITE) at the United Technologies Research Center is investigating the use of a dense, mirror confined, laser produced plasma as the target for an energetic neutral injection beam to create and sustain a high temperature, high density mirror confined plasma. In the LITE experiment, a dense, mirror confined target plasma is produced by high power laser heating of a ~ 100-200 μ dia. solid lithium hydride particle, electrodynamically suspended in vacuum at the center of a minimum-B magnetic containment field. The laser produced plasma expands in and is captured by a minimum-B mirror containment field. The laser produced plasma, upon capture, fills the containment volume forming a high density target for a neutral injection beam. Charge exchange collisions with the energetic beam particles further heat the confined plasma to the energy of the injected beam, and ionization of the neutral beam atoms and trapping in the mirror magnetic field act to build up the target and sustain the confined plasma against decay.

The results obtained during the current report period are presented in four technical papers which form the body of this report. Part I, Magnetic Confinement of Laser Produced LiH Plasma in LITE, by W. B. Ard, J. H. Stufflebeam, and R. G. Tomlinson, describes the time evolution and behavior of the minimum-B mirror confined plasma decay in LITE. For sufficiently high magnetic field strength, the plasma exhibits a period of quiescent decay with constant $n\tau$ for ~ 200 μsec followed by the onset of rf bursts accompanied by "dumps" of plasma out the mirrors. Fokker-Planck calculations of the plasma density decay show agreement with the measurements during the quiescent portion of the decay provided the electron temperature is assumed clamped at a low value. The rf bursts after ~ 200 μsec show only frequencies characteristic of Li ions indicating that after this time the hydrogen has been lost and the plasma is predominantly lithium. Raising the ambient gas pressure in the experiment chamber is observed to dampen the rf activity and smooth the plasma decay, indicating that warm plasma stabilization can be used to achieve increased plasma lifetimes for the LITE neutral beam injection experiments. Part II, Hot Ion Buildup by Low Current Neutral Beam Injection in LITE, by R. G. Tomlinson, W. B. Ard, W. J. Fader, D. H. Polk, A. E. Mensing, and J. H. Stufflebeam presents observations of energetic H^+ ion buildup produced by injection of a 0.2A 12 keV neutral hydrogen

beam into a mirror confined laser produced LiH plasma. Fast atom energy analyzer measurements show a rapid buildup of H^+ ions in the plasma at the energy of the injected beam to a peak value of 4.4×10^9 ions/cm^3 at ~ 50 μsec decreasing thereafter as the target plasma decays. The hot ion buildup and decay is observed over a period of ~ 200 μsec during which, from Part I, the target plasma decay is quiescent and a classical model of the target condition and injection beam interaction agrees qualitatively with the measured time history of the hot ion buildup. Further injection experiments with warm plasma stabilization for longer target lifetime and higher current beam injection will permit more detailed measurements of the hot ion buildup and represent the next phase of the LITE program. Calculations to estimate the warm plasma current necessary for stabilization of the LITE plasma and the development of a steady state ion source to supply the warm stream for the long duration experiments of interest in LITE are discussed in Part III, Streaming Plasma Stabilization Requirements in LITE, by W. J. Fader, R. A. Jong, and A. E. Mensing. The calculations are based on the quasilinear model of Baldwin, Berk, and Pearlstein and, for the conditions of the LITE target plasma, indicate that a warm plasma current of ≤ 5 amps is required for stabilization. To provide this current, the arc source of a 7 cm ORMAK ion source has been installed in the LITE facility along the axis of the magnetic containment field. Test stand operation of the source 40 amps arc current resulted in the delivery of ~ 5 amps of ~ 10 eV warm plasma at the target plasma location, and experiments feeding this plasma current into the LITE magnetic field for target plasma stabilization are now in progress. Increased neutral beam injection will be required for the next phase of injection buildup and plasma sustenance investigations in LITE, and Part IV, LITE Neutral Beam Line Upgrade, by T. L. Churchill and A. E. Mensing describes the ion source, beam line vacuum system, and power conditioning equipment being developed for these experiments. The beam line employs a 15-cm ORMAK ion source capable of delivering beam currents in excess of 15A at average energies from 10-20 keV. The beam line, designed using a self-consistent particle balance vacuum model, is pumped with a combination of oil diffusion pumps and LN_2 cooled titanium getter pumps to provide a steady state vacuum of $\leq 10^{-8}$ torr in the plasma region. The 15-cm beam line system is currently under construction and is scheduled for installation in October.

UTRC 76-98

Part I

MAGNETIC CONFINEMENT OF LASER PRODUCED LiH PLASMA IN LITE

W. B. Ard, J. H. Stufflebeam and R. G. Tomlinson
United Technologies Research Center

June, 1976

MAGNETIC CONFINEMENT OF LASER PRODUCED LiH PLASMA IN LITE

W. B. Ard, J. H. Stufflebeam, and R. G. Tomlinson

I. Introduction

In the LITE experiment, a hot, dense, plasma produced by laser heating of a ~100μ dia LiH particle is used to fill a minimum-B baseball coil mirror magnetic containment field. The confined laser produced plasma subsequently serves as the target for an energetic neutral hydrogen beam in experiments to investigate the target plasma buildup approach for creating and sustaining an equilbrium, steady state mirror fusion plasma. In the experiments, the LiH particle is positioned in vacuum at the laser beam focus by a feedback particle suspension system and heated by two sided irradiation with the focused dual beam, 50 j, 7 nsec output of a Q-switched Nd-glass laser. The energy density of the laser produced plasma is initially much greater than that of the surrounding magnetic field and the plasma expands, converting its internal energy into expansion kinetic energy and displacement of the magnetic field. As the energy density falls below that of the magnetic field, the expansion is stopped and the plasma becomes trapped, making the transition to a low beta, mirror confined plasma. This report is concerned with the properties and behavior of the plasma in the confinement stage.

II. Experimental Observations

A. Density Decay

The density decay of the confined plasma is observed with a 75 GHz microwave interferometer which measures the integrated electron density along a line through the mid-plane of the plasma perpendicular to the mirror axis (Fig. 1). For spatial resolution and to minimize the refraction effects arising from the finite geometry of the plasma the microwave beam is sharply focused and, for the ~ 6 cm transverse dimension of the confined plasma, the interferometer has a useful range from 5×10^{13} cm^{-3} to 10^{11} cm^{-3}.

The electron density is obtained from the microwave amplitude and phase shift signals using the relation:

$$n = n_c \left\{ 1 - \left[1 - \frac{\lambda}{2\pi \langle \ell \rangle} \cos^{-1} \left(\frac{V_m - 1 - T}{2\sqrt{T}} \right) \right]^2 \right\} \qquad (1)$$

where n_c is the critical density, $\langle \ell \rangle$ is the "effective plasma length", V_m is the output voltage from the mixer detector and T is the normalized transmitted power.

A computer display of n_e and phase shift ($\cos^{-1}$) versus time and the T and V_m data from which they were determined is shown in Fig. 2. The slight discontinuities in the derived density, n_e, coincident with V_m passing through a fringe are not physical but arise from small numerical discrepancies in calculating the phase shift.

Figure 3 shows the electron density decays for different containment magnetic field strengths. The electron density has been derived from the line density data under the assumption that the "effective plasma length" evolves linearly in 100 microseconds from an initial value given by the phase shift at the time the microwave signal emerges from cut-off to a final value of 5 cm observed in the luminosity photographs. The microwave signals emerge from cut-off at densities near 5×10^{13} cm^{-3} approximately 30-40 microseconds after the plasma has been created. The observed plasma density decay varies with magnetic field strength and, for the highest fields shown in Fig. 3 (10.4 kG), the density remains above 10^{12} for $\sim$ 500 microseconds. The data of Fig. 3 is replotted in terms of the classical confinement parameter, $n\tau$, in Fig. 4. For the highest magnetic field case, the decay from a density of 2×10^{13} cm^{-3} to 2×10^{12} cm^{-3} in Fig. 3 represents an interval of relatively constant $n\tau$ in Fig. 4 which does not appear for the lower field cases in Fig. 4. The measured value of $n\tau$ in this interval is $\sim 6 \times 10^{8}$ $cm^{-3}sec^{-1}$. After 200 microseconds, the value of $n\tau$ in Fig. 4 decreases rapidly for the 10.4 kG case, and the density falls exponentially with occasional sudden decreases, sometimes by as much as a factor of two, to the limit of sensitivity of the interferometer, $\sim 10^{11}$ cm^{-3}.

B. Plasma Luminosity

The luminosity of the magnetically confined plasma has a shape conforming to that of the magnetic field, as seen in Fig. 5. The microwave interferometer and charge collector probe measurements indicate a similar distribution for the plasma density. A photomultiplier camera has been developed to study the spatial and temporal development of the luminosity of the confined LITE plasma. The camera (Fig. 6) uses a 178 mm/f2.5 lens whose image is split, one appearing on photographic film as a regular camera, and the other image formed on an array of 12 fiber optic bundles which may be positioned to allow observation of different plasma locations. The fiber optic bundles are individually monitored by up to 12 photomultipliers to produce spatially and temporally resolved data of plasma luminosity in the visible wavelength region. From time integrated photographs, Fig. 5, the plasma luminosity displays a tetrahedral shape which conforms to the geometry of the baseball containment field with a center width of $\sim$ 6 cm; microwave interferometer and charge collector probe measurements indicate a similar distribution for the plasma density.

The development of the plasma luminosity observed with the photomultiplier camera upon magnetic field capture of a laser irradiated particle plasma is shown in Fig. 7. Three photomultipliers at locations 9, 5, and 2 in the plasma image as indicated on the left side of Fig. 7, are monitored in this shot; the output of each is shown on the right in Fig. 7 along with the time of the laser plasma production pulse. Photomultiplier 2 at the plasma origin, reads an initial luminosity due to illumination of the pellet by the argon ion laser of the pellet suspension system. The plasma luminosity is observed as a luminosity front which travels from the edges of the plasma toward the center. From a series of data runs with various combinations of positions monitored, the luminosity front travels four times faster in a direction along the magnetic field lines than in a direction normal to the magnetic field. The front reaches the center of the plasma in approximately 150 microseconds and the subsequent plasma luminosity thereafter decreases smoothly with the plasma decay.

Spectral resolution of the plasma luminosity is achieved with a 1 meter grating spectrometer with spatial resolution provided by controlling the position of the plasma luminosity image on the slit as illustrated in Fig. 8. The spectrum of the LITE plasma was obtained from 3800 Å to 6200 Å and is presented in Fig. 9. Extension of the spectral measurement into the ultra-violet was limited by the transmission of the glass used in the vacuum viewing ports. The spatial resolution provided by the slit showed two regions of interest: the plasma core $\sim$ 3 mm in diameter, and surrounding the core the remaining plasma volume whose boundary displays the characteristic fan shape of the minimum-B baseball coil. The data shows intense bremsstrahlung radiation in the plasma core along with higher ionization levels of lithium (Li^{++}, 4500 Å). Various impurity lines, predominantly O^+, are also observed in the core along with the second harmonic of the high power neodymium laser at 5300 Å and a number of lines of the argon ion laser used for particle suspension. In the outer region which comprises the majority of the plasma volume, the radiation consists almost entirely of two spectral lines, Li^+ (5485 Å) and Li (6103 Å). This indicates a much cooler outer region than the plasma core and identifies the components present in the luminosity measured with the photomultiplier camera.

The time dependence of the intense Li^+ radiation at 5485 Å was measured by photomultiplier observation of the spectrometer output with the spectrometer slit moved approximately 2 cm to the left of the plasma center, i.e., equivalent to fiber optic location 6, of Fig. 6. The results obtained are shown in Fig. 10 along with the total luminosity at position 6, taken with the photomultiplier camera. Both traces peak in intensity in approximately 70 μsec and display the same waveform as would be expected from the predominance of 5485 Å radiation in the outer plasma spectrum of Fig. 9.

C. Ion Energy Distribution

A fast atom energy analyzer has been used to determine the ion energy distribution in the magnetically confined plasma from measurements of the energy distribution of fast neutrals born in the plasma through recombination and charge-exchange of the confined ions. As shown in Fig. 1, the analyzer consists of a gas ionizing cell and a parallel plate electrostatic analyzer with an entrance angle of 45°. The fast neutrals are reionized in the gas cell and detected in four energy channels in the analyzer. The energy analyzer views the plasma through $\sim 1\ \mathrm{cm}^2$ cross section collimating tube along a line in the mid-plane orthogonal to the mirror field axis. The detector line is slightly displaced (~ 1 cm) from the center of the plasma to avoid saturation of the detectors by energetic photons produced during the laser plasma production. The gas stripping cell is 10 cm long and is normally operated with N_2 at a pressure of $2\text{-}4 \times 10^{-3}$ torr. The four energy channels are .6 qV, .9 qV, 1.2 qV and 1.5 qV where V is the voltage on the analyzer plates. The plates have been operated with up to 12 kV on the plate to detect ions with energies as high as 18 keV.

With the stripping cell evacuated, the energy analyzer has been used to examine the ion distribution of the freely expanding plasma in the absence of a magnetic field. Although the electrostatic energy analyzer only separates ions of the same energy per unit charge, in a free expansion, the charge to mass ratio of the ions can be measured since the ion velocity can be determined from the flight time from the origin to the analyzer. Since the response of the detectors to a delta function of charge is known to be a very fast rise in output voltage and a 10 μsec exponential decay, the detector output can be unfolded to give the input current.

Figure 11a shows the energy analyzer response in three energy channels along with the ion signal from a total current collector. The time scale for this total ion signal has been adjusted to account for the fact that the current collector was located closer to the initial plasma than the energy analyzer. From the energy response of the different channels and the time at which the ions arrive at the detector, the four peaks of the energy analyzer waveforms can be identified from left to right as H^+, Li^{+++}, Li^{++} and Li^+. All four different ion species are observed in each energy analyzer channel and the envelope of the signals in each channel roughly follows the envelope of the total current. In Fig. 11b the signals of the three energy channels in 11a are summed and compared with the total current waveform. Since the amplitudes of the signals in all the channels follow the amplitude of the total current in time, the velocity distribution of all four of the species is the same, and the mean energy of the Li ions in the free expansion plasma is therefore about 7 times the mean energy of the H^+. In this particular shot the peak energy of Li ions is ~ 6 keV and the H^+ energy is ~ 1 keV.

With the confining magnetic field on, only neutral particles can reach the energy analyzer. Some of the fast neutrals are ionized in the gas cell in front of the analyzer and bent by the deflection plates into the collector. The neutrals arriving at the analyzer can be H^o or Li^o, and since the time scales for neutral fluxes are much longer than the flight times of the fast neutrals, the different atoms cannot be distinguished in the analyzer. The time dependence of the neutral flux during the confined plasma decay has been measured over the range from 300 eV to 18 keV. Figure 12 shows the detector outputs at 300, 600, and 750 eV from one shot and the outputs from another plasma decay at 1.8, 3.6, and 4.5 keV. The detector gains are the same for both shots. In general, the lower energy outputs are characterized by a large initial flux which decays in 100 μsec and a lower level flux that continues for several hundred μsec. The higher energy signals increase with time, reaching a peak at about 75 μsec, and gradually decrease over several hundred microseconds. The fast neutral flux to the energy analyzer is consistent with a plasma composed of both a low temperature, short-lived component and a much higher temperature, long-lived component. If the assumption is made that most of the flux below 1 keV for the first 100 μsec is H^o, we can determine the energy distribution of the H^+ ions at different energies calculated from the neutral flux. The plot is obtained by correcting the output of the detectors for the probability of charge exchange of H^+ in the plasma and the probability of reionization of the H^o in the gas cell as a function of energy (Ref. 3). The distribution function of Fig. 13 gives a temperature of about 300 eV for the confined H^+ ions. The spectral measurements and the rf observations discussed below indicate that the higher energy, long-lived component of the neutral flux is probably due to Li^+ ions. The charge exchange and ionization cross sections for Li^+ are not as well known as for H^+, but the detector outputs at higher energies indicate a temperature of about 2 to 4 keV for the Li^+ ions in the plasma. The plasma also contains Li^{+++} and Li^{++} ions; however, since these ions cannot reach the analyzer through a one-step process such as charge exchange or recombination, their temperature or relative density cannot be inferred from the measurements.

The outputs of the energy analyzer in the higher energy channels sometimes show fast drops in signal at later times. These losses in signal are always correlated with decreases in electron density measured by the microwave interferometer. However, all the sharp density drops observed in the interferometer output do not show up as loss of signal in the energy analyzer outputs. When ions are lost in these dumps, they are predominantly in the energy range from 1 to 3 keV. In fact, the energy analyzer often shows increased signals at energies below 1 keV when dumps occur. These phenomena are correlated with rf activity in the plasma.

D. rf Oscillations

Two probes placed in the mirror throat are used to monitor rf activity in the plasma. The probes are located in the fan at the mirror points about 6 cm on either side of the field axis. The probes are small coaxial conductors with the center conductor connected to a small 1/8" dia. disc. The probes are terminated with 50Ω and coupled to a 50Ω terminated line through a .01 μf coupling capacitor.

The nature of the signals observed with the rf detectors changes during the course of the plasma decay. During the first 200 μsec of the decay, rf activity is generally not observed, but when oscillations do occur they appear to be more or less continuous. Some time after 200 μsec, bursts of rf are always seen. In general, the bursts last a few microseconds and are associated with abrupt drops in the plasma density observed on the microwave interferometer and fast atom energy analyzer and with increases in the current to the charge collectors in the fan. The correlated outputs of the fast atom energy analyzer, electron density decays and signals on the rf probe for two different shots are shown in Fig. 14.

The four shots of Fig. 15, each taken with low (<< 10^{-5} torr) background pressure, illustrate the four characteristic frequencies observed during the plasma decay. The upper trace in each photograph indicates the time dependence of the rf activity while the lower trace in each photograph shows the expansion of a small section of the upper trace. The continuous oscillations sometimes present during the period from about 50 μsec to 150 μsec have a dominant frequency of 17 to 18 mc. The frequencies present in the bursts which occur after 200 μsec fall into three groups with average frequencies of 2.7, 5.9 and 8.7 mc. Often the waveforms observed in the bursts consist of two or all three of these frequencies. Although the different frequencies are not exact harmonics, they are all within 10 percent of the ion cyclotron frequency of Li^+, Li^{++}, Li^{+++} or H^+ at the magnetic field strength of the central field. In these experiments the center field strength is 12,000 Gauss, and the corresponding cyclotron frequencies are 2.6, 5.2, 7.8 and 18.2 mc. Experiments at 25 percent lower field strength (9.3 kG) give frequencies about 25 percent lower indicating that the oscillations are closely related to ion cyclotron frequencies.

The change in slope of the density decays and the sharp drop in density observed with the microwave interferometer are always accompanied by the rf bursts. In comparing shots in which the frequency of the bursts are determined, the following observations were made: if the frequency of the rf burst is characteristic of Li^{+++} or Li^{++}, the total electron density drops but no change is observed in the energy analyzer outputs. If the frequency is the Li^+ cyclotron frequency the dumps are observed both in the electron density and the energy analyzer. Oscillations characteristic of H^+ cyclotron frequencies were only observed before 150 μsec and never in the form of bursts. On those shots which do contain the H^+ cyclotron frequency, the bursts of Li ion cyclotron frequency which occur later are of unusually large amplitude and accompanied by large drops in density.

The amplitude of the oscillations is affected by neutral background pressure; the amplitude being greatly attenuated for pressures above 1×10^{-5} torr as shown in Fig. 16. At pressures above 10^{-5} torr, rf bursts are barely detectable, and the decay rate of the plasma after 200 μsec is greatly reduced and smooth with no large dumps of plasma.

III. Discussion of Results

The combined microwave interferometer, plasma light emission, fast atom energy analyzer, and rf oscillation measurements provide an internally consistent characterization of the magnetically confined, laser produced, LiH plasma in LITE. The most apparent feature is the time dependence of the density decay shown in Fig. 3. For sufficiently high magnetic field strength, the plasma exhibits a period of quiescent decay with constant $n\tau$ for ~200 μsec followed by the onset of rf bursts accompanied by "dumps" of plasma out the mirrors. This is very similar to the behavior of the plasma reported in earlier 2XII, PR-6, and PR-7 experiments (Refs. 4, 5, 6) although the filling of the mirror fields and the initial density, composition, and energy distribution of the plasmas is quite different in these experiments.

Theoretical calculations of the plasma density decay using the HYBRID two-dimensional and ISOTIONS one-dimensional Fokker-Planck codes (Ref. 1) show agreement with the microwave interferometer measurement during the quiescent portion of the decay provided that the electron temperature is assumed to be clamped at a low value. The density decay data for the high field (10.4 kG) case of Fig. 3 is compared in Fig. 17 with the density decay calculated using ISOTIONS with the electron energy clamped at 25 eV.

The model used in the calculation assumes that the initial mean energies of the H^+ and Li^{+++} components of the plasma are 254 eV and 1771 eV, respectively, in agreement with the measured energies of these components in the free expansion (no magnetic field) experiments. The clamped electron temperature in the model results in sufficient energy drag on the ions to prevent hardening of the energy distribution. The lower energy H^+ component rapidly scatters out of the plasma, and the plasma composition becomes dominated by the higher energy Li^{+++}. The fast atom energy analyzer data clearly shows the presence of a low energy short-lived component (~ 300 eV) and a high energy, long-lived component (~2-4 keV). Although only H^+ or Li^+ ions are monitored by the energy analyzer, the Li^+ component, which most likely is produced from charge exchange interactions of Li^{+++}, should reflect the energy distribution of the Li^{+++} component from which it originated. The observation that rf activity after 150 μsec shows only frequencies characteristic of Li ions supports the conclusion that after this time the plasma is predominantly Li.

The appearance of rf bursts with the Li^+ cyclotron frequency, correlated with drops in total electron density and corresponding drops in the high energy component of the energy analyzer outputs, indicates that the decaying Li plasma ultimately evolves to a plasma dominated by Li^+ ions. The larger scattering rate of the higher charge states is expected to cause the distribution to evolve toward the lower charge states (at low electron temperatures the probability of reionization of the Li^+ to the higher charge states becomes small).

Although the ISOTIONS model and the fast atom energy analyzer measurements suggest that the H^+ component of the plasma is very quickly lost from the plasma, frequencies characteristic of the H^+ cyclotron frequency are occasionally observed early in the decay. For those plasmas in which the H^+ oscillations are seen, the overall behavior of the decay has characteristics quite distinct from those where the H^+ frequency is absent as evidenced in Fig. 14. The Li rf bursts which occur after 200 μsec are, in general, larger in amplitude and the amount of plasma lost during a burst is much greater for decays that exhibited H^+ oscillations than for those which did not. Since increasing the initial background pressure has been shown to decrease the amplitude of the rf bursts and to decrease the amount of plasma lost in the dumps, it is likely that the variations observed in the plasma behavior without initial filling pressure are the result of variations in the amount of wall reflux in different shots. Incomplete ionization of the LiH particle could result in a large charge exchange rate in the freely expanding plasma and a large flux of fast atoms to the surfaces of the magnet near the plasma. It would appear therefore that the increased losses are obtained for a particularly energetic laser produced plasma which is more completely ionized, has a lower neutral density in the confined plasma, and possibly a higher electron temperature as well. This is consistent with the observations that the prompt neutral flux to the fast atom energy analyzer is smaller in these shots and the low energy component, probably H^+, lasts longer and has a higher temperature.

IV. Conclusions

It has been determined (Refs. 4, 5, 6) that the initial period of quiescent decay in PR-6, and PR-7 and the early 2XII experiments was established by inadvertent warm plasma stabilization due to the presence of plasma from the plasma injectors in the loss cones and that the plasmas experienced enhanced losses due to the DCLC (Drift Cyclotron-Loss Cone) instability when this stabilizing plasma decayed. The LITE experiment has no external plasma source but may experience some self-stabilization by plasma created in the mirror loss cones during the initial plasma production, capture, and confinement. The inward propagating luminosity wave observed in LITE appears to arise from wall reflux which may serve both as a mechanism for clamping the electron temperature and for introducing warm stabilizing plasma in the loss cones to establish the period of quiescent decay. Early quasi-CW rf activity at the H^+ cyclotron frequency, occasionally observed, does not appear to result in significant plasma loss from LITE, either because the H^+ component has already become a small fraction of the total plasma or because, as in PR-6 (Ref. 5), the regular oscillations are not associated with plasma losses. The later rf bursts at the Li^+, Li^{++} and Li^{+++} ion cyclotron frequencies are associated with plasma "dumps" observed both in the electron and hot ion densities. Raising the ambient gas pressure in the experiment chamber dampens the rf activity and smooths the plasma decay, indicating that warm plasma stabilization can be expected to yield longer-lived plasmas. On the basis of these results, the arc source of a 7-cm ORMAK ion source is being installed in the LITE facility along the axis of the magnetic field for application of the streaming plasma stabilization technique to the multi-species LiH plasma and to provide long duration stabilization for steady state injection sustenance investigations in LITE.

References

1. Haught, A. F., D. H. Polk, W. J. Fader, R. G. Tomlinson, R. A. Jong, W. B. Ard, A. E. Mensing, T. L. Churchill, J. H. Stufflebeam, F. J. Bresnock: High Beta Capture and Mirror Confinement of Laser Produced Plasmas, UTRC R76-953200-24, COO-2277-7, Semiannual Report, Jan., 1976, prepared under Contract E(11-1)-2277 for the U.S.E.R.D.A..

2. Mattioli, M. and D. Vernon, Plasma Physics, 11, 684, 1969.

3. Barnett, C. F., and J. A. Ray, Nuclear Fusion, 12, 65, 1972.

4. Coensgen, F. H., W. F. Cummins, A. W. Molvik, W. E. Nexsen, T. C. Simonen, and B. W. Stallard, Plasma Physics and Controlled Nuclear Fusion, 1, IAEA, Vienna, 323, 1975.

5. Baiborodov, Yu. T., M. S. Ioffe, B. I. Kanaev, R. I. Sobolev, and E. E. Yushmanov, Plasma Physics and Controlled Nuclear Fusion Supplement, IAEA, Madison, 219, 1972.

6. Gott, Y. V., M. S. Ioffe, B. I. Kanaev, A. G. Motlich, V. P. Pastukhov, and R. I. Sobolev, Plasma Physics and Controlled Nuclear Fusion Supplement, IAEA, Vienna, 55, 1975.

List of Figures

DIAGRAM OF MICROWAVE INTERFEROMETER AND FAST ATOM ENERGY ANALYZER POSITIONS

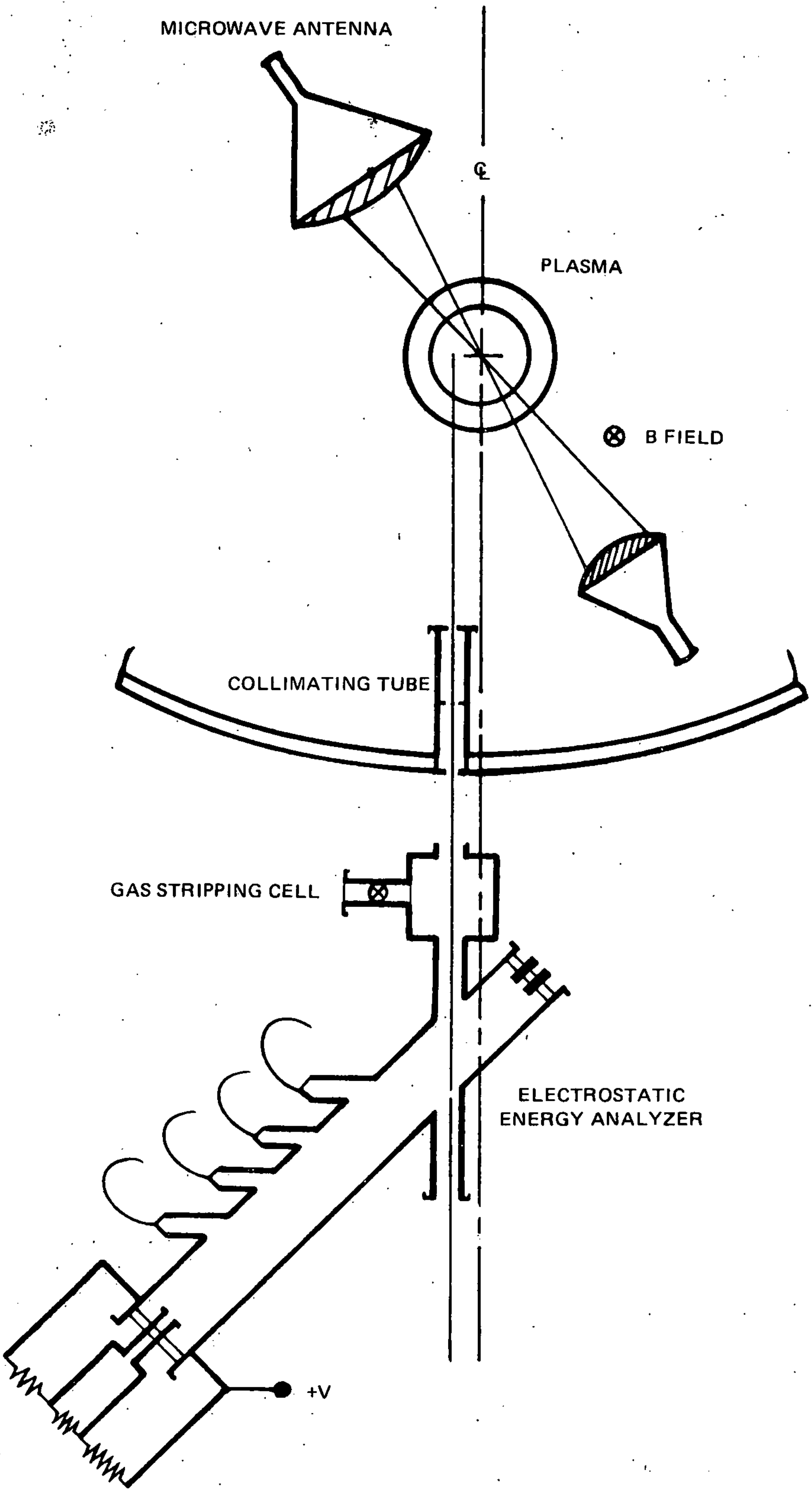

FIG. 2

MICROWAVE INTERFEROMETER SIGNALS

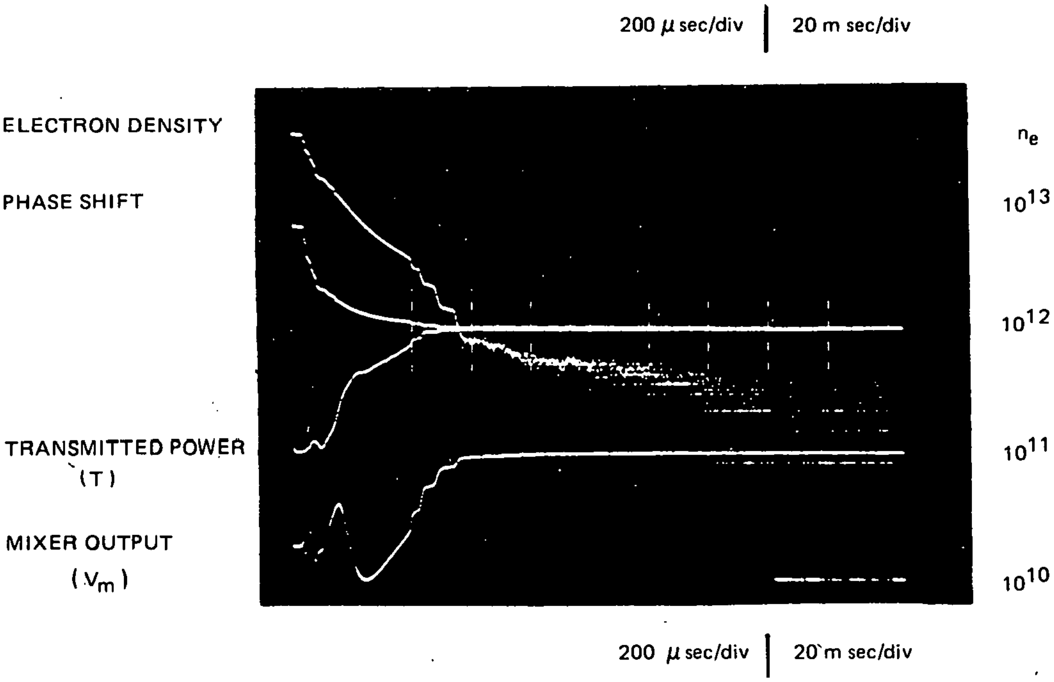

FIG. 3

PLASMA ELECTRON DENSITY VS TIME

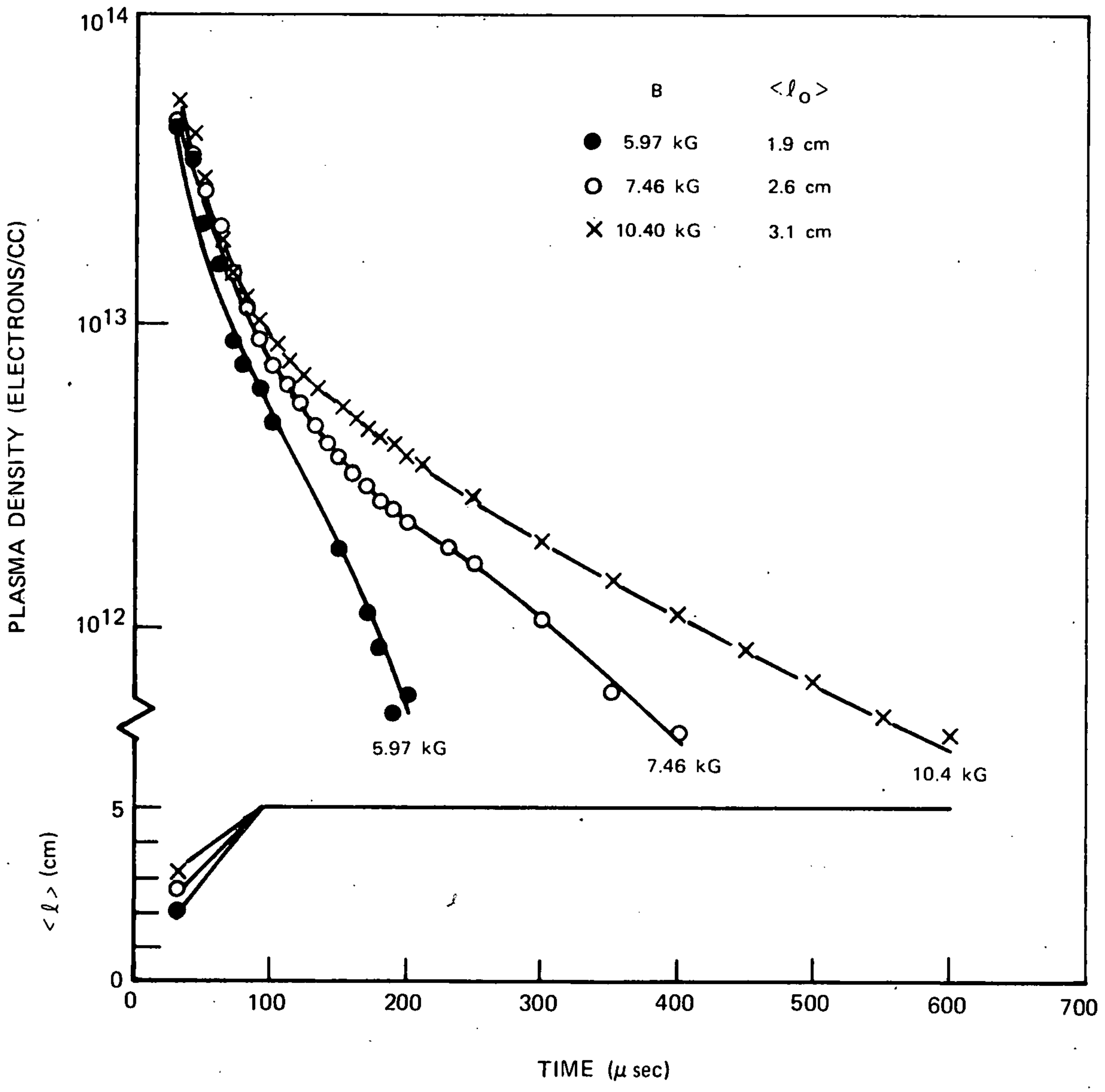

nτ VS TIME

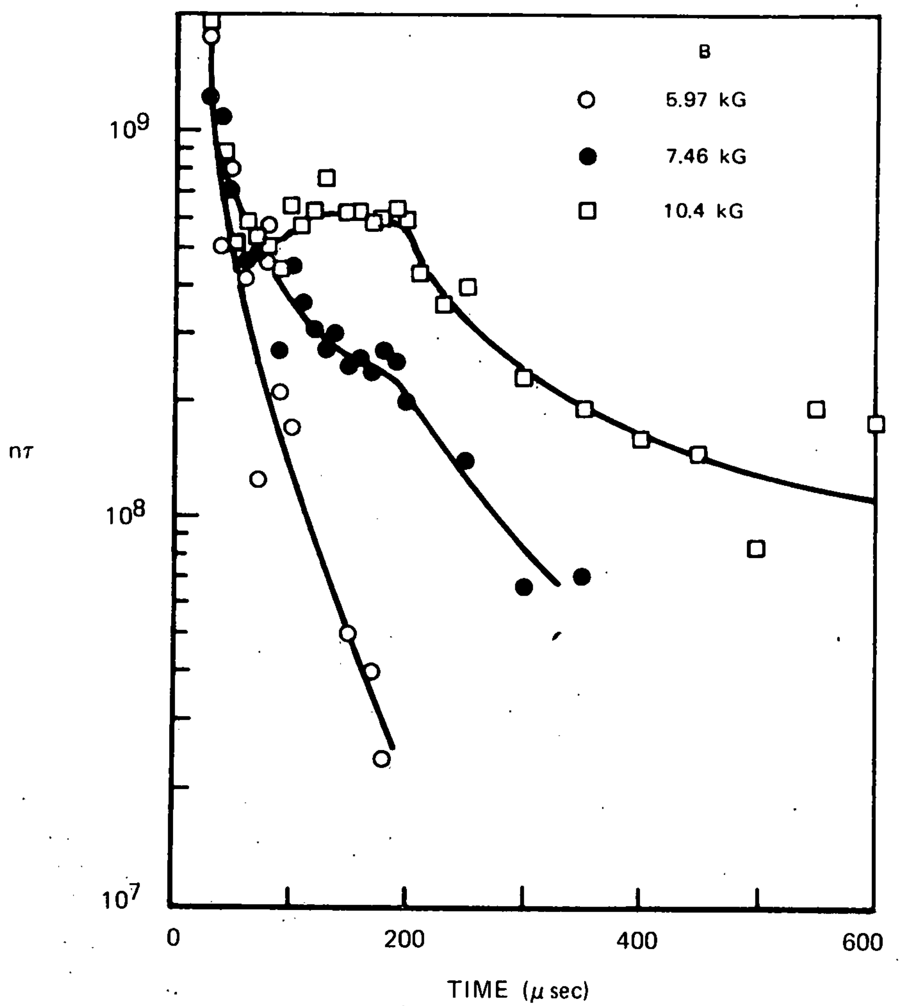

PLASMA GEOMETRY

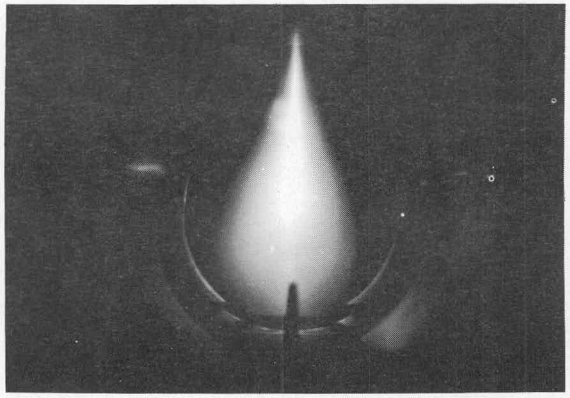

PLASMA LUMINOSITY

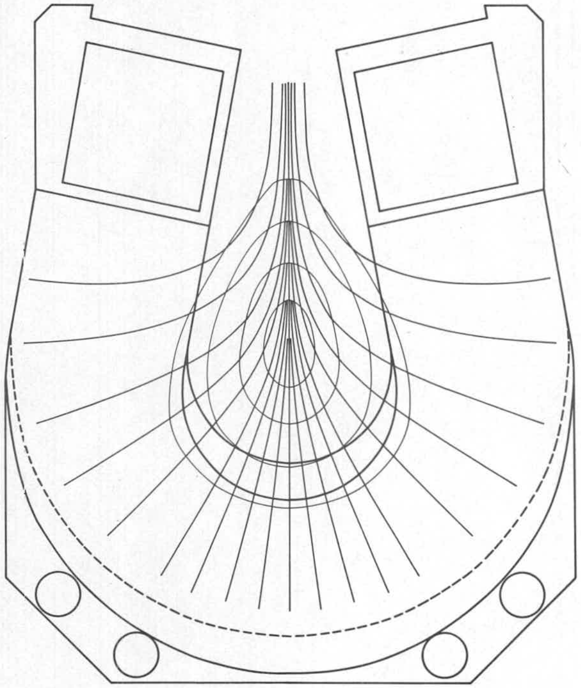

FIELD CONFIGURATION

0 5 10

CM

FIG. 5

PHOTOMULTIPLIER CAMERA

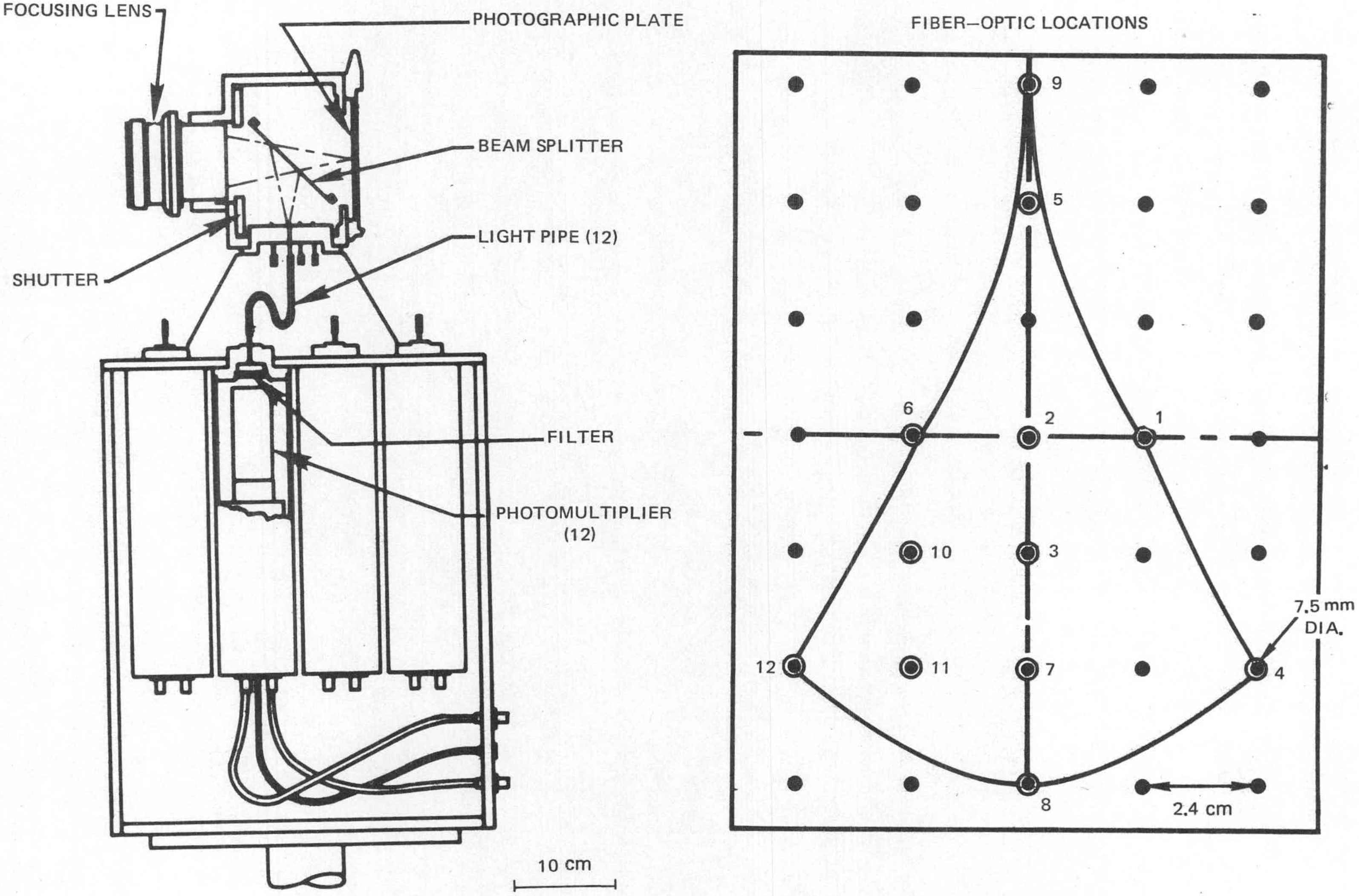

FIG. 6

76–06–264–1

PHOTOMULTIPLIER CAMERA DATA

SHOT # 903

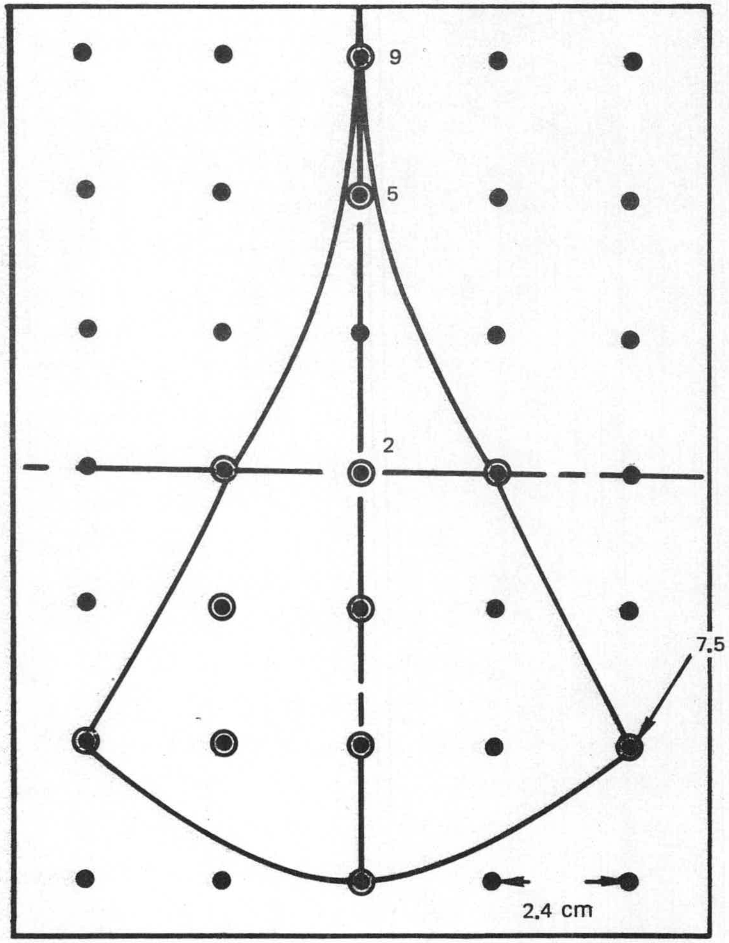

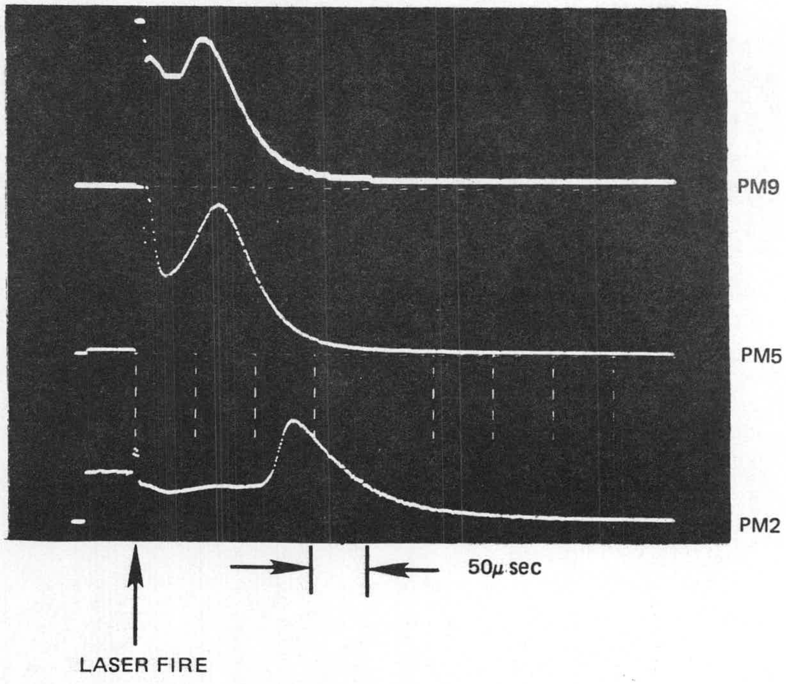

$V_{9,5} = 2 \times 10^5$ cm/sec

$V_{5,2} = 9 \times 10^4$ cm/sec

76–06–264–2

FIG. 7

FIG. 8

SPECTROGRAPH SLIT LOCATION

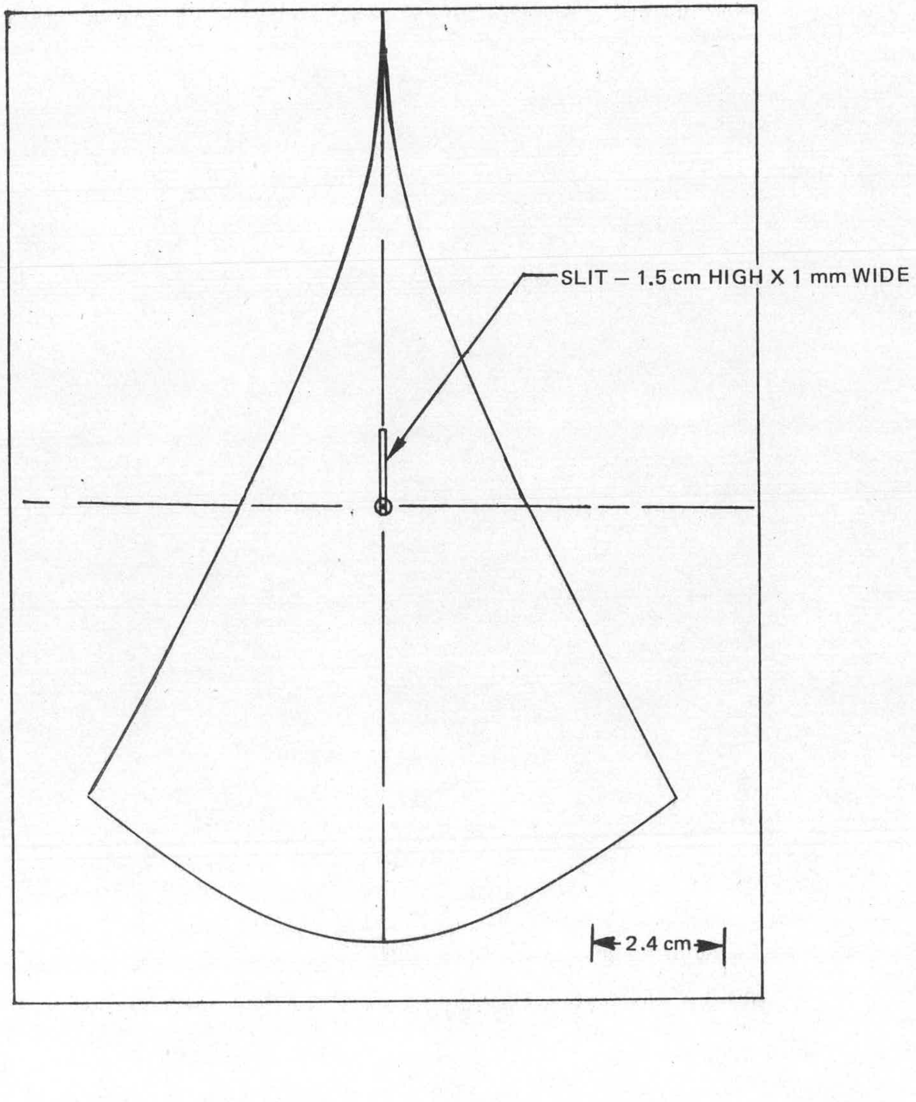

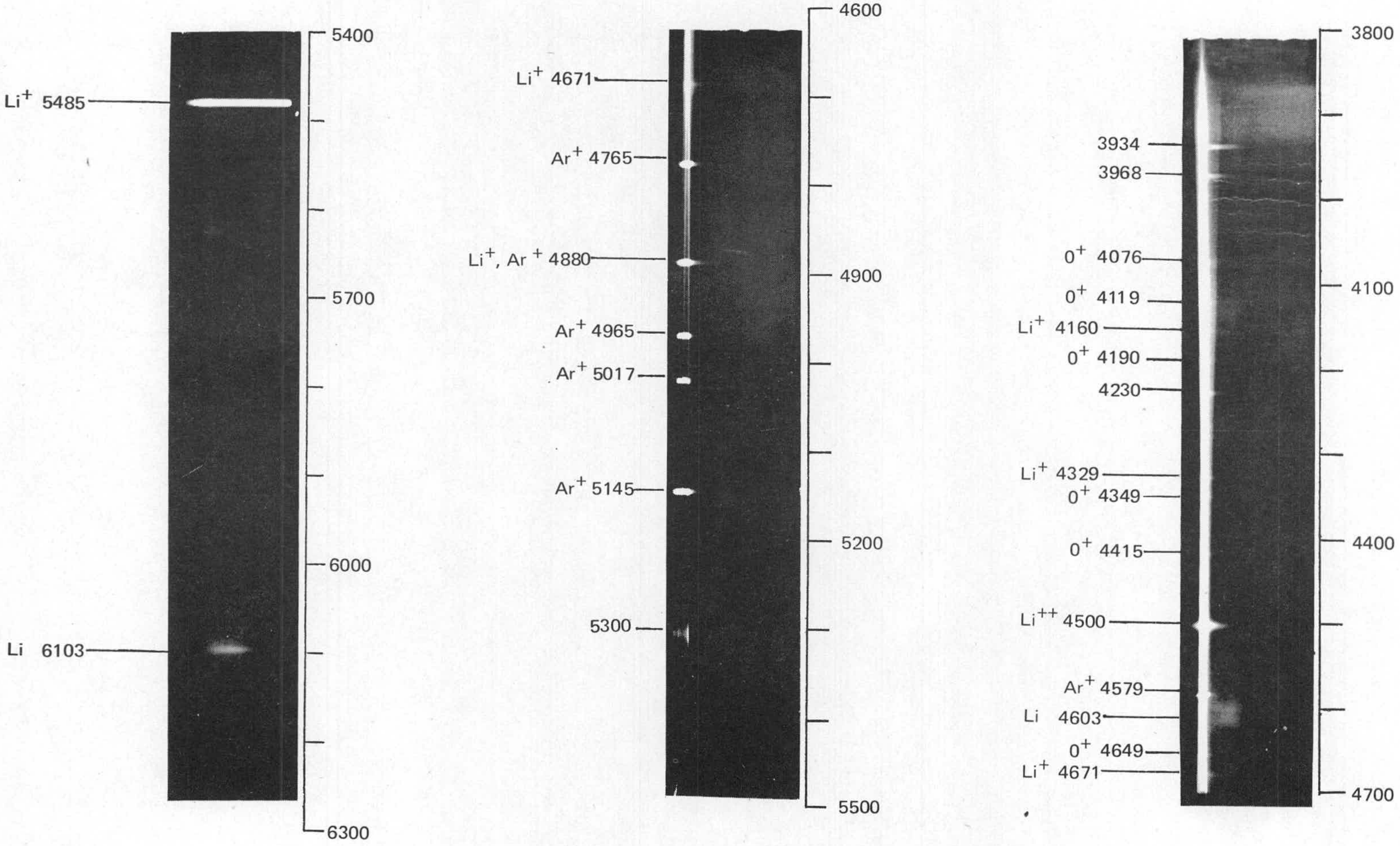

SPECTRUM OF LITE PLASMA

FIG. 9

TIME EVOLUTION OF Li^+ RADIATION

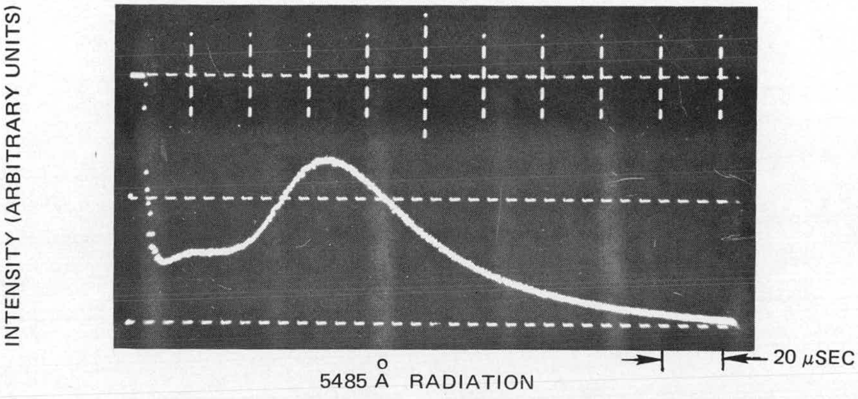

5485 Å RADIATION

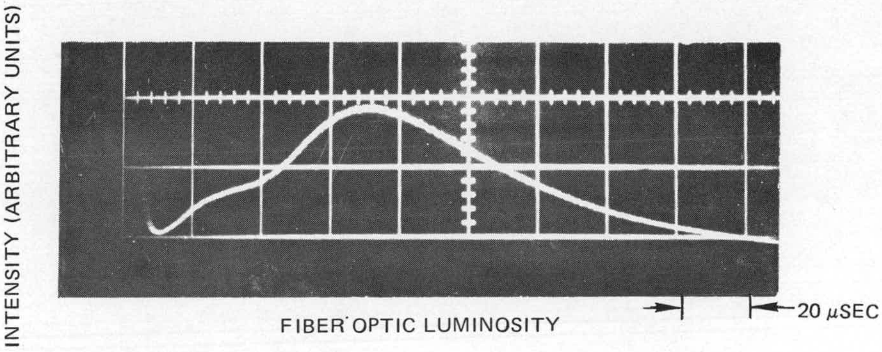

FIBER OPTIC LUMINOSITY

FIG. 11

FAST ATOM ENERGY ANALYZER SIGNALS FOR FREE EXPANSION LiH PLASMA

FIG. 11a

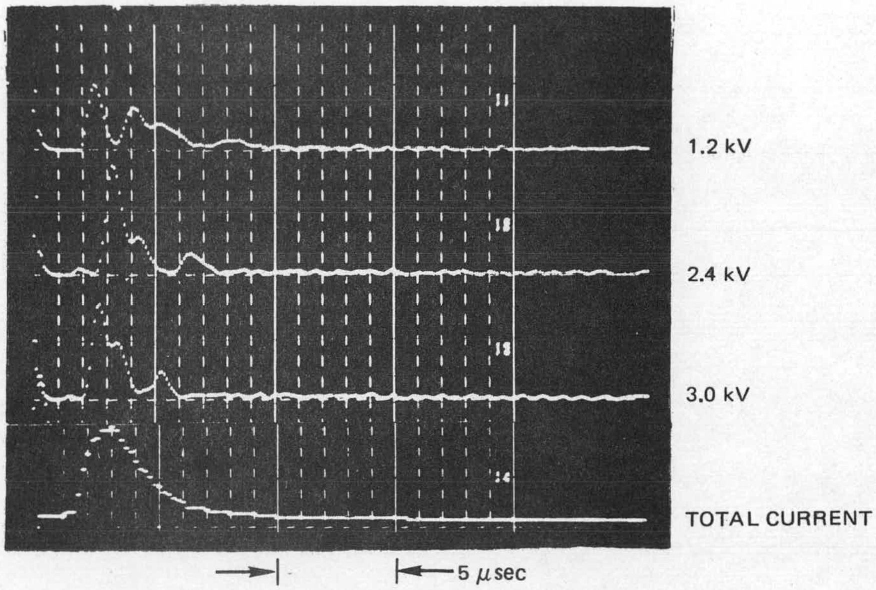

FIG. 11b

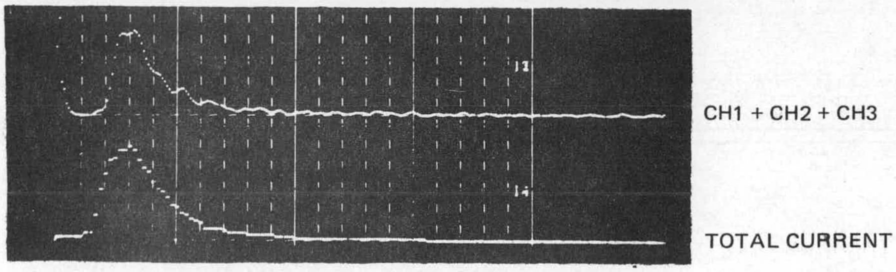

76–06–234–1

FIG. 12

FAST ATOM ENERGY ANALYZER SIGNALS
FOR CONFINED LiH PLASMA

FIG. 12 a

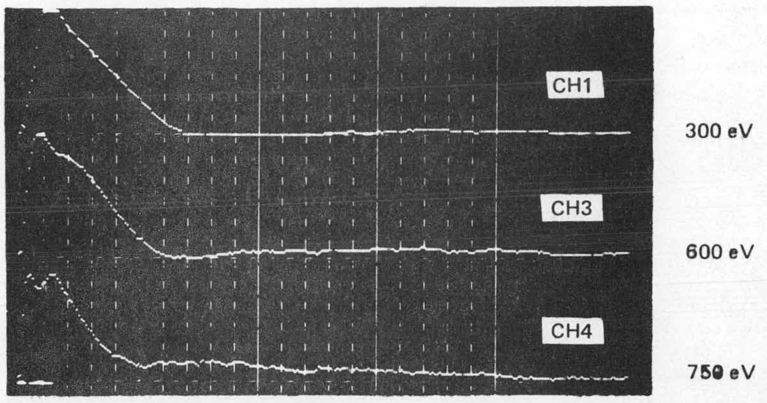

FIG. 12 b

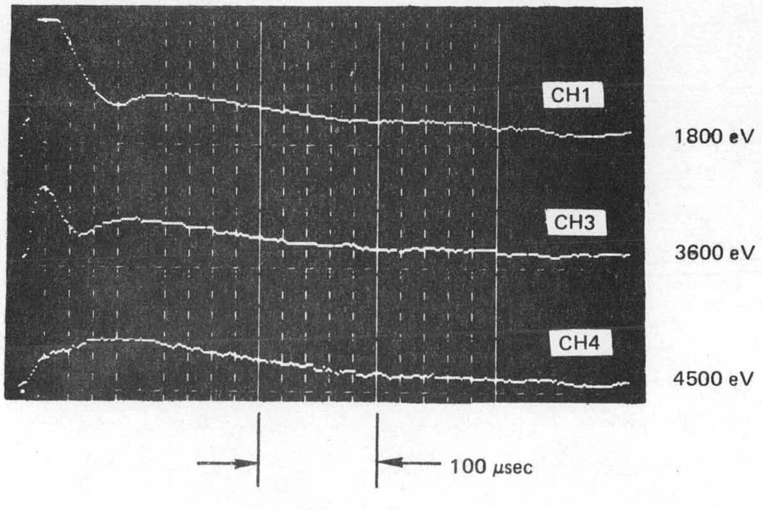

76–06–200–1

RELATIVE ENERGY DISTRIBUTION OF HYDROGEN IONS IN PLASMA

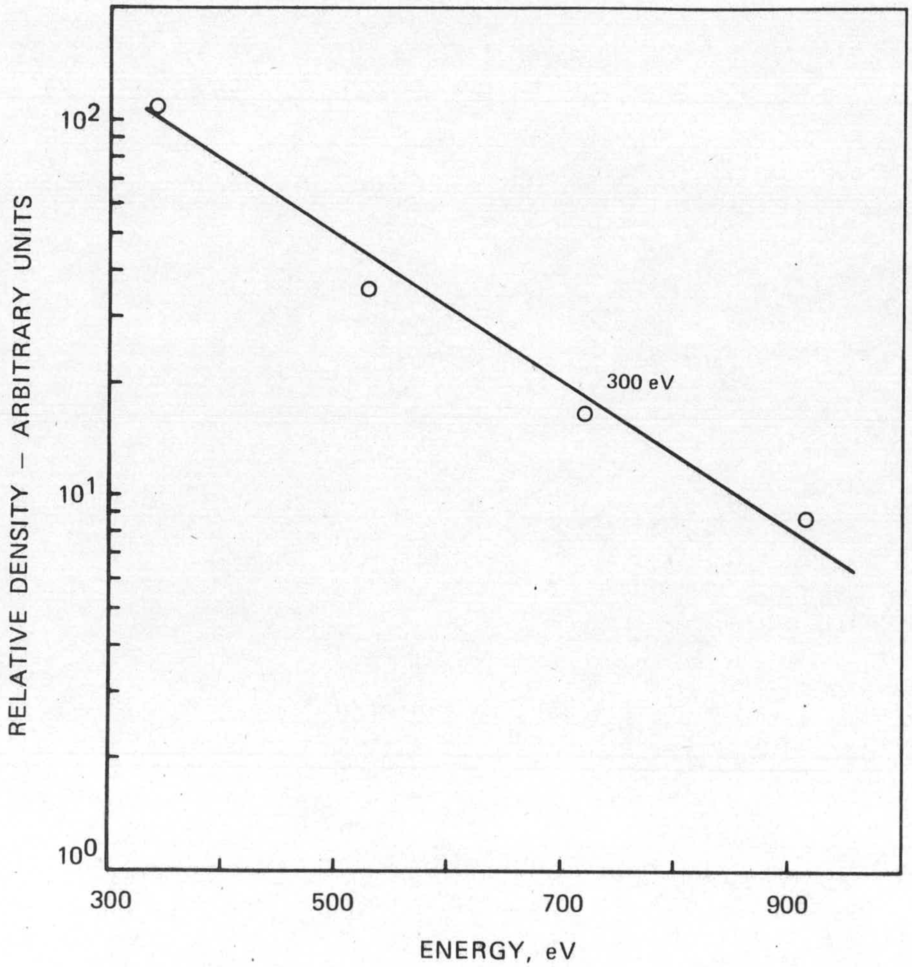

FIG. 14

FAST ATOM ENERGY ANALYZER SIGNALS, ELECTRON DENSITY DECAYS AND RF SIGNALS FROM TWO SHOTS

SHOT #2247

ENERGY ANALYZER OUTPUT

SHOT #2234

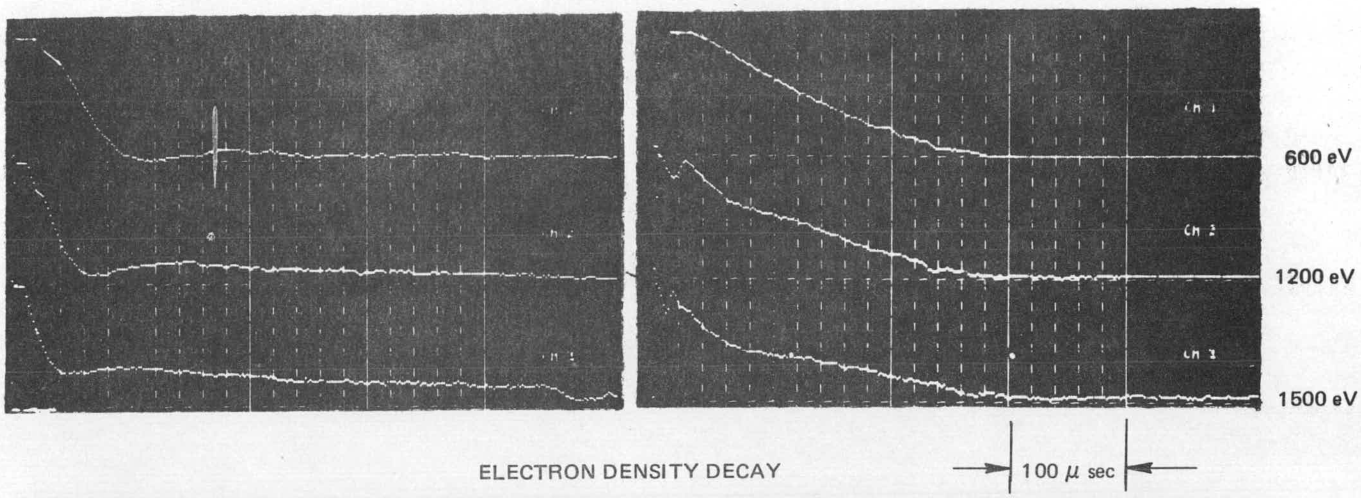

ELECTRON DENSITY DECAY

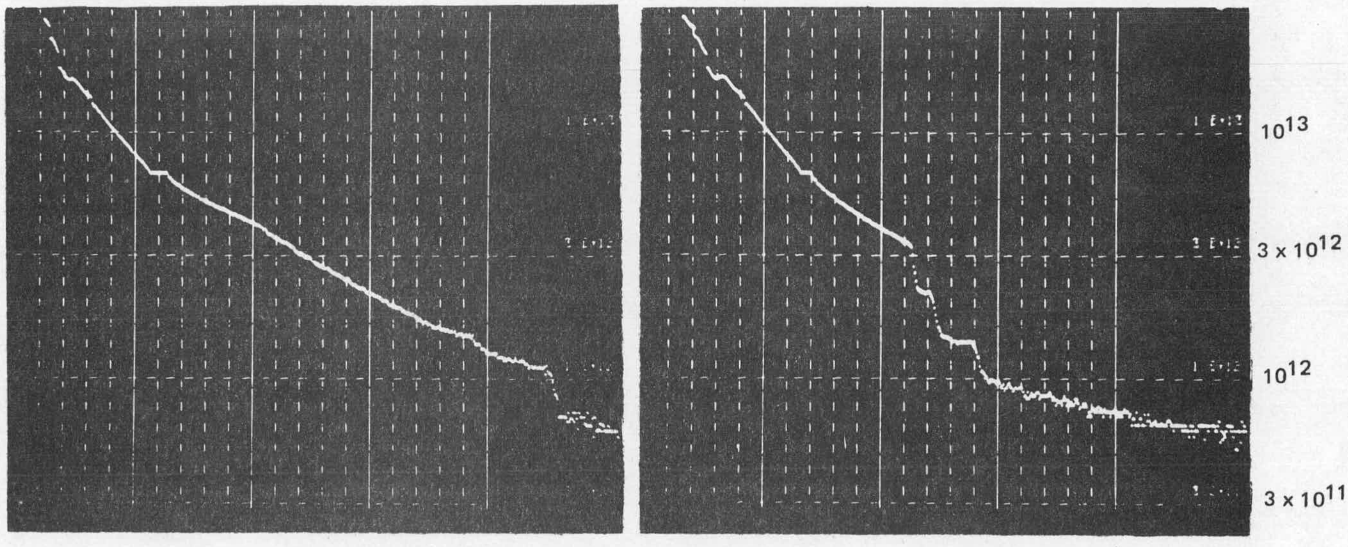

UPPER TRACE – RF PROBE SIGNAL
LOWER TRACE – 2 μsec EXPANSION OF UPPER TRACE

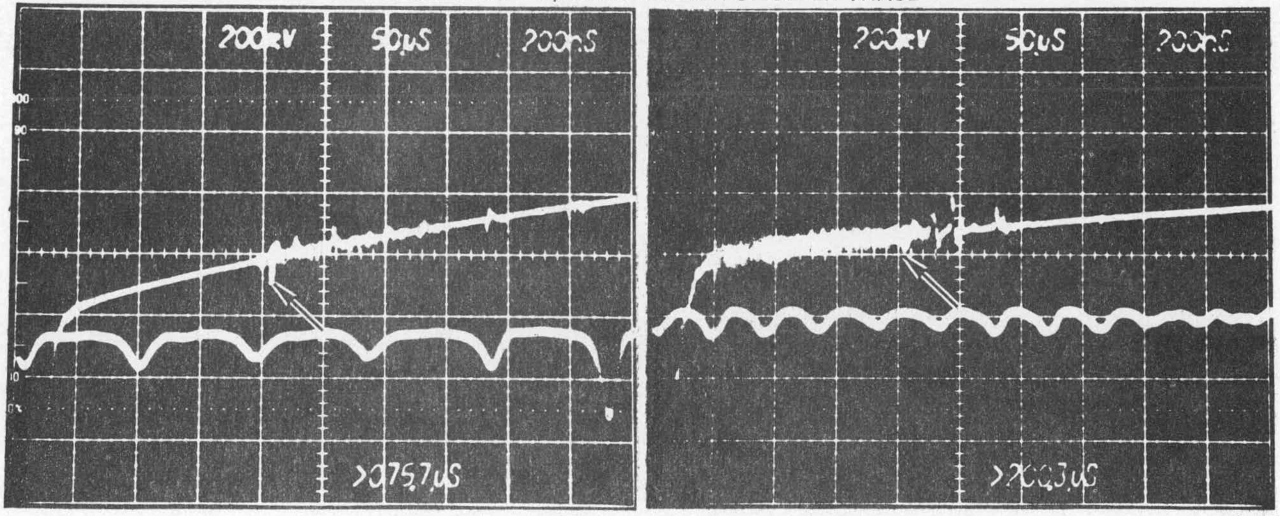

76–06–238–2

FIG. 15

RF SIGNAL AND ELECTRON DENSITY DECAY AT
HIGH BACKGROUND PRESSURE

SHOT #2089

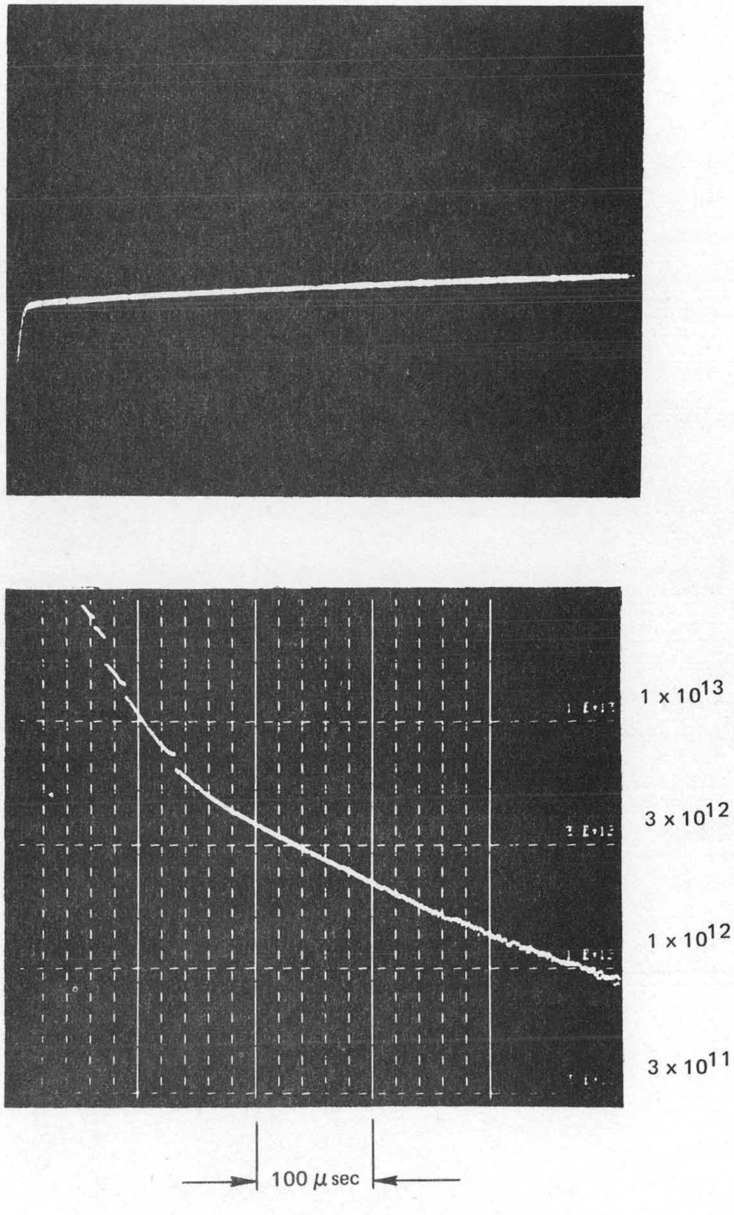

FIG. 16

RF SIGNALS SHOWING FOUR CHARACTERISTIC FREQUENCIES

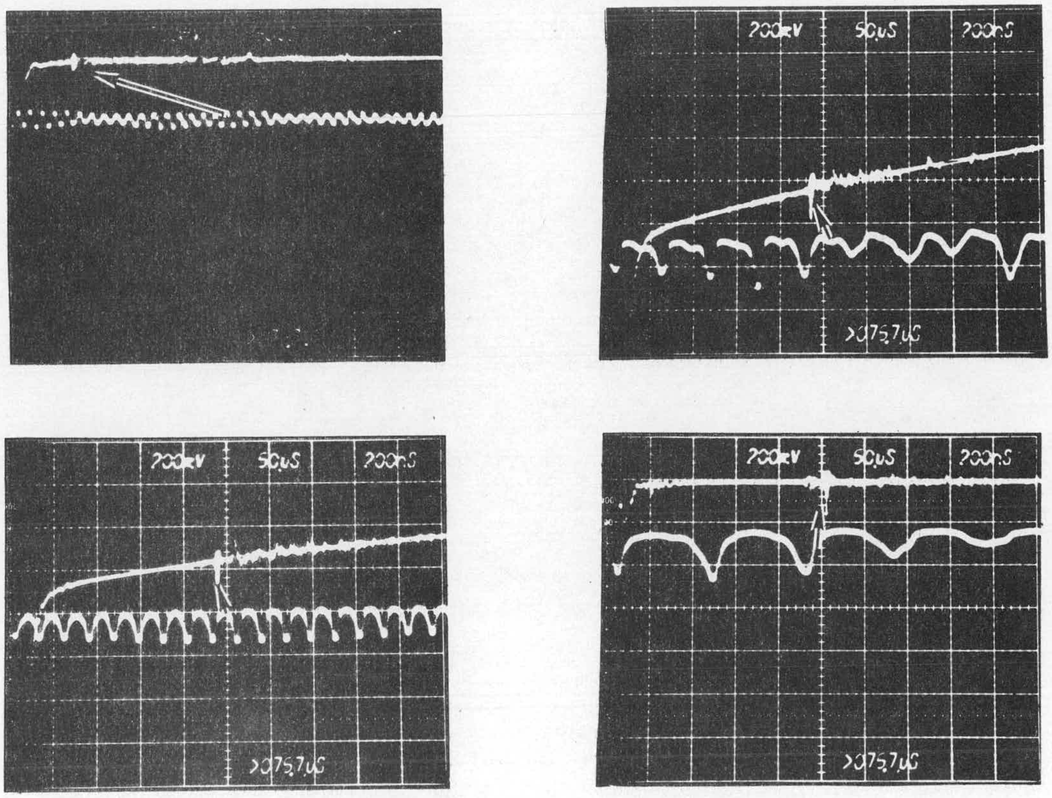

FIG. 17

EXPERIMENTAL ELECTRON DENSITY AND CALCULATED ELECTRON AND HYDROGEN DENSITIES

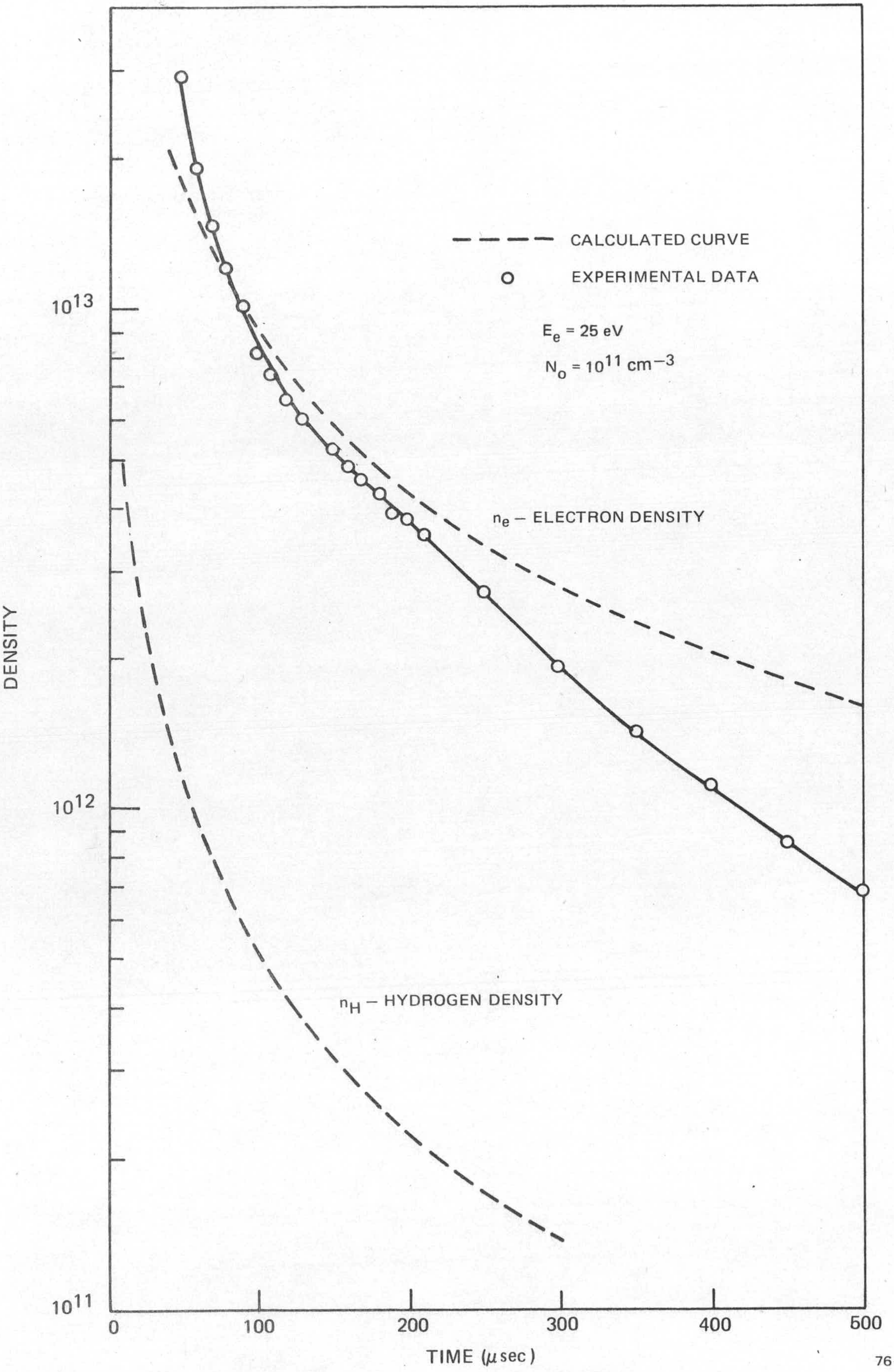

76–06–198–5

UTRC 76-95

Part II

HOT ION BUILDUP BY LOW CURRENT NEUTRAL BEAM INJECTION IN LITE

R. G. Tomlinson, W. B. Ard, W. J. Fader, D. H. Polk,
A. E. Mensing, and J. H. Stufflebeam
United Technologies Research Center

June, 1976

HOT ION BUILDUP BY LOW CURRENT NEUTRAL BEAM INJECTION IN LITE

R. G. Tomlinson, W. B. Ard, W. J. Fader, D. H. Polk,
A. E. Mensing, and J. H. Stufflebeam

I. LITE Target Plasma

The laser produced target plasma confined in the LITE minimum-B mirror magnetic field is shown in Fig. 1 along with a drawing of the confinement field line configuration. The plasma is generated by two beam, 1.06 micron, Nd-glass laser irradiation of LiH particles ~ 100 microns in diameter producing a plasma of $\sim 10^{16}$ hydrogen and lithium ions which expands in and is captured by the "baseball" confinement field. The plasma luminosity displays a plasma configuration which corresponds to the magnetic field geometry and indicates a plasma volume of $\sim 400\ \mathrm{cm}^3$. Probe and microwave measurements confirm the plasma distribution indicated by the luminosity photographs. Charge collector probes located at a series of positions over a 120° arc in the mirror fan permit simultaneous observations of the plasma decay along field lines which pass through the mid-plane at different radial distances from the magnetic field axis. Plasma flux is observed with these probes to field lines 6 cm from the axis. Microwave measurements have been made with a strongly focused, 75 GHz ($\lambda = 4$ mm) beam passing through the mid-plane, orthogonal to the mirror axis. Cut-off of the microwave beam transmission early in the confined plasma time history indicates that the radial dimension of the high density plasma region exceeds 2 cm. Measurement of the line density via interferometric measurements of the phase shift of the transmitted beam when the density has fallen below cut-off indicates an "effective" diameter of ~ 5 cm and an axial extent of ~ 20 cm. Thus, the plasma presents $\sim 100\ \mathrm{cm}^2$ target area to an incident neutral beam and occupies $\sim 400\ \mathrm{cm}^3$ volume.

The target plasma electron density versus time has been determined from the microwave phase shift measurements and has the time history shown in Fig. 2. The plasma density is evaluated from the measured line density taking into account the evolution of the "effective plasma length" from an initial value, $\langle \ell_0 \rangle$ given by the phase shift at the time the microwave signal emerges from cut-off to a final value of 5 cm ~ 100 microseconds later as determined from streak photographs of the plasma transverse growth. As shown in Fig. 2, the microwave signals emerge from cut-off at densities near $5 \times 10^{13}\ \mathrm{cm}^{-3}$ approximately 30-40 microseconds after the laser produced plasma has been created. The decay of the plasma density is a strong function of magnetic field strength and, for the highest fields shown in Fig. 2 (10.4 kG), the density remains above $10^{12}\ \mathrm{cm}^{-3}$ for ~ 500 microseconds. The data of

Fig. 2 is replotted in terms of the classical confinement parameter, $n\tau$, in Fig. 3. For the highest magnetic field case, an interval of relatively constant $n\tau$ exists which does not appear for the lower field cases in Fig. 3. The measured value of $n\tau$ in this interval of relative constant value, $\sim 6 \times 10^8$ cm^{-3} sec and the 300-400 eV hydrogen ion temperature derived from the fast atom detector in Sect. II is consistent with the calculational model of Ref. 2. After approximately 200 microseconds, the value of $n\tau$ in Fig. 3 decreases rapidly for the 10.4 kG case. This occurs concurrently with the onset of rf oscillations shown in Fig. 4 which are believed to arise from the onset of the drift cyclotron loss cone instability.

It appears from these observations that for sufficiently high magnetic field strength the confined laser produced plasma experiences a period of self-induced stabilization. During this brief period the density decay is relatively quiescent and is dominated by Coulomb scattering into the mirror loss cones. This is qualitatively the kind of behavior which would be expected on the basis of the theory of warm plasma stabilization (Ref. 1), provided the processes of production, capture, and confinement of the laser produced plasma generated significant amounts of plasma in the mirror loss cones.

For comparison with the target plasma density decay calculations, Fokker-Planck calculations have been carried out using the ISOTIONS code discussed in more detail in Sect. IV. Values of parameters of the LITE target plasma, vacuum system, and neutral beam assumed for these calculations are listed in Table I. The initial densities of H$^+$, electrons, and Li^{3+} used in the calculations were

$$n_T(0) = 2.5 \times 10^{13} \mathrm{cm}^{-3}$$

$$n_e(0) = 10^{14} \mathrm{cm}^{-3}$$

$$n_{Li}(0) = 2.5 \times 10^{13} \mathrm{cm}^{-3},$$

and the initial energies of the ions were taken to be proportional to the ion mass, an assumption consistent with observed energy ratios in free expansion of the target plasma, (Ref. 2), i.e.,

$$E_H(0) = 254 \text{ eV}$$

$$E_H(0) = 1771 \text{ eV}$$

and the initial energy of electrons was taken to be one tenth of $E_H(0)$.

TABLE I

LITE PARAMETERS

Dimensions

Plasma	Interior Vacuum Region	Outer Vacuum Region
$V = 384$ cm^3	$S_I = 1.41 \times 10^3$ cm^2	$S_V = 1.08 \times 10^5$ cm^2
$S = 410$ cm^2	$V_I = 1.41 \times 10^4$ cm^3	$V_V = 2.49 \times 10^6$ cm^3

Surface Area of Interface between Inner and Outer Vacuum Regions: $S_F = 1410$ cm^2

Neutral Beam: Current Density $I/A = 5$ mA/cm^2; $I = 200$ mA; $E_B = 10$ keV

Sticking Probabilities: Slow - $b_o = 0.3$; Intermediate - $b_{fc} = 1.0$; Fast - $b_f = 0.7$

Slow - $b_v = 0.3$ at vacuum chamber wall

Knock-Off Probabilities:

Interior Region - Slow: $C_{of} = 0.5$, $C_{ofc} = 1.0$ (produced by fast and intermediate neutrals)
Slow: $a_o = 0$ (produced by plasma ions)
Outer Region - Slow: $a_1 = 0.5$ (produced by plasma ions)

Fraction of Fast Beam Atoms Scattered in the Interior Region: $a_m = 0$

Previous calculations of the target plasma decay with the more complex two-dimensional (v,θ) HYBRID-II Fokker-Planck code had yielded results in good agreement (Ref. 2) with the electron density decay observed in LITE provided that in the calculations the electron energy was clamped at 25 eV. On the basis of these results, the constraint on the electron energy is also incorporated in the one-dimensional calculations with the modified ISOTIONS code presented here. The good agreement between the calculated and measured electron densities between 100 μsec and 250 μsec for the high field (10.4 kG) case of Fig. 2 is evident in Fig. 5. In Fig. 5, calculational results from ISOTIONS are shown for two different assumed background densities; $N_o = 10^{11}$ cm^{-3} and $N_o = 10^{13}$ cm^{-3}. Note that the electron density, n_e, remains relatively unchanged by the increase in neutral background density, while the densities of target H^+ ions also shown in Fig. 5 and labeled n_T are significantly depleted by the increase in background density. The reason for this behavior is that charge exchange between an H^+ ion and a cold background neutral results in the loss of a hydrogen atom in a mirror transit time, while a similar charge exchange interaction with a Li^{+++} ion produces Li^{++} which remains mirror confined and has a high probability of being reionized to Li^{+++} before leaving the system. Thus, as long as Li^{+++} and Li^{++} are the dominant species providing charge compensation in the plasma, the first order effect of charge exchange with cold neutrals will be to cool the electrons rather than reduce the electron density. Even at low background densities where charge exchange is negligible the hydrogen density, n_T, because of its lower temperature (Ref. 2), decays much more rapidly by Coulomb scattering out of the mirror than does the lithium density.

II. Fast Atom Energy Analyzer

A fast atom energy analyzer is used to determine the energy distribution of ions in the confined plasma. The detector consists of a gas ionizing cell and a parallel plate electrostatic analyzer with an entrance angle of 43°. Neutral atoms born in the confined plasma by recombination or by charge-exchange with cold background gas are reionized in the gas cell and detected in four energy channels in the analyzer. The detectors are 260° channel electron multipliers with 10 mm aperture cones and capped collectors (CEM 355367). The back plate of the analyzer opposite the entrance is open through a 1" pipe in order to prevent photons from the plasma from reflecting into the detectors. The analyzer and gas cell are installed in a separate vacuum system. The fast atom detector views the plasma through a $\sim 1\ cm^2$ cross section collimating tube along a line in the mid-plane nearly orthogonal to the neutral beam path. This detector line is slightly displaced ($\sim$ 1 cm) from the center of the plasma in order to avoid saturation of the detectors by energetic photons produced during laser irradiation of the LiH particle. The gas ionizing cell is 10 cm long and is normally operated with N_2 at a pressure of $2\text{-}4 \times 10^{-3}$ torr. Figure 6 is a diagram of the analyzer system. The energy for the four different channels if .6 qV, .9 qV, 1.2 qV and 1.5 qV where V is the voltage on the analyzer plates. The plates have been operated with up to 12 kV on the plate to detect ions with energies as high as 18 keV.

The time dependence of the neutral flux from the confined target plasma has been measured over the range from 300 eV to 12 keV. Figure 7a shows the analyzer outputs at 300, 600, and 750 eV and in Fig. 7b are shown the outputs at 1.8, 3.6, and 4.5 keV for another plasma decay. The gains are the same for both shots. In general, the lower energy channels observe a large initial flux which decays in about 100 μsec to a lower level that continues for several hundred μsec. At higher energies, the plasma flux increases in time, reaching a peak at about 75 μsec and then gradually dacays over several hundred microseconds.

From measurements of the freely expanding (no magnetic field) laser produced plasma it is known that the velocity distributions for all four species in the plasma (H^+, Li^{+++}, Li^{++}, Li^+) are similar (Ref. 2), so that the mean kinetic energy in the expanding plasma is primarily in the Li ions (7 times greater than the mean energy of the H ions). We assume that the Li and H ions do not equilibrate with each other during capture and confinement, and the flux below 1 keV is therefore predominately H^0. Under this assumption, we can determine the energy distribution of the H^+ component of the plasma. Figure 8 from Ref. 2 is the resulting relative density of H^+ ions at different energies calculated from the neutral flux. The plot is obtained by correcting the output of the detectors for the probability of reionization of the H^0 in the gas cell as a function of energy (Ref. 4). The results of Fig. 8 give a temperature of about 300 eV for the confined H^+ ions. The charge exchange and ionization cross sections for Li^+ are not as well known as for H^+, but the detector outputs at higher energies indicate a temperature of about 2 to 4 keV for the Li^+ ions in the plasma. The plasma also contains Li^{+++} and Li^{++} ions; however, since these ions cannot reach the analyzer through a one step process such as charge exchange or recombination, their temperature or density cannot be inferred from the fast atom detector measurements.

The geometry of the neutral injection experiments and the location of the fast atom energy analyzer are shown in Fig. 9 as viewed along the mirror axis from the top of the experiment chamber. The beam impinges on the mid-plane of the target plasma, (Fig. 1 and Fig. 9), normal to the mirror axis, and is limited in cross section by an 83 mm diameter aperture at the input of the vacuum chamber. The magnetic field in this region is azimuthally symmetric with respect to the mirror axis; the field lines are vertical and the field direction is downward. As discussed in Sect. I, the radial extent of the target plasma in this region is $\sim$2.5-3 cm. Energetic hydrogen ions are introduced into the target plasma when the beam neutrals experience charge exchange or ionizing collisions in the target plasma. The resulting hot ions gyrate around the field lines with Larmor radii which are significant compared to the plasma dimensions (for $B = 10$ kG and $E = 10$ keV, $\rho_i = 1.5$ cm). Some of these hot ions are reconverted to fast neutrals by charge exchange collisions with cold neutrals from the background gas in the chamber. Those fast neutrals which are created in a 1 cm^2 area with velocities along the detector line will enter the detector.

The fast atom energy analyzer has been calibrated by injecting the neutral beam into the magnetic field without the target plasma present. By raising the ambient pressure in the vacuum chamber to provide a gas target, an equilibrium, low density plasma is created, and the resulting fast neutral flux observed with the fast atom energy analyzer. The hot ion density n_H in the magnetic field builds up as:

$$\frac{dn_H}{dt} = \frac{I n_o \sigma_i \ell}{q V_p} - n_H n_o \langle \sigma_{cx} v \rangle \tag{1}$$

where I = beam current
n_o = cold gas density
σ_i = ionization cross section
ℓ = "effective" plasma length
V_p = plasma volume
n_H = hot ion density
σ_{cx} = charge exchange cross section
v = hot ion velocity

At equilibrium the fast neutral production rate is given by

$$\frac{n_H}{\tau_{cx}} = \frac{I n_o \ell \sigma_i}{q V_p} \tag{2}$$

where τ_{cx} is the charge exchange lifetime. The fast atom energy analyzer signal is then given by

$$S = K \cdot V_d \cdot \frac{n_H}{\tau_{cx}} \tag{3}$$

where V_d, the detection volume, is the plasma volume sampled by the detector.

For injection of a 3 mA/cm^2, 10 keV beam into a 5×10^{-5} Torr N_2 gas target, the signal amplitudes on four channels set for 5, 7, 10 and 12 keV respectively are shown in Fig. 10. Signals are observed at both the beam energy of 10 keV and half energy of 5 keV because both H^+ and $H_2{}^+$ ions are extracted from the source. Negligible signals are detected on the 7 and 12 keV channels. Assigning a relative value of 1 to the signal amplitude on the 10 keV channel, the proportionality constant, K, can be evaluated. With a nitrogen background density of $n_o = 6.3 \times 10^{12}$ cm^{-3} and nitrogen ionization cross section $\sigma_i = 3 \times 10^{-16}$ cm^{-2} and assuming $I\ell/V_p \approx I/A$, Eq. 2 gives $n_H/\tau_{cx} \approx 3.5 \times 10^{13}$ ions/cc-sec. The detection volume is determined by the 8 cm beam diameter and 1 cm^2 aperture giving $V_d \approx 1$ cm^2 x 8 cm = 8 cm^3. Thus, the value of the calibration constant K in Eq. 3 is $K = 3.5 \times 10^{-15}$.

III. Experimental Observations of Hot Ion Density

With no neutral beam injected, the signals appearing on the fast atom detector energy channels at 6, 9, 12, and 15 keV due to the energetic components of the laser produced plasma are as shown in Fig. 11a. With a 5 mA/cm^2, 12 keV neutral beam incident on the plasma over the 40 cm^2 aperture area shown in Fig. 1, the signals obtained on the same fast atom detector energy channels are presented in Fig. 11b. Note that the signal has been significantly enhanced at both the beam energy (12 keV) and half energy (6 keV). The fast neutral signal on the 12 keV channel determined from this data is plotted in Fig. 12a and for comparison the electron density decay of the target plasma measured with the microwave interferometer is shown in Fig. 12b. The peak fast neutral flux signal occurs approximately 50 μsec into the decay and is four times as large as the signal observed in the gas target calibration discussed in Sect. III. Assuming that the observation length is now governed by the target plasma width rather than the beam diameter, the detection volume is ~ 5 cm^3. From Eq. 3 the peak signal of Fig. 12a corresponds to a fast neutral production rate of $n_H/\tau_{cx} = 2.2 \times 10^{14}$ ions/cm^3-sec. The fast neutral flux is replotted to this scale in Fig. 13a. To convert this curve to one of hot ion density requires a knowledge of the charge exchange time, τ_{cx}. The ambient background pressure during these experiments was measured as 3×10^{-6} Torr (3.8×10^{11}/cm^3 at 77°K) which gives a $\tau_{cx} \approx 20$ μsec, and the corresponding hot ion density plot, given in Fig. 13b, reaches a peak value of 4.4×10^9 ions/cm^3.

IV. Analysis of Hot Ion Buildup in LITE Target Plasma

The hot ion buildup is observed over the initial ~ 200 μsec of the target plasma decay during which, as discussed in Sect. I, the decay is quiescent and can be described by a classical Fokker-Planck model. As a result, for comparison with the measurements, the ISOTIONS code used for the target plasma decay calculations of Sect. I has been further modified to include the effects of charge exchange and ionization interactions with an injected neutral beam and used to calculate the buildup of 10 keV H$^+$ ions by injection of a 200 mA neutral beam into the LITE target plasma. The ISOTIONS code, described in Ref. 5 is a one-dimensional, multispecies Fokker-Planck code developed at Lawrence Livermore Laboratory for the analysis of mirror confined plasmas. Modifications incorporated into the code for the LITE target plasma decay and hot ion buildup calculations consisted of (a) the substitution of the iteration scheme of Chang and Cooper (Ref. 6) for the existing algorithms, (b) the addition of a subroutine for modeling the neutral background and effects of wall reflux of fast neutrals escaping from the plasma after charge exchange, (c) new source terms and subroutines for calculating energy-dependent cross sections and plasma-averaged and source-averaged rate coefficients.

In these calculations, four particle species were considered, namely, the target plasma ions H$^+$, and Li^{3+}, the injected ions H$^+$, and the electrons. A Fokker-Planck equation for the particle distribution function is solved for each species (Ref. 5):

$$\frac{\partial F_j}{\partial \tau} = \frac{1}{x^2}\frac{\partial}{\partial x}\left[A_j(x)F_j(x) + B_j(x)\frac{\partial F_j}{\partial x}\right] - C_j(x)F_j(x) + D_j(x) \qquad (4)$$

The independent variables are scaled velocity, $x = v/v_o$ and the scaled time $\tau = t/t_N$. The parameter v_o is a conveniently chosen velocity and t_N is a characteristic time for electrons, namely, $2v_o{}^3 me^2/4\pi K_e e^4$, in which K_e is the normalization factor for the electron distribution function defined by

$$n_e(t) = K_e \int_0^\infty F_e(x,t)\, x^2 dx$$

The dynamical friction $A_j(x)/x^2$ and the diffusion coefficient $B_j(x)/x^2$ are defined in Ref. 5. These terms are particle-conserving and account for energy exchange among the various plasma species. The coefficient $C_j(x)$ accounts for particle losses by classical scattering into the mirror loss cones in the electron and ion equations. In the two equations for H^+ ions (target ions and injected ions), $C_j(x)$ also includes background neutrals. Moreover, the target H^+ ion equation $C_j(x)$ contains a term representing losses by charge exchange with the 10 keV neutral beam. The source term $D_j(x)$ in the electon equation represents the rate of increase of $F_e(x)$ by ionization of the neutral beam. In the equation for the injected H^+ ions, $D_j(x)$ contains the source contributions of both ionization and charge exchange with target H^+ ions.

The charge exchange loss contribution to $C_j(x)$ is calculated as

$$H l j(x) = v\sigma_{cx}(v)\,(n_f + n_{fc}) + v\,\sigma_{H2}(v)\,n_0 \tag{5}$$

in which σ_{cx} is the cross section for the (H, H^+) charge transfer reaction and σ_{H_2} is the corresponding cross section for (H_2, H^+) charge transfer. Their values are calculated from analytical fits to curves shown in Fig. 14. The densities n_f, n_{fc} and n_o are values of the energetic (~ 10 keV) H ions, Franck-Condon (~ 10 eV) H atoms and thermal H_2 molecules, respectively, which account for shielding of neutrals from the plasma interior and yield the correct reaction rates. These neutral densities are calculated in the subroutine VAKBAK discussed in Ref. 7. For target H^+ ions, the contribution to $C_j(x)$ of charge exchange with the neutral beam is approximated by

$$L_{cx}(v) = \frac{I}{A}\,\frac{<\sigma_{cx}V>_s}{<V>_s} \tag{6}$$

in which I/A is the current density of the neutral beam at the target plasma and $<\sigma_{cx}V>_s$ and $<V>_s$ are beam-distribution-averaged values of the rate coefficient and particle speed.

The source contributions to $D_j(x)$ for electrons and injected ions are respectively

$$S_e(v) = \frac{I}{A}\,\frac{n_T<\sigma_{ii}V>_s + n_e<\sigma_{ie}V>_e}{<V>_s} \tag{7}$$

in which $<\sigma_{ie}V>_e$ is an average over the plasma electron distribution functions, and

$$S_H(v) = S_e(v) + \frac{I}{A}\,n_T\,\frac{<\sigma_{cx}V>_s}{<V>_s} \tag{8}$$

The densities n_T and n_e are the target plasma H^+ ion and electron densities and the ionization rate coefficients $<\sigma_{ii}V>_s$ and $<\sigma_{ie}V>_e$ were obtained by averages over analytical fits to the curves shown in Fig. 15.

Upon injection of a 200 mA beam of 10 keV H atoms at a current density of $I/A = 5$ mA/cm^2 into the target plasma, a portion of the beam is trapped as 10 keV H^+ ions. The rate constants for trapping are $<\sigma_{cx}V> = 1.36 \times 10^{-7}$ cm^3-sec^{-1} for charge exchange on target H^+ ions, $<\sigma_{ii}V> = .95 \times 10^{-8}$ cm^3-sec^{-1} and $<\sigma_{ie}V> = 1.26 \times 10^{-8}$ cm^3-sec^{-1} for ionization by H^+ ions and electron collisions, respectively. Although the charge exchange process has the highest rate constant, from the results of Fig. 5 the density of target H^+ ions is so much lower than the electron density that the hot ions are trapped mainly by electron ionization collisions with the beam neutrals. Since the plasma mean chord length $4\ V/S \approx 3.8$ cm and thus the effective plasma radius is about twice the gyroradius of the 10 keV photons in a field of B = 10 kilogauss, the loss rate of hot ions by charge exchange with the neutral background is calculated with the ambient value N_o of cold neutrals substituted for n_o in Eq. 5. For initial values of ambient densities of cold neutrals of $N_o(0) = 10^{11}$, 4×10^{11} and 10^{12}cm^{-3}. The calculated time-dependences of the total hot ion populations are presented in Fig. 16. It is clear from these curves that the lifetimes of the hot ions are charge exchange dominated at these values of background density.

The energies of the trapped ions are shifted downward by collisions with the target plasma species, most of the energy being transferred to the electrons, which constitute an energy sink by virtue of their clamped energies. In Table II, the energies and densities of the hot ions, and electron densities are tabulated for 110, 160, and 210 μsec for the $N_o(0) = 10^{11}$, 4×10^{11} and 10^{12} cm^{-3} cases. From summary tables of the ISOTIONS calculations it was possible to calculate values of charge exchange times

$$\tau_{cx} = \left(n_H / \frac{dn}{dt}\right)_{cx}$$

and the electron drag time

$$\tau_d = \left(n_H E_H / \frac{d(n_H E_H)}{dt}\right)_e$$

where $d(n_H E_H)/dt)_e$ is the rate of energy transfer to electrons and the source term S_H; these quantities are also given in Table II. Values of $n_e \tau_d$ thus obtained are in good agreement with the Spitzer approximation

$$n_e \tau_d \doteq 7.1 \times 10^{11}\ T_e(\text{keV})^{3/2}$$

for 25 eV electrons. The parameter τ_d is a measure of the rate of removal of 10 keV ions to lower energies and is comparable with the ratio n_H/S_H. This implies that the hot ions are removed to lower energies almost as fast as they are trapped in the plasma.

TABLE II

SUMMARY TABLE FOR HOT IONS, DENSITIES AND TIME CONSTANTS

t(sec)	n_H(cm^{-3})	E_H(keV)	n_e(cm^{-3})	τ_d(sec)	τ_{cx}(sec)	S_H ($cm^{-3}sec^{-1}$)
$N_o(0) = 10^{11}$ cm^{-3}						
$110\text{x}10^{-6}$	$3.08\text{x}10^{9}$	6.717	$7.92\text{x}10^{12}$	$2.69\text{x}10^{-4}$	$8.28\text{x}10^{-5}$	$2.40\text{x}10^{13}$
160	2.39	6.635	5.36	3.95	8.30	1.61
210	1.82	6.680	4.01	4.93	8.31	1.20
$N_o(0) = 4 \times 10^{11}$ cm^{-3}						
110	$6.03\text{x}10^{8}$	8.50	$7.91\text{x}10^{12}$	$3.04\text{x}10^{-4}$	$1.93\text{x}10^{-5}$	$2.39\text{x}10^{13}$
160	3.51	9.09	5.35	4.35	1.83	1.60
210	2.39	9.29	3.99	5.71	1.78	1.19
$N_o(0) = 10^{12}$ cm^{-3}						
110	$1.88\text{x}10^{8}$	9.48	$7.90\text{x}10^{12}$	$2.90\text{x}10^{-4}$	$7.35\text{x}10^{-6}$	$2.36\text{x}10^{13}$
160	1.19	9.59	5.31	4.40	7.18	1.58
210	8.57	9.64	3.96	5.78	7.05	1.17

The calculated time-dependent densities for the hot ions added to the plasma are plotted in Fig. 16 for the three cases studied along with the experimentally derived 12 keV ion density curve of Fig. 13. (The difference between the 10 keV beam energy of the calculations and the 12 keV beam energy of the experiments is not significant for this comparison.) General agreement is observed between the shape of the experimental and calculated total injected ion density decay curves for a background density of $N_o = 4 \times 10^{11} cm^{-3}$, a value corresponding to the initial background pressure of 3×10^{-6} Torr. The magnitude of the experimentally indicated maximum hot ion density near the beam energy is considerably larger than the calculated value. The energy resolution of the energy analyzer is ~15% so that under those conditions (Table II) when the electron drag time, τ_d, is comparable to or less than the charge exchange time, τ_{cx}, significant cooling of the hot ions will occur and further reduce the signal expected in the 12 keV energy channel. Several factors may contribute to the difference between the calculated and observed signal amplitude. First, the experimentally determined values of hot ion density are over-estimated because of the contribution of the hot component of the target plasma (seen in Fig. 11a) to the fast atom energy analyzer signal at the beam energy. Second, the target plasma lithium ions may contribute substantially to the trapping of hot ions by ionizing collisions and perhaps by charge exchange with the neutral beam. Third, a transient neutral background considerably higher than the initial value would lower the value of the hot ion density calculated from the fast atom energy analyzer signals and also decrease the effect of electron drag by decreasing the charge exchange lifetime of the ions.

Experimental measurements of hot ion buildup upon injection of a 5 mA/cm^2 (200 mA) 12 keV neutral hydrogen beam into a laser produced LiH plasma in LITE show an energetic ion buildup to a peak value of 4.4×10^9 ions/cm^3 decreasing thereafter as the target plasma decays. The absence of density dumps and the lack of rf bursts during the initial ~ 200 microsecond interval when the fast atom signals at the beam injection energy are observable indicates a classical behavior of the target plasma with beam injection during this period, just as observed experimentally for the decaying target plasma alone over the first ~ 200 microseconds (Ref. 2). Consistent with this result, a classical Fokker-Planck model used to describe the neutral injection into the LITE target plasma gives results in qualitative agreement with the observed injection buildup provided the electron energy is clamped. Further experiments involving higher current neutral injection (~15 A) and warm, streaming plasma stabilization of the confined target plasma are planned to extend these results to longer times and the hot ion buildup to higher densities.

References

1. Baldwin, D. E., H. L. Berk and L. D. Pearlstein, Phys. Rev. Lett. 36, 1051, 1976.

2. Ard, W. B., J. H. Stufflebeam, and R. G. Tomlinson, Magnetic Confinement of Laser Produced LiH Plasma in LITE, UTRC 76-98, June, 1976.

3. Haught, A. F., D. H. Polk, W. J. Fader, R. G. Tomlinson, R. A. Jong, W. B. Ard, A. E. Mensing, T. L. Churchill, J. H. Stufflebeam, F. J. Bresnock: High Beta Capture and Mirror Confinement of Laser Produced Plasmas, UTRC R76-953200-24, COO-2277-7, Semiannual Report, Jan., 1976, prepared under Contract E(11-1)-2277 for the U.S.E.R.D.A., pg. 31.

4. Barnett, C. F., and J. A. Ray, Nuclear Fusion 12, 65, 1972.

5. Mirin, A. A., ISOTIONS, a One-dimensional Multispecies Fokker-Planck Computer Code, UCRL-51616, 1974.

6. Chang, J. S., G. Cooper, J. Comp. Phys. 6, 1, 1970.

7. Haught, A. F., D. H. Polk, J. T. Woo, W. J. Fader, R. G. Tomlinson, R. A. Jong, W. B. Ard, A. E. Mensing: High Beta Capture and Mirror Confinement of Laser Produced Plasmas, Semiannual Report, Jan., 1975, UARL R953100-22, COO-2277-5, prepared under contract AT(11-1)-2277 for the U.S.E.R.D.A., pg. 24.

List of Figures

TARGET PLASMA GEOMETRY

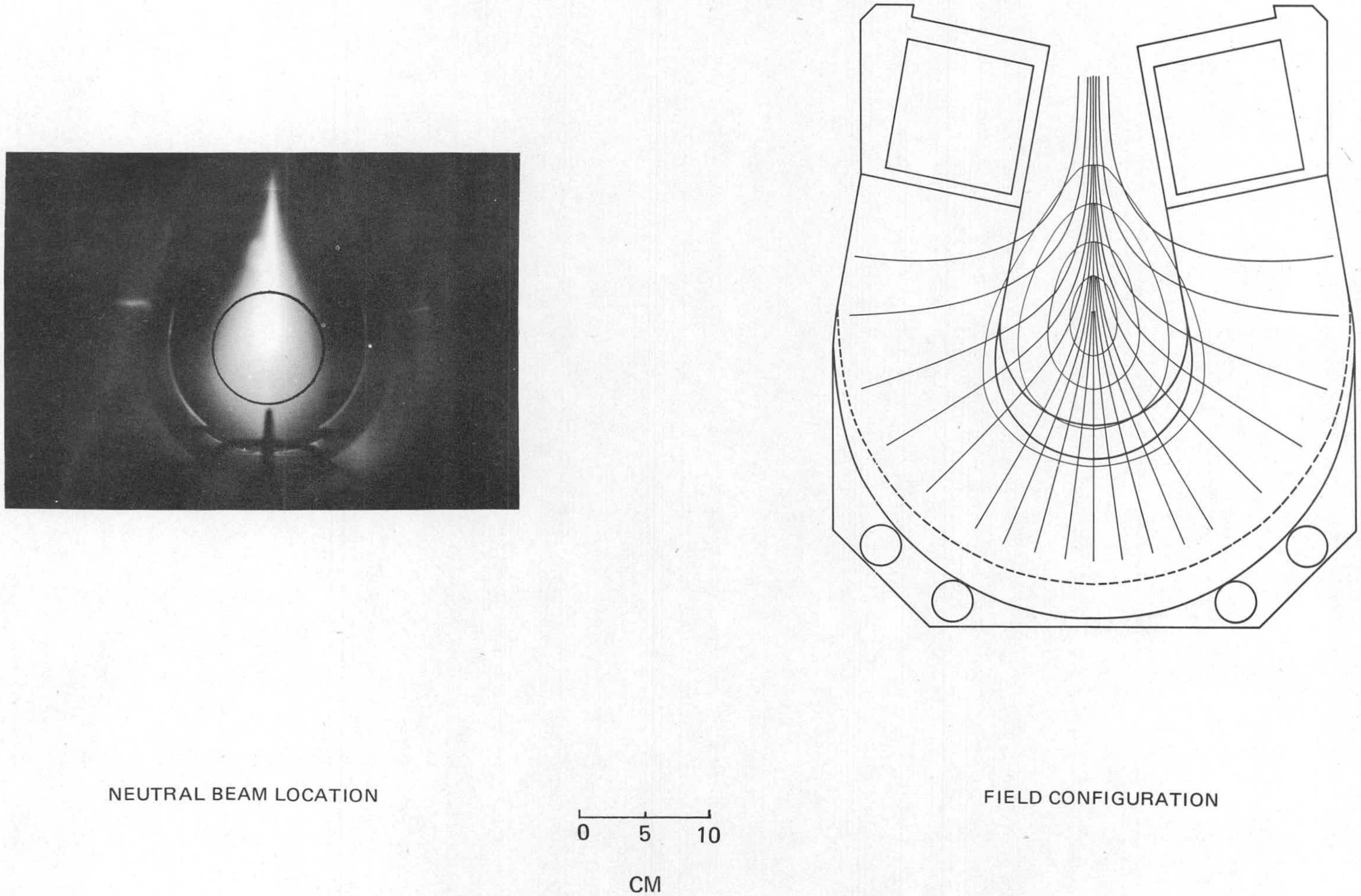

NEUTRAL BEAM LOCATION

FIELD CONFIGURATION

FIG. 1

FIG. 2

TARGET PLASMA ELECTRON DENSITY VS TIME

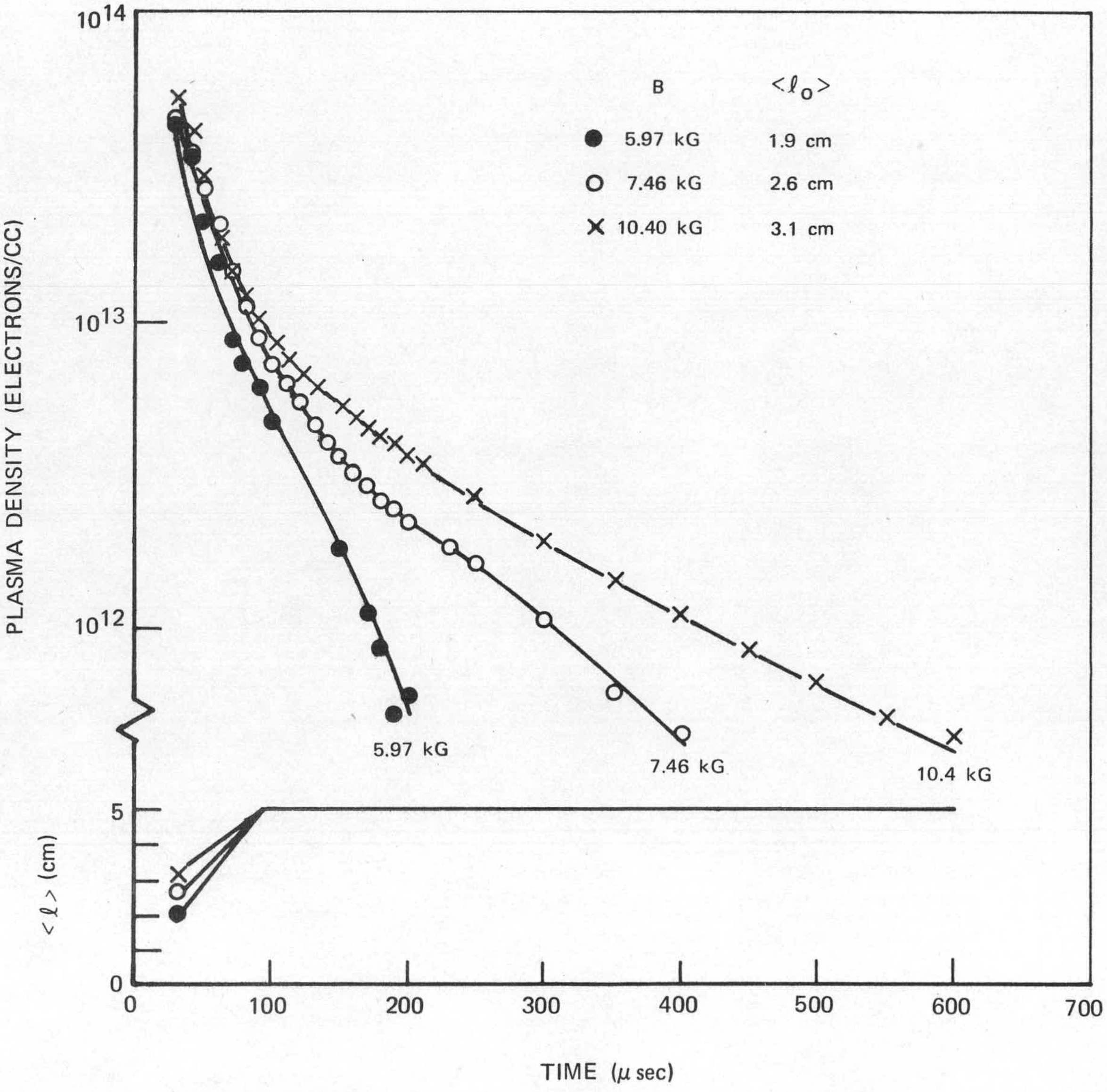

R08–75–1

FIG. 3

TARGET PLASMA CONFINEMENT PARAMETER VS TIME

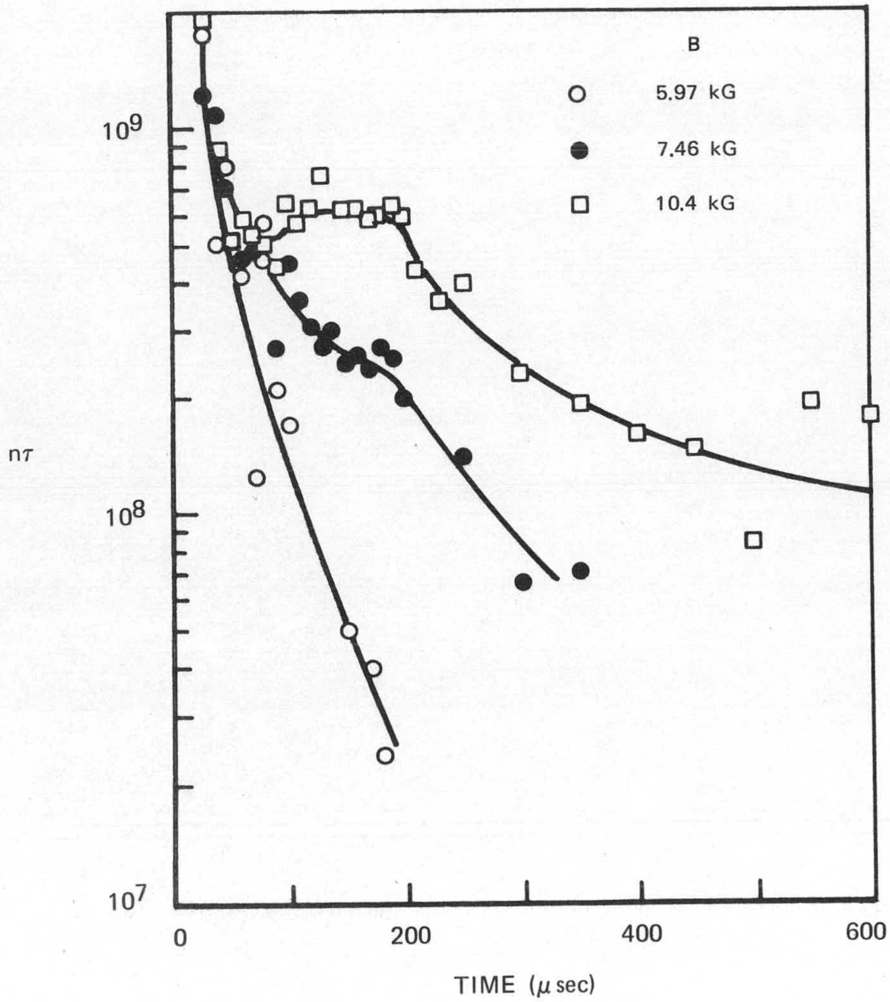

FIG. 4

UNSTABILIZED TARGET PLASMA RF OSCILLATIONS

B = 10.4 kG

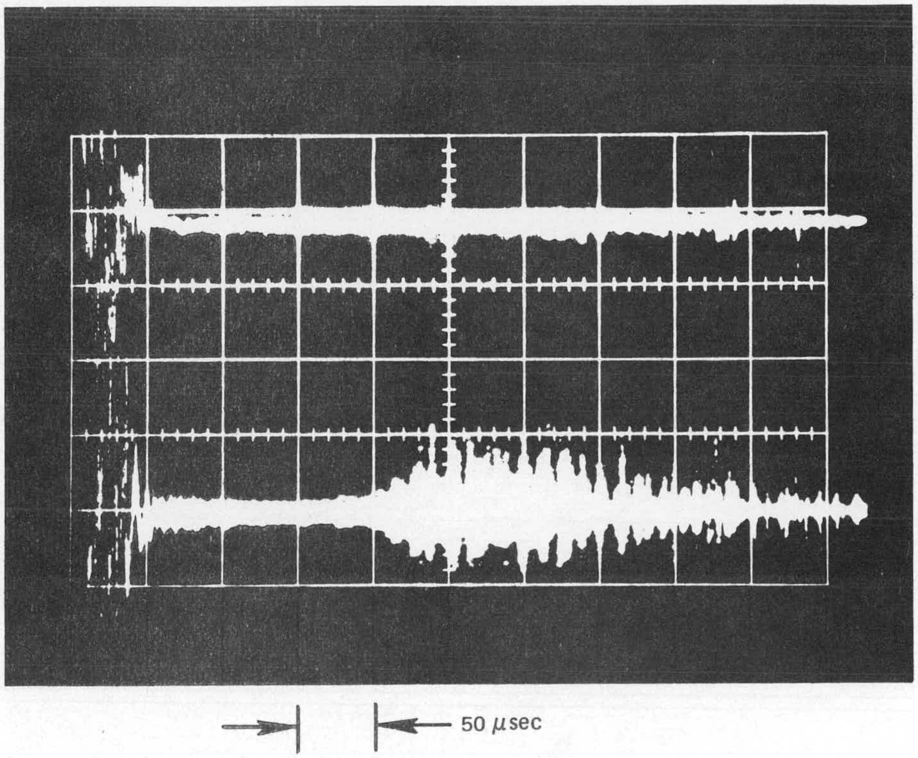

FIG. 5

EXPERIMENTAL ELECTRON DENSITY AND CALCULATED ELECTRON AND HYDROGEN DENSITIES

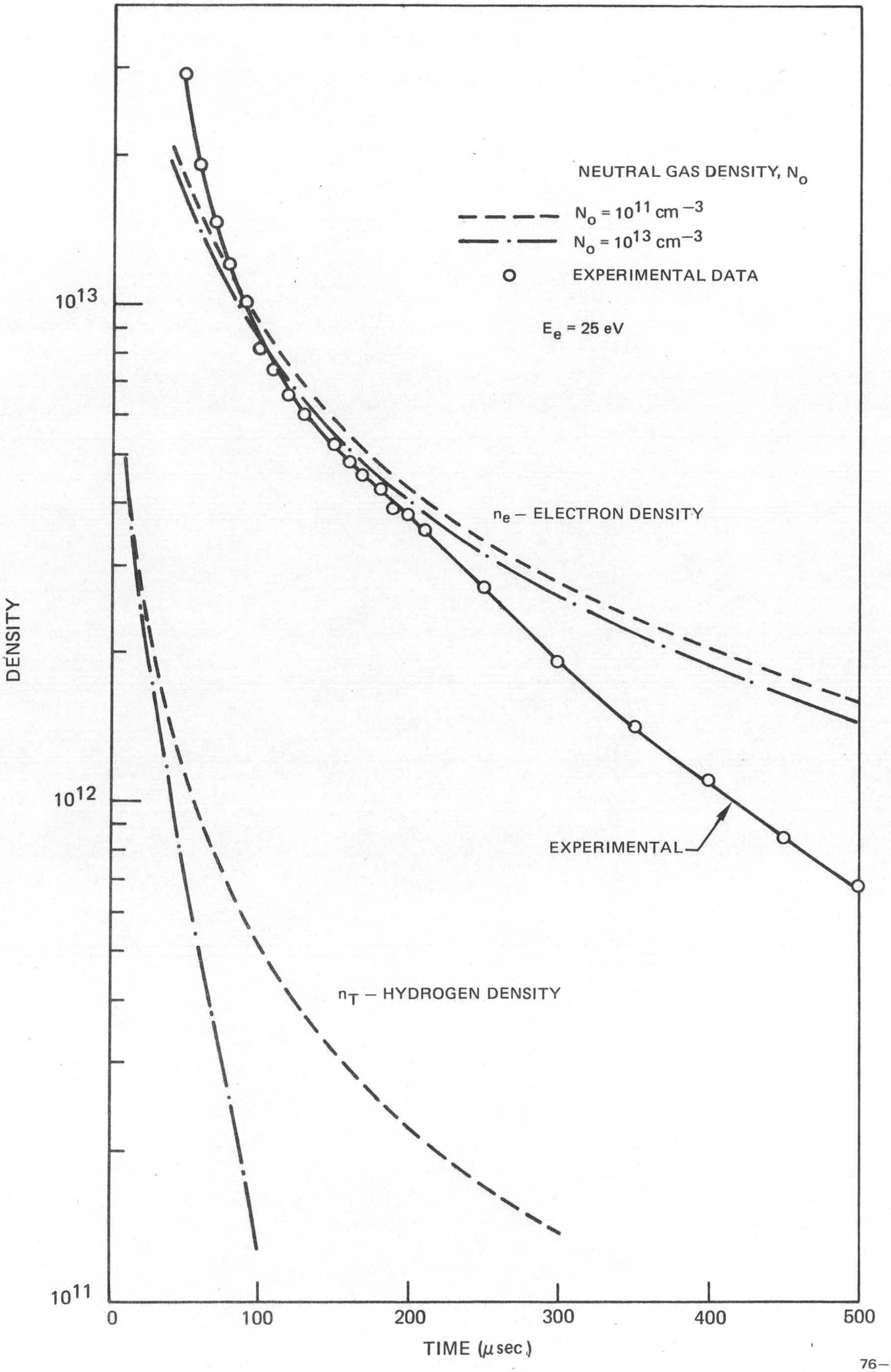

76–06–198–5

SCHEMATIC OF FAST ATOM ENERGY ANALYSER

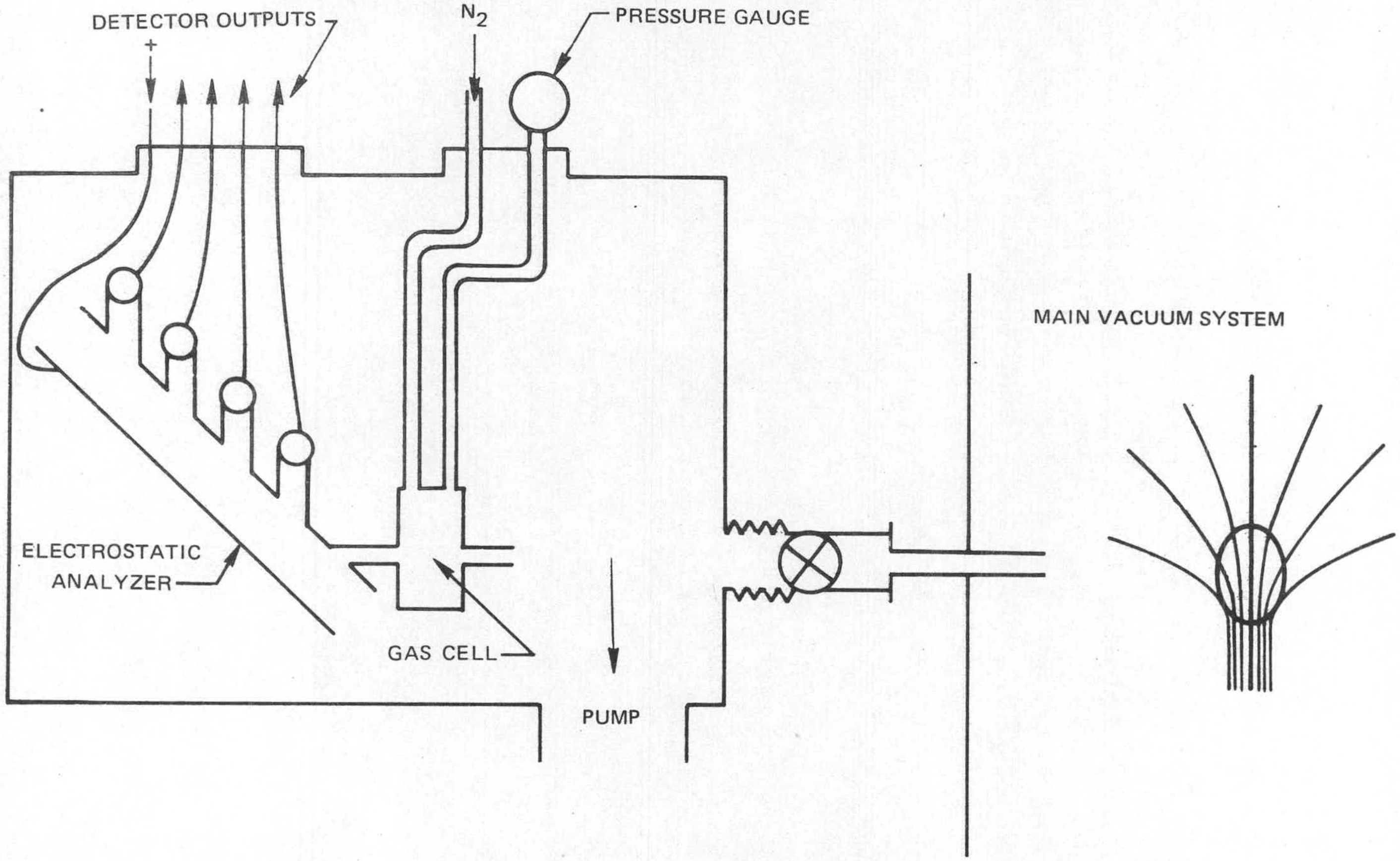

FIG.6

R1–179–2

FAST ATOM ENERGY ANALYZER SIGNALS FOR LiH TARGET PLASMA

FIG. 7a

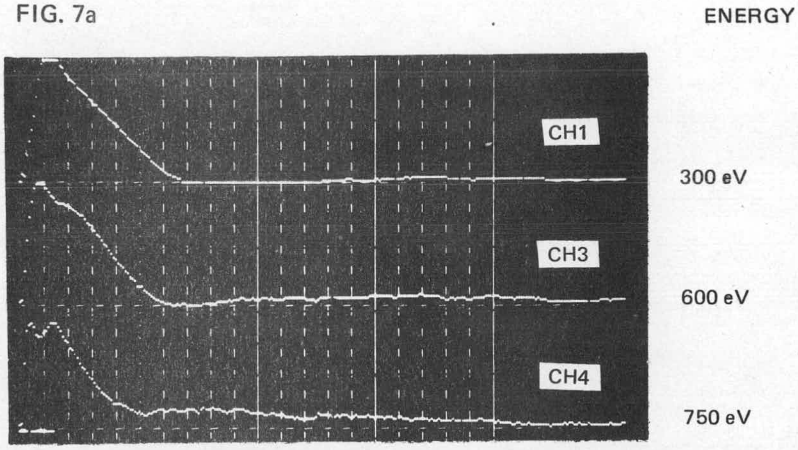

FIG. 7b

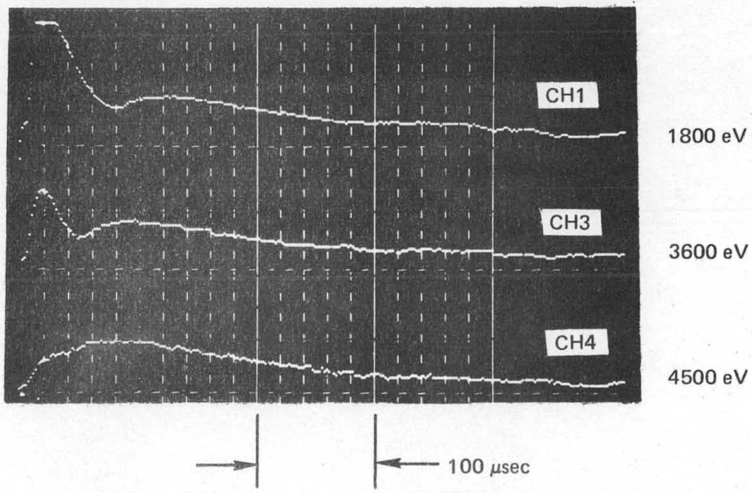

ENERGY DISTRIBUTION OF HYDROGEN IONS IN PLASMA

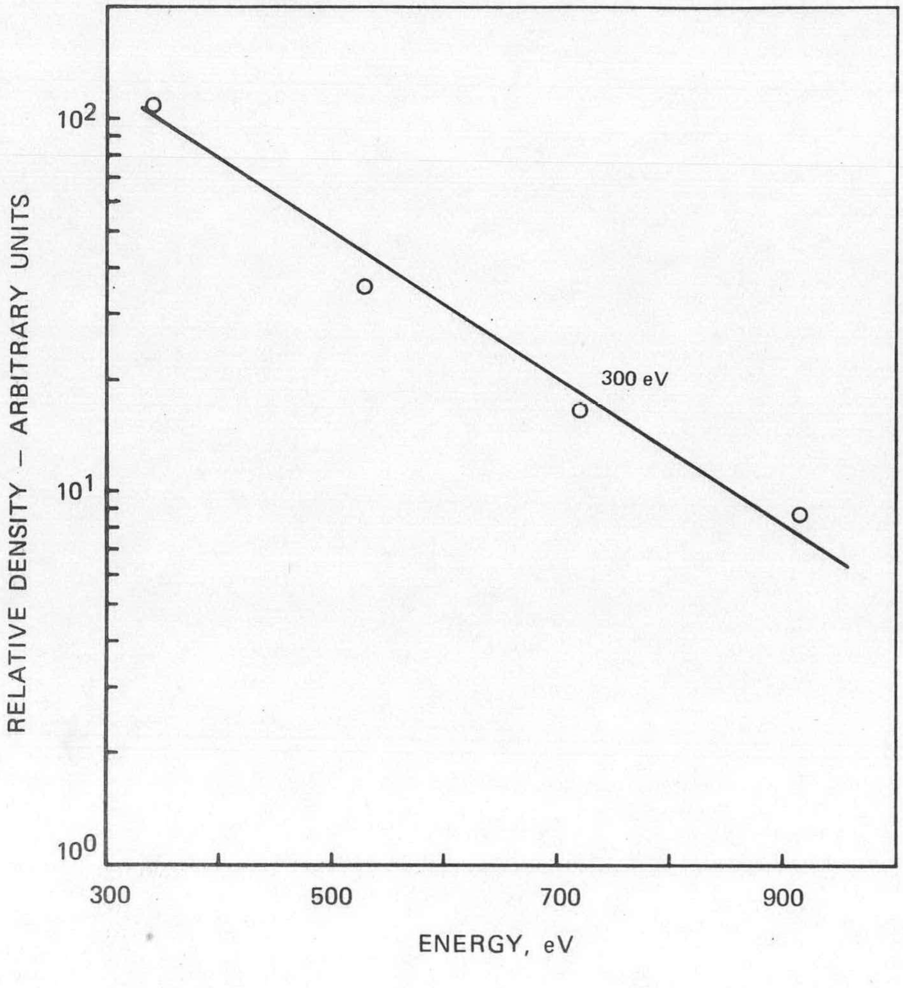

DETECTION OF FAST ATOM FLUX DUE TO NEUTRAL INJECTION

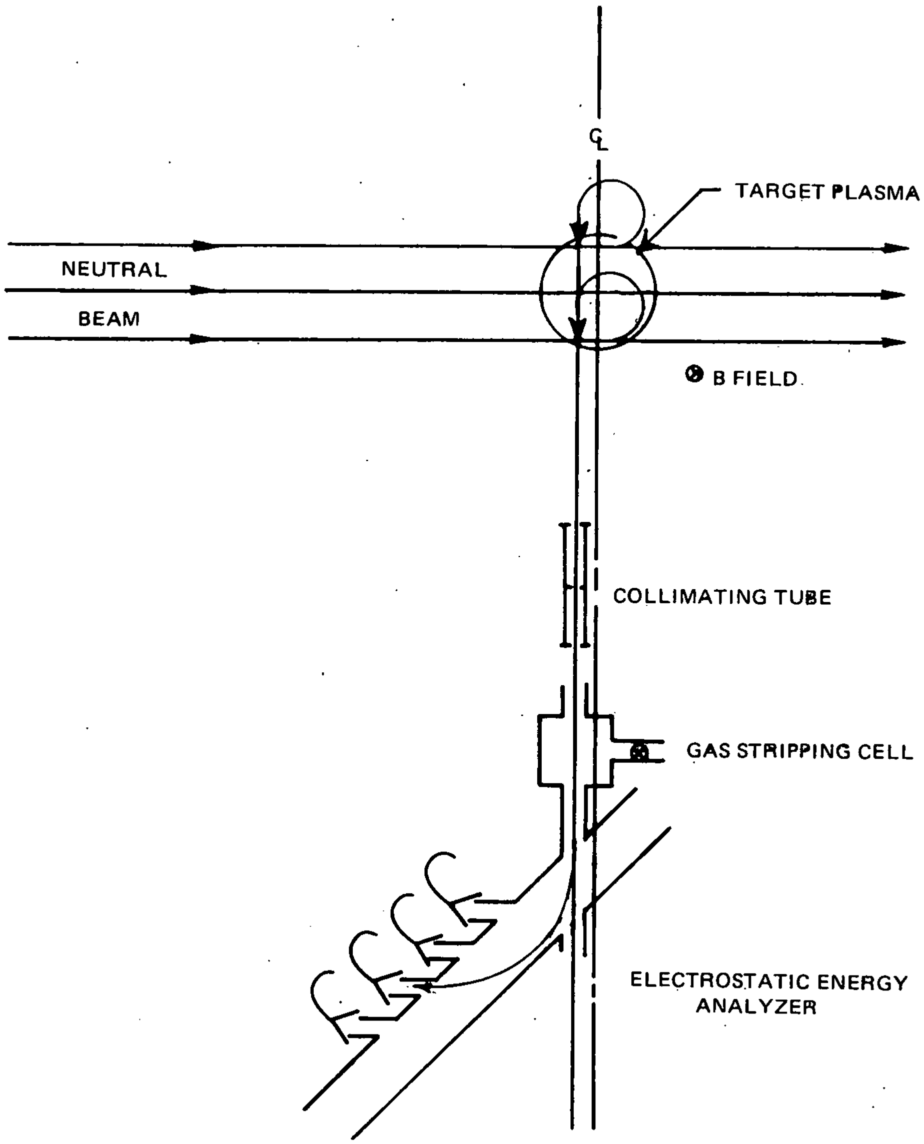

FIG. 10

FOUR CHANNEL FAST ATOM ENERGY ANALYZER SIGNALS FROM NEUTRAL BEAM INJECTION INTO GAS TARGET

(5×10^{-5} Torr N_2)

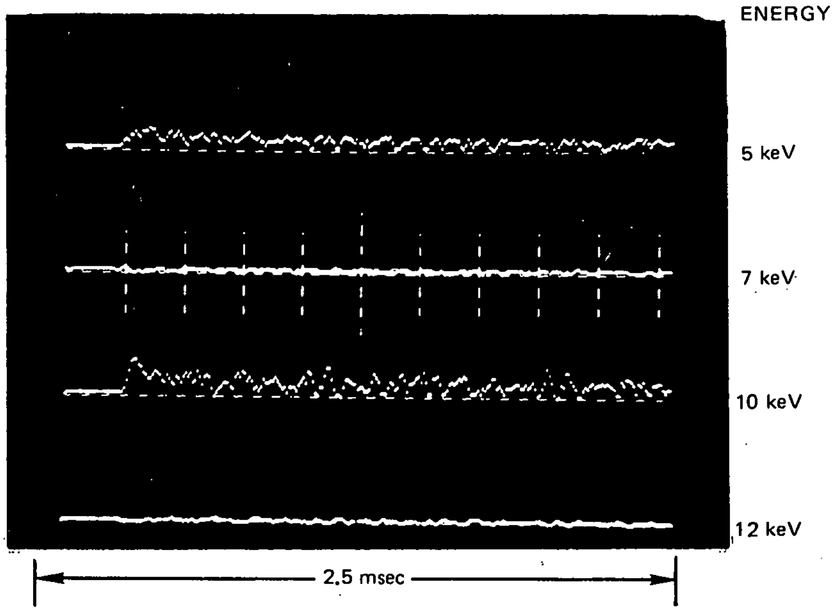

FOUR CHANNEL FAST ATOM ENERGY ANALYZER SIGNALS

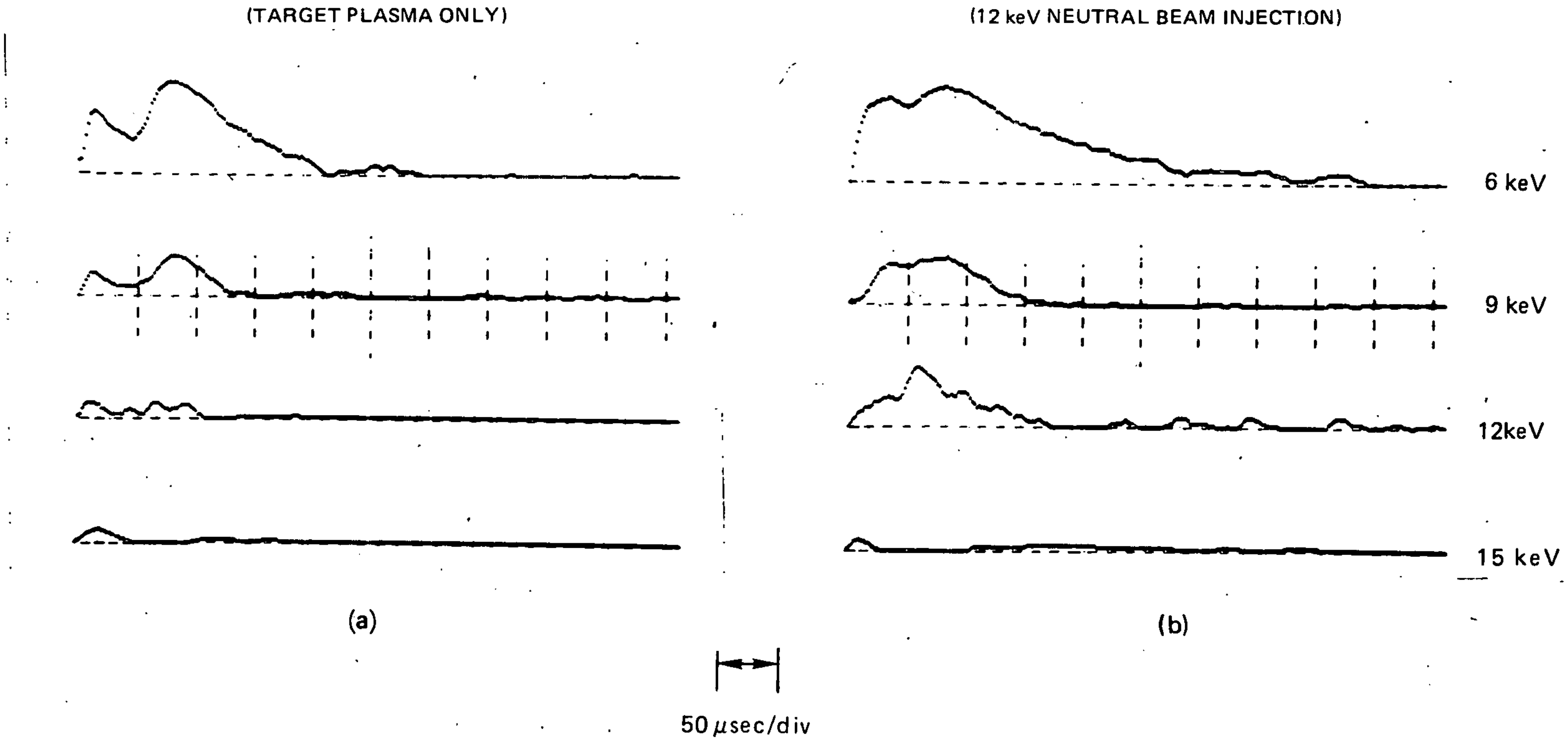

76–02–234–7

FIG. 11

FIG. 12

NEUTRAL INJECTION ON LITE

BEAM INTENSITY = $5 mA/cm^2$

SHOT #1285

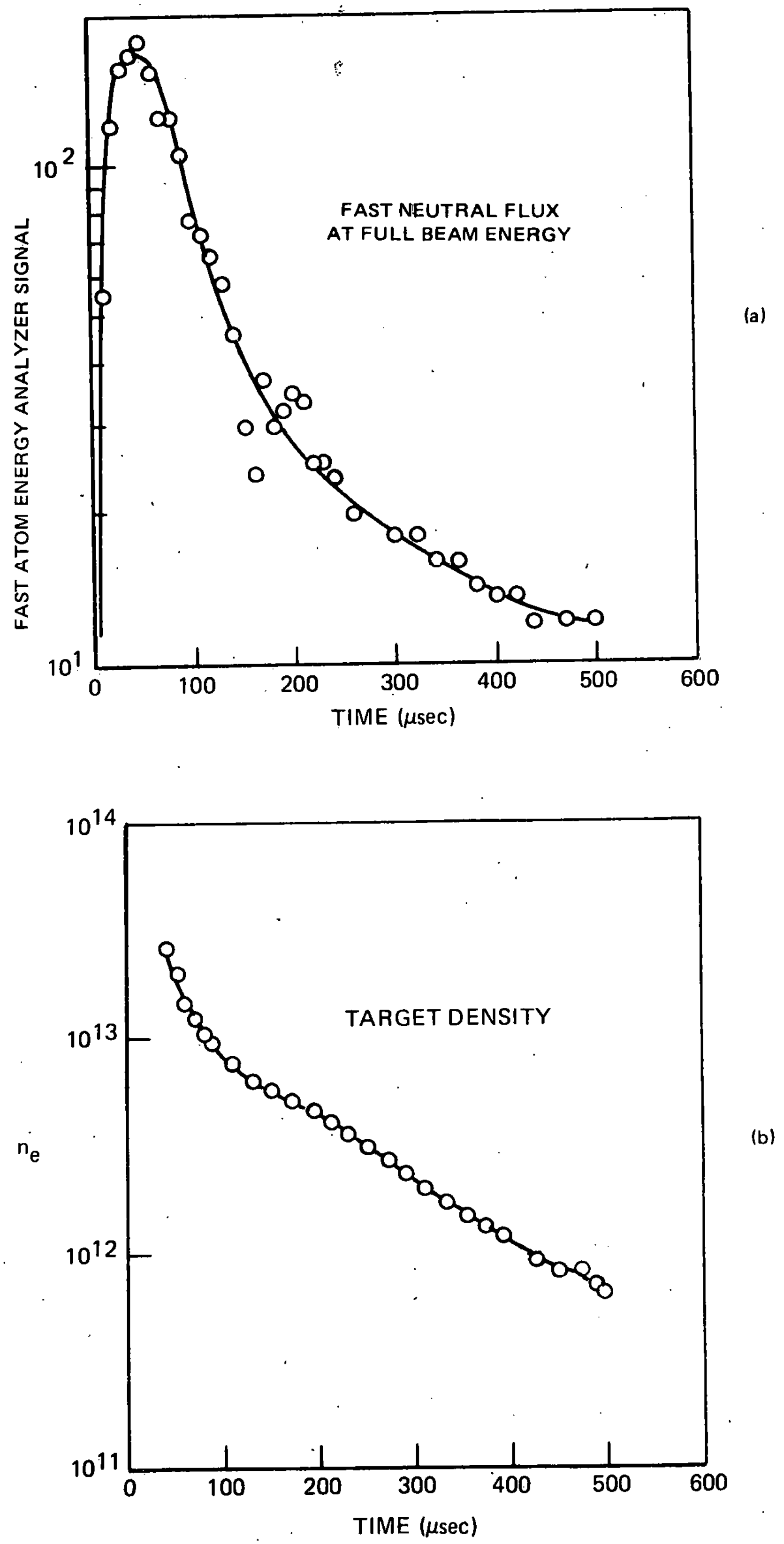

FIG. 13

NEUTRAL INJECTION DATA

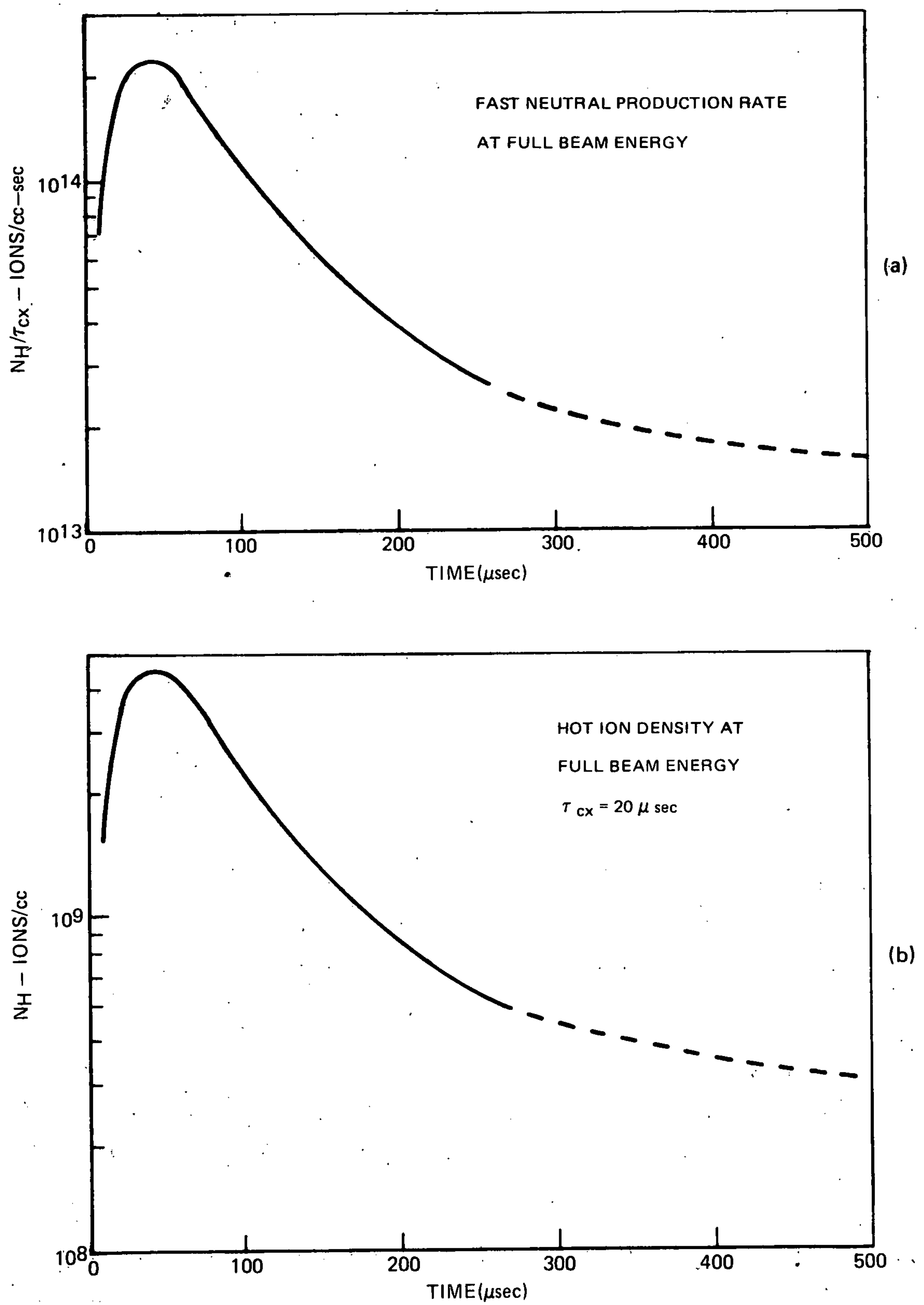

76–06–162–1

FIG. 14

CHARGE EXCHANGE CROSS SECTIONS

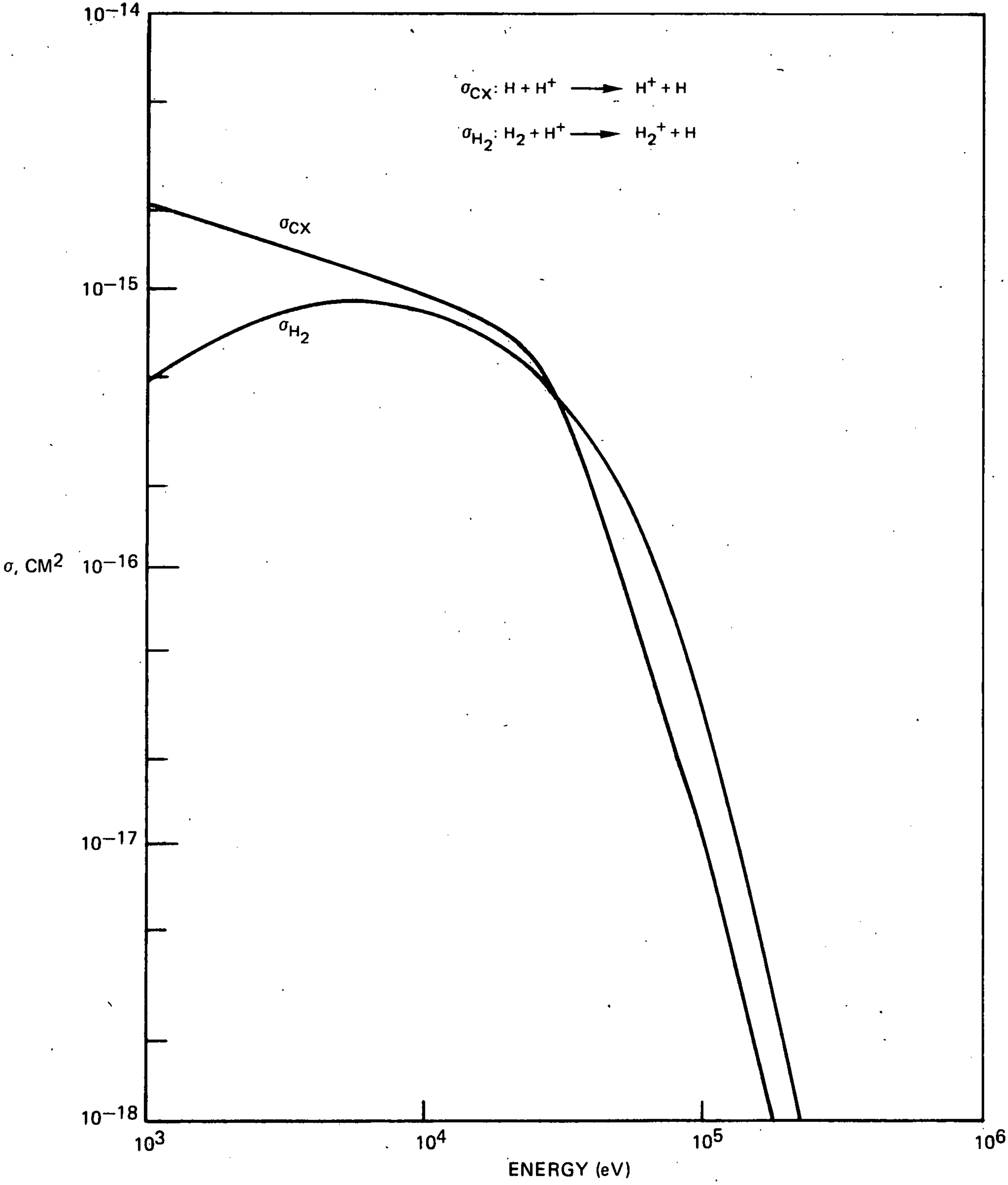

IONIZATION CROSS SECTIONS

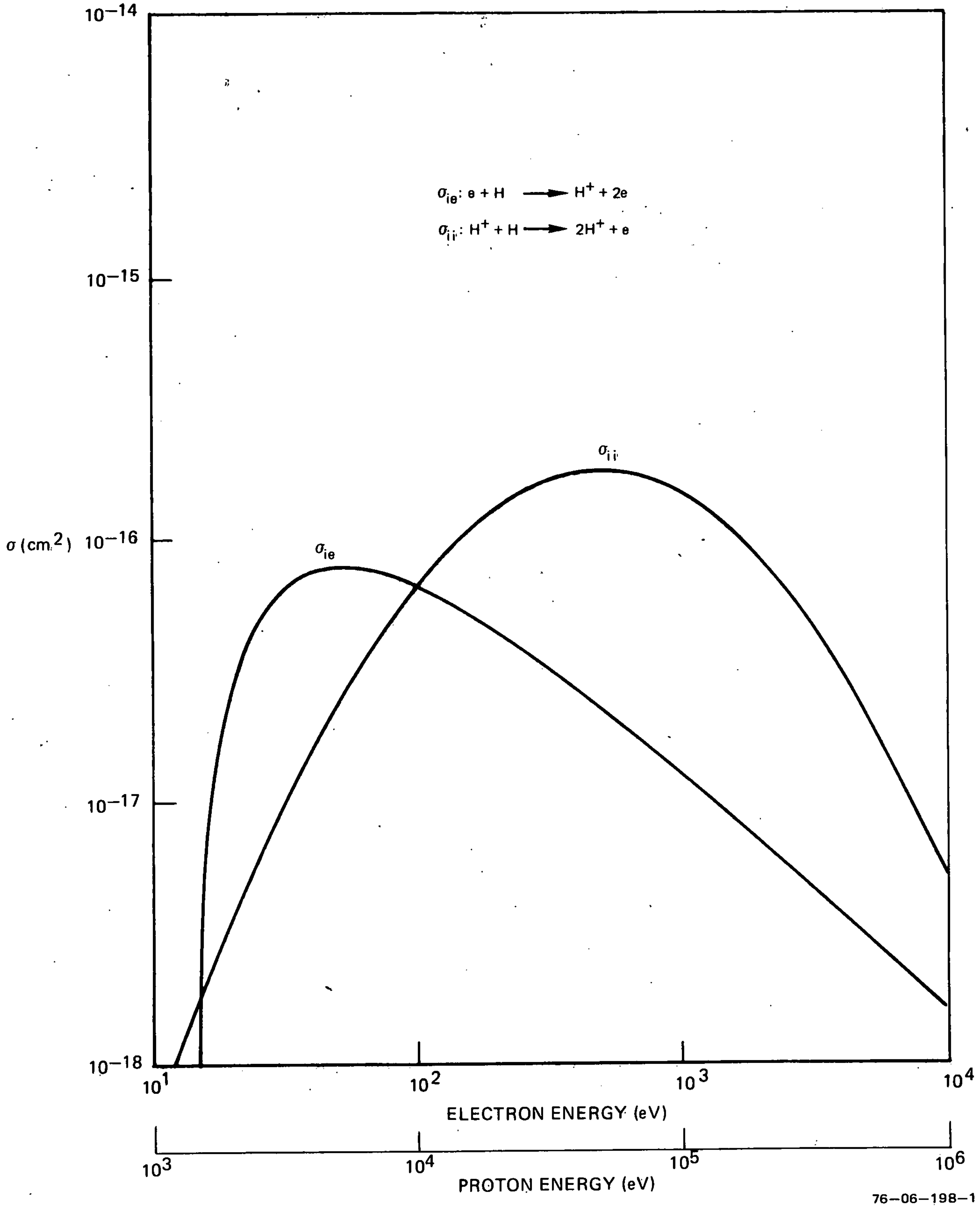

76–06–198–1

FIG. 16

CALCULATED DENSITY OF TRAPPED HOT IONS VS TIME

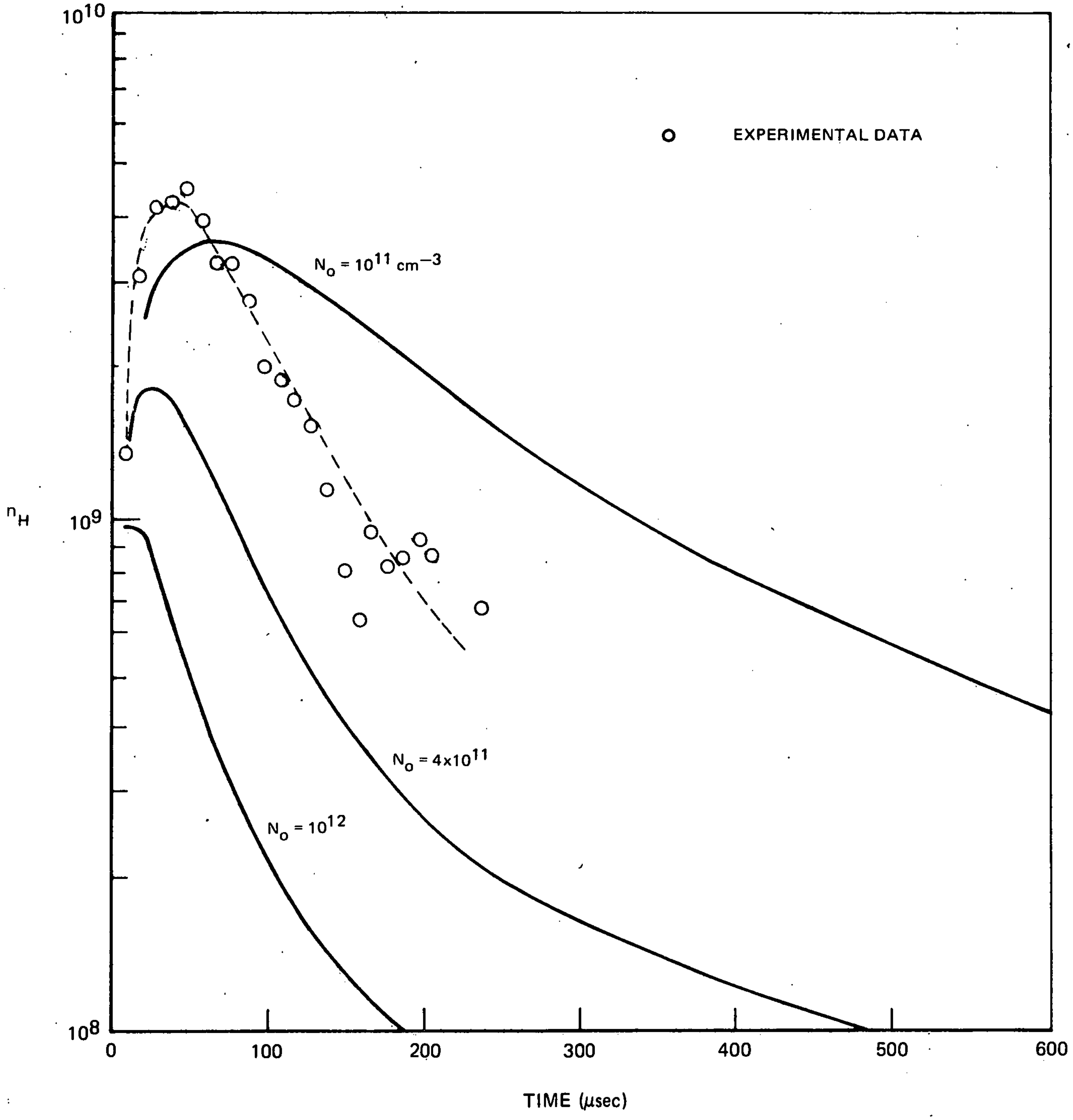

76–06–198–3

UTRC 76-93

Part III

STREAMING PLASMA STABILIZATION REQUIREMENTS IN LITE

Walter J. Fader, Raynard A. Jong, and Arthur E. Mensing
United Technologies Research Center

June, 1976

STREAMING PLASMA STABILIZATION REQUIREMENTS IN LITE

Walter J. Fader, Raynard A. Jong, and Arthur E. Mensing

Target plasma confinement experiments in LITE have displayed an enhanced loss of the LiH target plasma accompanied by copious bursts of rf radiation several hundred microseconds into the target decay (Ref. 1) as shown in Fig. 1. Although the wavelength and phase velocity of the rf activity have not been measured, comparisons with measurements in 2XII-B, PR-6 and PR-7 (Refs. 2, 3, 4) suggest that the drift cyclotron loss cone instability is present and accounts for the rapid loss of density.

Recent advances in mirror theory (Ref. 5) predict that the drift cyclotron loss cone instability can be controlled by the introduction of a warm streaming plasma (Ref. 6). Experiments on PR-6, PR-7, and 2XII-B (Refs. 3, 4, 6) confirm the stabilizing effect of the warm stream. Furthermore, experiments on 2XII-B (Ref. 7) and recent measurements in LITE showed that stable plasma decays could be obtained for plasmas in a high ambient gas density environment. In the LITE measurements, N_2 gas bled into the vacuum chamber raising the background pressure during the experiment, resulted in stable plasma decays as shown by the smooth density decay and absence of rf activity in Fig. 2 (Ref. 1). On the basis of these observations, it is expected that a warm plasma stream would serve to stabilize the target plasma decay in LITE. Calculations to estimate the warm plasma current necessary for stabilization of the LITE plasma and the development of a steady state ion source to supply the warm stream for the long duration experiments of interest in LITE are described in this report.

I. Warm Plasma Current Required for Stabilization

Baldwin, Berk, and Pearlstein (Ref. 5) have developed a quasilinear model which describes the time evolution of a mirror confined plasma unstable to the drift cyclotron loss cone mode (DCLC) and have estimated the warm plasma density required to stabilize the mode. The loss cone mirror confined hot plasma and accompanying warm component are modeled by the distribution function

$$\begin{aligned} F(v_\perp) &= F\ (v_\perp) + F_W(v_\perp) \\ &= \frac{2n_H}{v_H^2 - v_h^2}\left\{\exp(-v_\perp^2/v_H^2) - \exp(-v_\perp^2/v_h^2)\right\} + \frac{2n_W}{v_W^2}\exp(-v_\perp^2\, v_W^2) \end{aligned} \tag{1}$$

where v_H is the thermal velocity of the hot ions, and v_W is the thermal velocity of the warm stream.

The size of the loss cone hole in the hot ion distribution is expressed by a "hole velocity", v_h , which in terms of the plasma potential, Φ, and the ion mass M, is

$$\frac{1}{2} M v_h^2 = Ze\Phi \ . \tag{2}$$

The two components of the distribution function, F_H and F_W are shown schematically in Fig. 3 along with the total distribution function, F. The velocity v_h^* is defined by the minimum in the distribution function F, i.e., $\left.\frac{\partial F}{\partial v_\perp}\right)_{v_h^*} = 0$. In the analysis that follows, particles with $v_\perp < v_h^*$ are considered part of the warm streaming plasma, while particles with $v_\perp > v_h^*$ are taken to be part of the hot population.

For the distribution function of Eq. 1, Baldwin, et al (Ref. 5) have estimated the minimum warm density fraction, $\Delta(= {}^{n}W/n_H)$ required to stabilize the DCLC mode as

$$\Delta \simeq \frac{1}{2}\left(\frac{v_h}{v_H}\right)^2 << 1 \ . \tag{3}$$

To translate this requirement on the density fraction into a streaming source strength, we must follow the time evolution of the plasma. From Ref. 5, the evolution of the distribution function $F(v_\perp, t)$ is described by the relation

$$\frac{\partial F}{\partial t} = \frac{1}{2v_\perp}\frac{\partial}{\partial v_\perp} v_\perp\left[v_\perp \frac{F}{\tau_D} + \frac{D}{2}\frac{\partial F}{\partial v_\perp}\right] - \left[\int_0^\infty v_\perp dv_\perp \, S_{cx}(v_\perp) + \nu_L(v_\perp)\right]F \tag{4}$$

$$+ n\left[S_i(v_\perp) + S_{cx}(v_\perp)\right] + S_o(v_\perp) \ .$$

In this equation, S_i and S_{cx} are the sources of particles due to ionization and charge exchange of a neutral beam, and are taken as zero in the case we are considering (target plasma and warm stream only). τ_D is the electron drag time, $D(v_\perp, t)$ is the velocity space diffusion due to fluctuations, S_o is the source of low energy stream particles, and n is the particle density given by $n = \int v_\perp \, dv_\perp \, F(v_\perp)$. The loss rate $\nu_L(v_\perp)$ is approximately the inverse transit time for untrapped particles.

The time behavior of the warm and hot ion densities are obtained by taking the zeroth moment of Eq. 4. Since the source of streaming particles supplies only low energy ions,

$$S_o(v_\perp) = 0 \quad \text{for } v_\perp > v_h^* \ . \tag{5}$$

The loss rate $\nu_L(v_\perp)$ models the finite loss time required for ions which cross the loss cone boundary to be lost from the system. Assuming that electron drag dominates over diffusion in velocity space, particles are only lost at low energy, i.e.,

$$\nu_L(v_\perp) = 0 \quad \text{for} \quad v_\perp > v_h^* \tag{6}$$

and we can for simplicity model the loss rate by the relation

$$\nu_L(v_\perp) = \frac{v_h^*}{L_p} \; H(v_h^{*2} - v_\perp^2) \tag{7}$$

where L_p is the half length of the mirror and H is the unit step function. For simplicity in notation, the warm stream source term is denoted by

$$\left.\frac{\partial n_w}{\partial t}\right)_s \equiv \int_0^{v_h^*} S_0(v_\perp) \; v_\perp dv_\perp \; . \tag{8}$$

Taking the zeroth moment of Eq. 4 with the restrictions noted above, the hot and warm ion densities satisfy the relations

$$\frac{\partial n_H}{\partial t} = - {v_h^*}^2 \frac{F(v_h^*)}{2\tau_D} \tag{9}$$

$$\frac{\partial n_w}{\partial t} = \frac{v_h^{*2}}{2\tau_D} F(v_h^*) - \int_0^{v_h^*} \nu_L(v_\perp) F(v_\perp) \, v_\perp dv_\perp + \left.\frac{\partial n_w}{\partial t}\right)_s \; . \tag{10}$$

Using Eq. (7) and $\Delta = n_w/n_H$, the equation for the time behavior of the warm streaming source (Eq. 10) can be rewritten as

$$\left.\frac{\partial n_w}{\partial t}\right)_s = \frac{v_h^*}{L_p} n_w - \frac{(1+\Delta)}{2} \frac{v_h^* F(v_h^*)}{\tau_D} \tag{11}$$

where v_h^* is evaluated by differentiating Eq. (1) with $v_\perp = v_h^*$ to obtain

$$\frac{-1}{v_H^2 - v_h^2} \left\{ \frac{v_h^*}{v_H^2} \exp\left(-\frac{v_h^{*2}}{v_H^2}\right) - \frac{v_h^*}{v_h^2} \exp\left(-\frac{v_h^{*2}}{v_h^2}\right) \right\} = \frac{\Delta v_h^*}{v_w^4} \exp\left(-\frac{v_h^{*2}}{v_w^2}\right) \; . \tag{12}$$

Recalling Eq. (3), the expression for v_h^* is

$$v_h^{*2} \simeq \frac{v_w^2 v_h^2}{v_h^2 - v_w^2} \, \ln\left(\frac{1}{2} \frac{v_h^4}{v_w^4} \frac{v_H^2 - v_h^2}{v_H^2}\right) . \tag{13}$$

Since

$$v_H^2 >> v_h^2$$
$$v_h^4 > 2 v_w^4 \tag{14}$$

Eq. (13) can be approximated by

$$v_h^* \lesssim v_h \tag{15}$$

and the distribution function is approximated by

$$F(v_h^*) \simeq \frac{2\,n_H}{v_H^2} \ . \tag{16}$$

Substituting in Eq. 11, the warm streaming source becomes

$$\left.\frac{\partial n_W}{\partial t}\right)_S \simeq \frac{n_H}{2}\,\frac{v_h^2}{v_H^2}\left\{\frac{v_h}{L_p} - \frac{2}{\tau_D}\right\} \ . \tag{17}$$

The electron drag time is the Spitzer electron-ion energy equilibration time and has the form

$$n\tau_D \simeq 3.87 \times 10^{11}\,\frac{A}{Z^2}\,E_e^{3/2} \tag{18}$$

where A is the mass number and E_e is the electron energy in keV. For a hydrogen plasma with 500 eV ions and 25 eV electrons in a plasma potential of 80 eV, (Ref. 8) the following values for the parameters are obtained:

$$n\tau_D \simeq 1.53 \times 10^9 \text{ cm}^{-3}\text{ sec}^{-1}$$

$$v_h = 1.24 \times 10^7 \text{ cm/sec}$$

$$\left(\frac{v_h}{v_H}\right)^2 = .16 \ .$$

Using these parameters the density input rate of the warm stream can be evaluated from Eq. 17 for the mirror half length, L_p = 16 cm of the LITE containment field. The resulting density input rate and the current required to supply this input over the .4 liter volume of the LITE target plasma are tabulated in Table I as a function of the hot ion density.

Table I

Streaming Plasma Requirements in LITE with H^+ Target Plasma

n_H	$\left.\frac{\partial n_W}{\partial t}\right)_S$	I
10^{11}cm^{-3}	6.2 x 10^{15} cm^{-3} sec^{-1}	.40 amperes
10^{12}	6.2 x 10^{16}	4.0
10^{13}	6.1 x 10^{17}	39.

To the extent that the laser produced target plasma in LITE contains a significant fraction of Li ion as indicated by recent calculations (Ref. 8) and measurements on LITE, it is of interest to evaluate the streaming plasma current required to stabilize a Li dominated target plasma. The effect of the Li ions is to alter the hole in the hot ion distribution which determines the fraction Δ of warm to hot plasma density. Assuming a Li energy of 1.1 keV, the current requirements to stabilize a Li^+ and a Li^{+++} plasma are summarized in Table II.

Table II

Streaming Plasma Requirements in LITE with Li^+ and Li^{+++} Target Plasma

n_H	$\left.\frac{\partial n_w}{\partial t}\right)_s$ Z = 1	I	$\left.\frac{\partial n_w}{\partial t}\right)_s$ Z = 3	I
$10^{11} cm^{-3}$	$1.05 \times 10^{15} cm^{-3} sec^{-1}$	.068 amp	$5.57 \times 10^{15} cm^{-3} sec^{-1}$	.36 amp
10^{12}	1.04×10^{16}	.68	5.54×10^{16}	3.6
10^{13}	1.00×10^{17}	6.5	5.43×10^{17}	35.

The Li dominated plasmas have a smaller hole velocity, v_h, and consequently, a smaller hole in the velocity distribution function. Since less warm plasma would be needed to fill the smaller hole, compared with the results for a pure H plasma, the warm stream current required for stabilization is slightly less for a Li^{+++} plasma and substantially reduced for a Li^+ plasma.

For the steady state injection sustained plasma, the warm streaming current requirement is much less than that required for the target plasma at the same density. The hot ion energy is increased to $\gtrsim 10$ keV. Correspondingly, v_H^2 in Eq. (17) is increased by a factor of 20. Since the hole velocity is determined by the plasma potential, which is nearly a constant multiple of the electron energy, v_h^2 in Eq. (17) should not change by more than a factor of two. Hence the warm streaming current necessary to stabilize the target plasma at a density of $\sim 10^{12} cm^{-3}$ should stabilize the steady state plasma at a hot ion density of $\sim 10^{13} cm^{-3}$.

II. Steady State Streaming Plasma Source on LITE

The warm stream current calculations of Sect. I indicate that to stabilize the LITE plasma in the density range $n_H \gtrsim 10^{12}$ cm^{-3}, a current of $\lesssim 5$ amps of warm streaming plasma is needed. The presence of the lithium ion component in the laser produced plasma initially decreases the warm straming current requirement; however, as the plasma evolves in time with neutral injection, the Li ions are lost and the H^+ population increases, so that the long term warm streaming current requirement is that evaluated for a pure hydrogen plasma.

Recent experiments in 2XII-B (Ref. 6) utilized a short pulse "washer gun" plasma source directed axially into the plasma for warm plasma stabilization; in the LITE experiment where run times are 1 to 2 sec, such a "washer gun" is not an appropriate source since it is limited by arc heating to pulse lengths of approximately 5 msec. To provide the long pulse (1-2 sec) warm streaming plasma source for stabilization of the confined LITE plasma, a DuoPIGatron arc source is installed in the center of the top of the LITE experiment chamber along the axis of the magnetic confinement field as shown in Fig. 5. The arc source is the arc portion - cathode, anodes, and expansion chamber - of a 7-cm ORMAK ion source obtained from ORNL (see Fig. 6). The source, which has the capability of cw operation, is mounted atop an interface vacuum chamber containing a 10 cm dia. aperture between the vacuum chamber and the experiment chamber. The vacuum chamber contains two 8-inch dia. ducts, each connected to a 6-inch diffusion pump with LN_2 baffles for removal of the gas efflux from the arc plasma source. The pumping speed of the two baffled pumps is 5000 ℓ/sec. A 12-inch valve connects the system to the experiment chamber so that changes to and tuning of the arc source can be made without affecting the experiment chamber vacuum. The arc is powered by a 70 A, 150 V dc resistive ballasted unregulated power supply capable of either cathode or anode ground operation. The magnet and filament supplies are as shown in Fig. 6. The hydrogen flow rate into the arc chamber is 3.5 T-ℓ/sec resulting in an arc chamber pressure of 50 μ. With the specified gas flow rate and the pumping speed of the diffusion pumps, the pressure in the vacuum chamber between the experiment chamber and the arc source is 7×10^{-4} T. The hydrogen gas flow rate is approximately twice that employed when the 7-cm source was used as an ion source on ORMAK. The removal of the extraction electrodes reduces the flow resistance, and unless the flow is increased the pressure in the arc chamber would be too low to generate the proper arc. A piezoelectric valve in the gas feed line provides rapid and programmed control of flow into the arc source. Provision has been made for incorporation of a guide magnetic field to couple the streaming plasma flow from the plasma source into confinement region. However, a guide field is not presently installed as test stand operation of the source with a solenoidal magnet installed downstream of the source and producing 70 Gauss axial field at the arc exit plane produced significant channeling of the arc output plasma. Since this field intensity is approximately the same as that generated by the confinement field at the arc location, the confinement field alone should serve to channel the arc source warm plasma output into the target plasma region. These tests also showed that with a magnetic field present, grounded anode operation of the arc source resulted in more effective channeling and higher axial streaming plasma flux. In operation on LITE, the production of the warm streaming plasma will be synchronized with the laser target plasma formation. The 7-cm arc source can be pulsed from 0 to full current in < 2 msec. The gas valve will be opened approximately 10 msec prior to firing the arc to provide sufficient time for pressure buildup in the arc chamber. These necessary time delays have been incorporated into laser, magnet, and neutral beam firing sequences so that both the warm streaming plasma and the energetic neutral beam will arrive in the plasma confinement region simultaneously with the production of the target plasma.

Test stand operation of the source has been carried out to measure the plasma density and, hence, the current of the warm plasma issuing from the arc source. Langmuir probes were installed in the plasma stream, and by applying a negative bias voltage to the probe, the ion density was determined by the method of Ref. 9. Two Langmuir probes separated by 120 cm were used to measure the time of flight and hence the ion velocity. With the arc operating at 40 amps (grounded anode mode) and with a gas flow rate of 3.5 T-ℓ/sec an ion density of 10^{11} cm^{-3} was determined at a position 35 cm downstream of the 10 cm dia. aperture. Time of flight measurements showed the ion energy to be ~ 10 eV. The density and energy result in a current density of 64 mA/cm^2. Measurements showed a uniform ion density throughout the 10 cm dia. apertured area in these no magnetic field tests, giving a total output current of 5 amps. The 5 amp output of the 7-cm ORMAK ion source matches the streaming plasma requirement determined from the calculations of the preceding section. The arc source was operated at 40 A arc current in these tests; arc currents up to 70 A are available from the power supply providing reserve output current capability for the LITE streaming plasma stabilization experiments.

REFERENCES

1. Ard, W. B., J. H. Stufflebeam and R. G. Tomlinson: Magnetic Confinement of Laser Produced LiH Plasma in LITE, UTRC 76-98, June 1976.

2. Simonen, T. C.: Identification of an Ion Cyclotron Instability in a Mirror Confined Plasma. Lawrence Livermore Laboratory Report UCRL-76115, October 1974.

3. Baiborodov, Y. T., M. S. Ioffe, B. I. Kanaev, R. I. Sobolev and E. E. Yushmanov: Nuclear Fusion Supplement, 1972, p. 219.

4. Gott, Y. V, M. S. Ioffe, B. I. Kanaev, A. G. Motlich, V. P. Pastukhov, and R. I. Sobolev: Nuclear Fusion Supplement, 1975, p. 55.

5. Baldwin, D. E., H. L. Berk and L. D. Pearlstein: Phys. Rev. Letters, 36, 1051 (1976).

6. Coensgen, F. H., W. F. Cummins, B. G. Logan, A. W. Molvik, W. E. Nexsen, T. C. Simonen, W. C. Turner: Seventh European Conference on Controlled Fusion and Plasma Physics, Sept. 1-5, 1975, Lausanne, Switzerland.

7. Coensgen, F. H., W. F. Cummins, A. W. Molvik, W. E. Nexsen, T. C. Simonen, and B. W. Stallard: Plasma Physics and Controlled Nuclear Fusion Research, Vol. I, IAEA, Vienna, 1975. p. 323.

8. Haught, A. F., D. H. Polk, W. J. Fader, R. G. Tomlinson, R. A. Jong, W. B. Ard, A. E. Mensing, T. L. Churchill, J. H. Stufflebeam, F. J. Bresnock: High Beta Capture and Mirror Confinement of Laser Produced Plasmas, UTRC R76-953200-24, COO-2277-7, semiannual report, Jan., 1976, prepared under Contract E(11-1)-2277 for the USERDA.

9. Cobine, J. D.: Gaseous Conductors, Dover Publications, Inc., N.Y., 1958.

LIST OF FIGURES

FIG. 1

UNSTABLE PLASMA DECAY

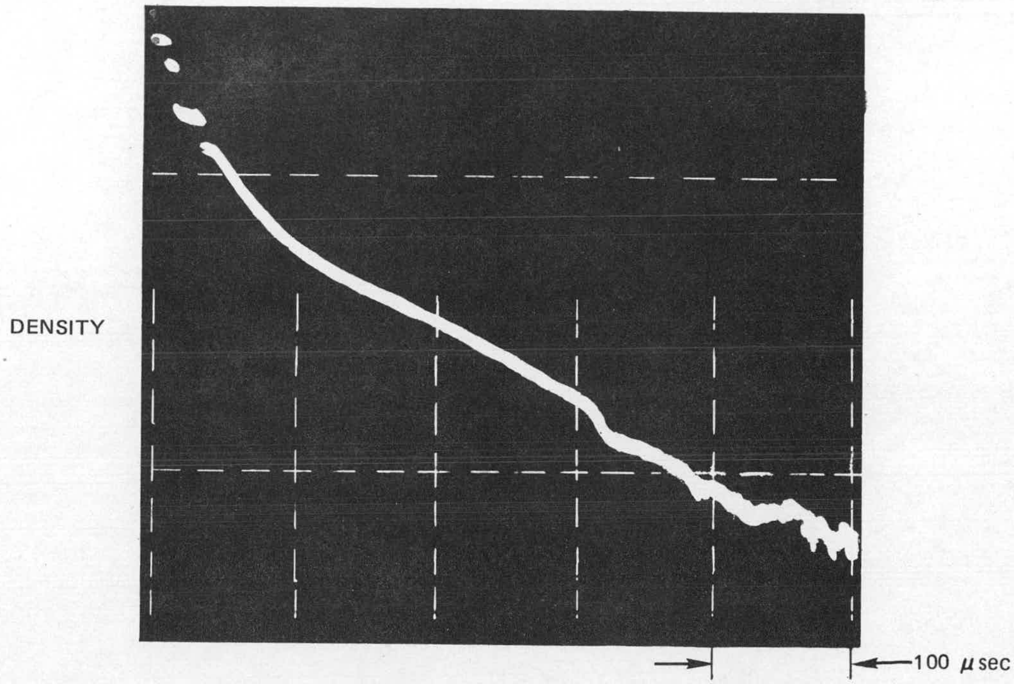

DENSITY TIME HISTORY

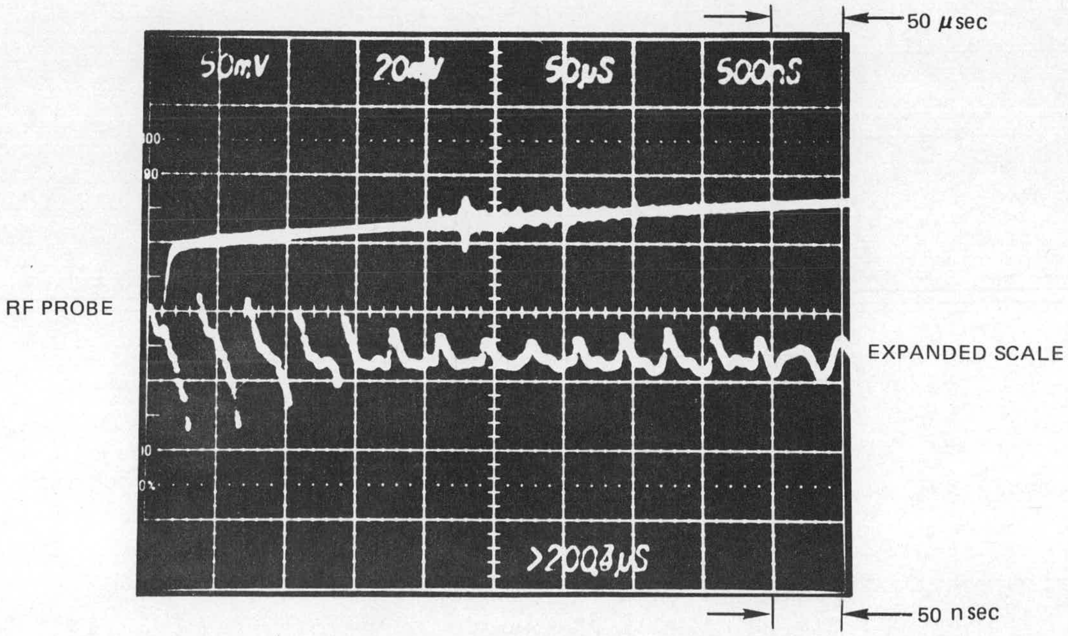

RF EMISSION

FIG. 2

STABLE PLASMA DECAY

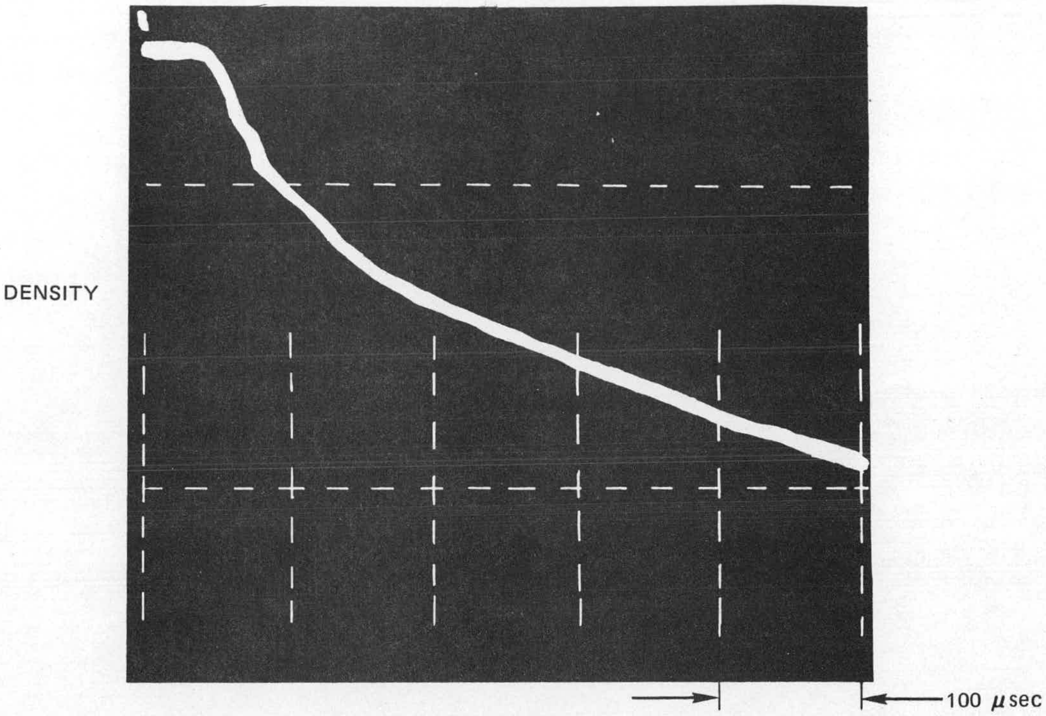

DENSITY TIME HISTORY

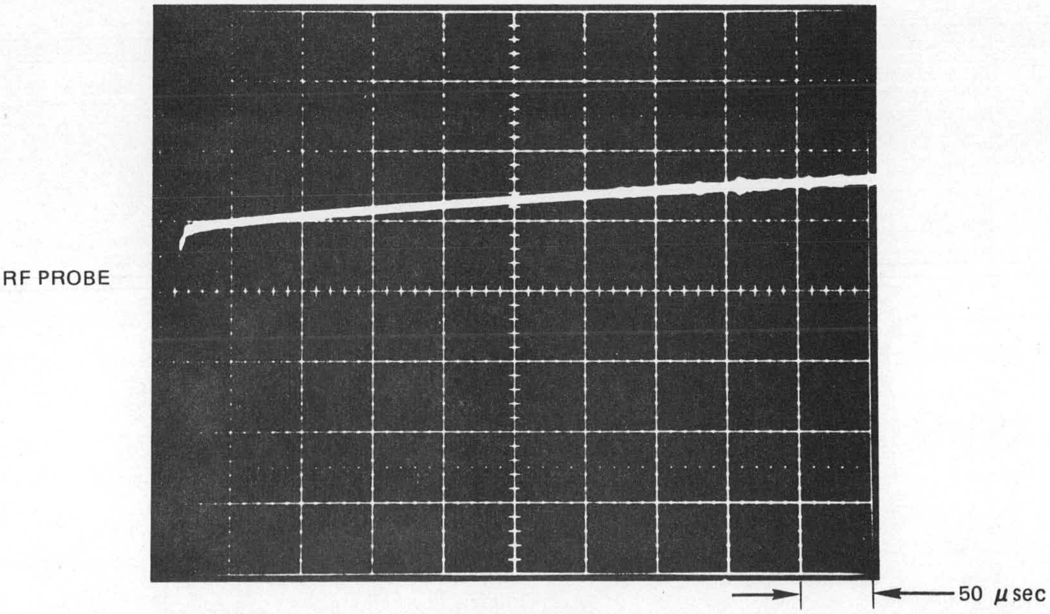

RF EMISSION

MODEL DISTRIBUTION FUNCTION

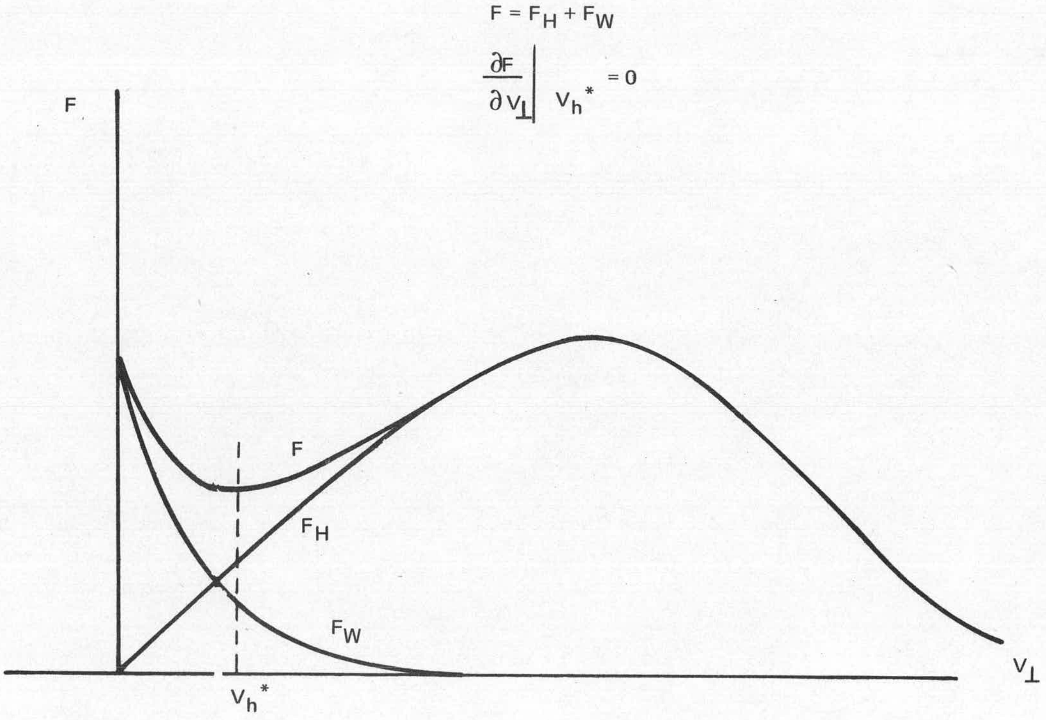

FIG. 4

WARM STREAMING CURRENT REQUIREMENTS IN LITE

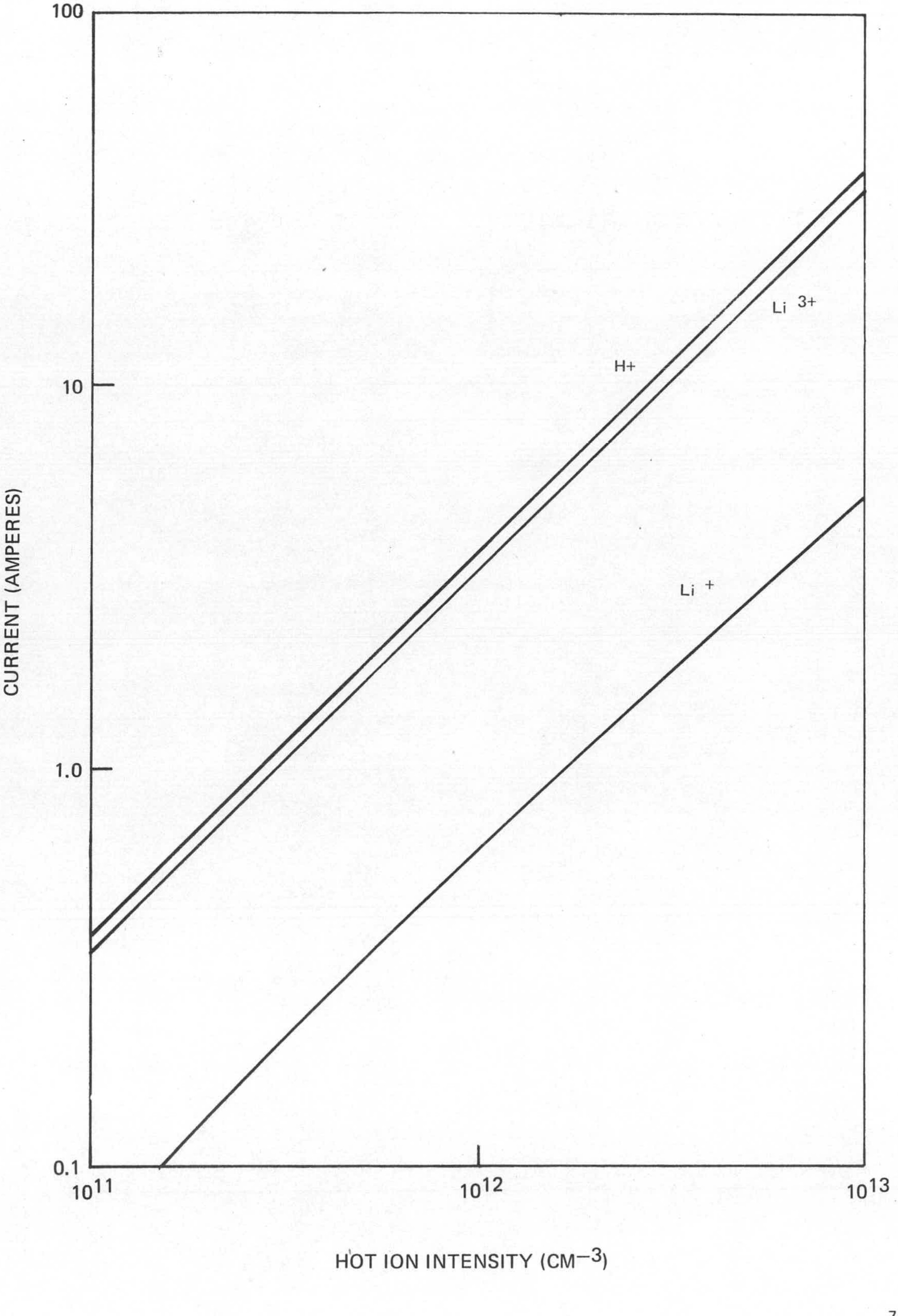

76–06–112

LITE FACILITY WITH STREAMING PLASMA STABILIZATION SOURCE

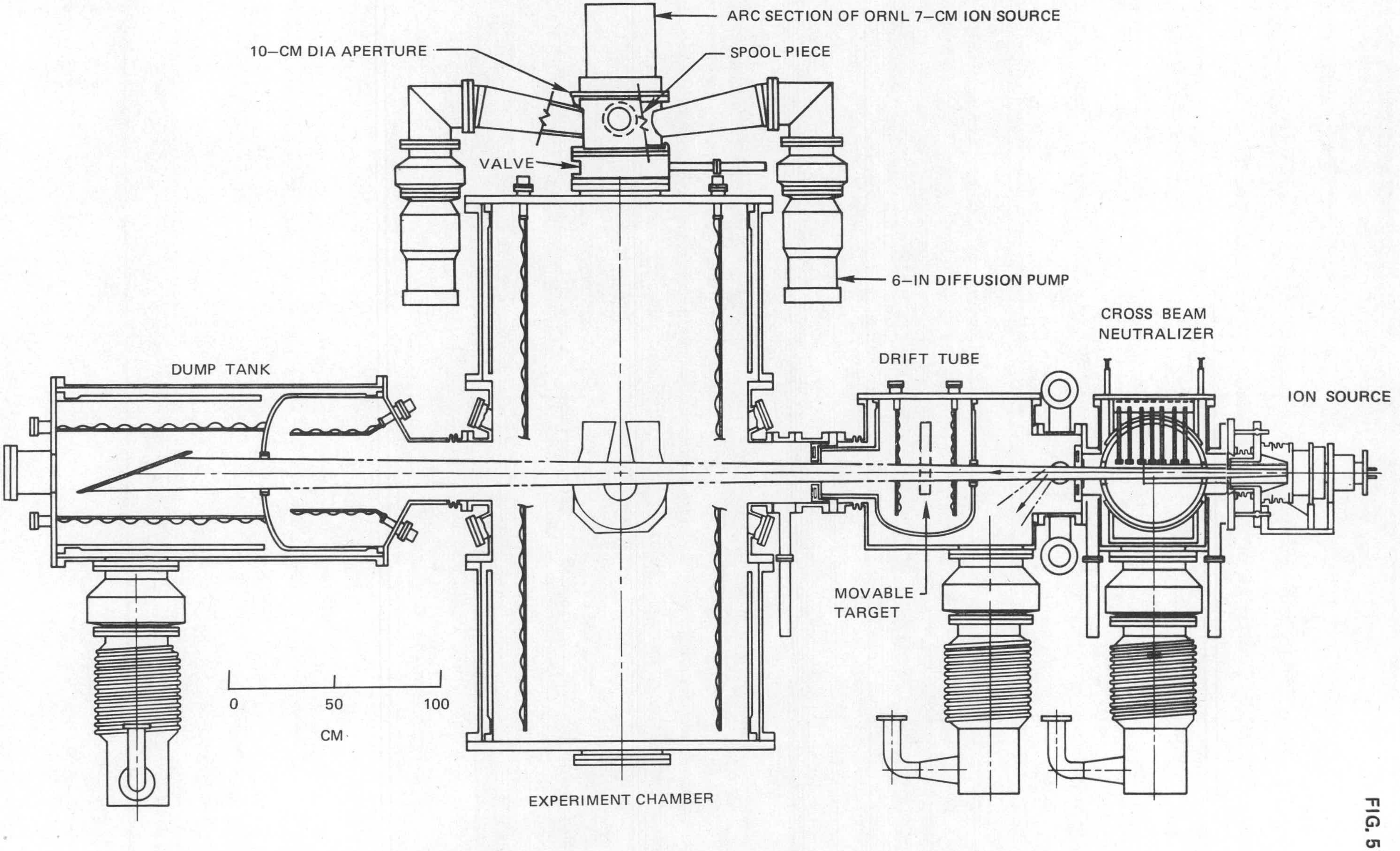

76–06–180–1

FIG. 5

FIG. 6

ARC SECTION OF ORNL 7 CM DUOPIGATRON ION SOURCE

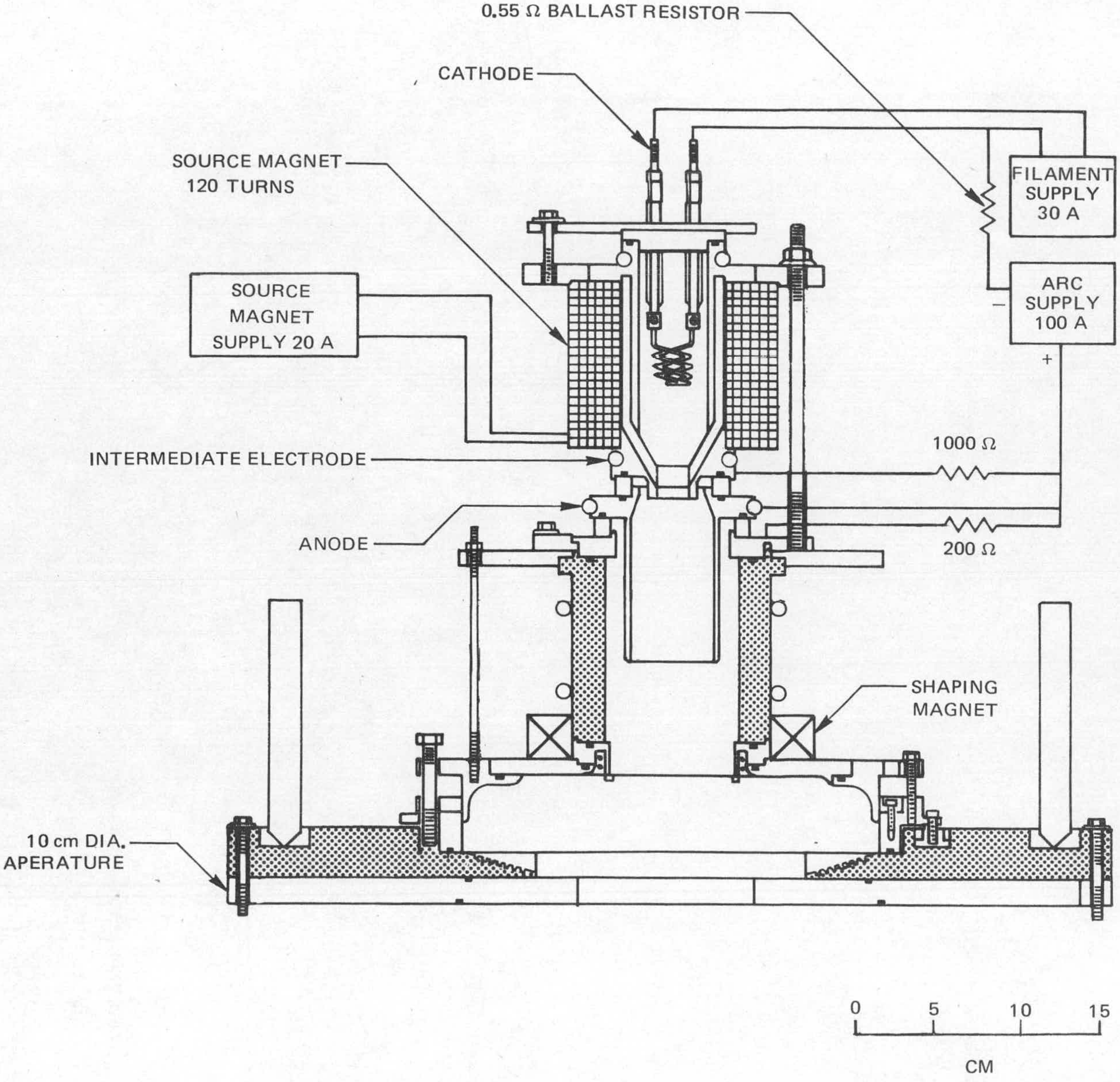

76–06–180–2

UTRC 76-91

Part IV

LITE NEUTRAL BEAM LINE UPGRADE

Thomas L. Churchill and Arthur E. Mensing
United Technologies Research Center

June, 1976

LITE NEUTRAL BEAM LINE UPGRADE

Thomas L. Churchill and Arthur E. Mensing

Abstract

The neutral beam line on the Laser Initiated Target Experiment (LITE) is being upgraded to increase the injection capability by a factor of 50. Described herein are the ion source and power conditioning necessary to achieve this goal. Also described are the anticipated performance figures of the new beam line including the impact of the increased gas load on the system vacuum levels.

Introduction

The Laser Initiated Target Experiment (LITE) at the United Technologies Research Center is designed to address the target plasma buildup approach to a steady state mirror fusion device. A dense, mirror confined, target plasma is produced by high power laser irradiation of a solid lithium hydride particle, electrically suspended in a vacuum at the center of an established minimum-B magnetic field. Following expansion in and capture by the magnetic field, this target plasma is irradiated by an energetic neutral hydrogen beam. Charge exchange collisions with energetic beam particles serve to heat the confined plasma while ionization of the neutral beam atoms and trapping in the mirror magnetic field add particles to the confined plasma. For sufficiently high beam intensities, confined plasma losses will be offset so that buildup of the plasma density occurs, thus demonstrating sustenance and fueling as well as heating by neutral beam injection of a steady state mirror fusion device.

Neutral beam injection experiments have been conducted on LITE employing a MATS III ion source (Ref. 1). With this source 10-12 keV neutral hydrogen beams have been injected with beam current densities up to 3 mA/cm^2 (equivalent) into 400 cc laser produced plasmas. Total injected beam power levels have approached 3 kilowatts. These injection experiments at the 3 mA/cm^2 level have been directed toward investigations of the initial charge-exchange heating phase of the injection. Future experiments on plasma buildup in LITE are calculated to require much higher (> 15 mA/cm^2) energetic neutral beam intensities. As a result, the LITE neutral beam line is being upgraded, and in this report are described the ion source and power conditioning system for generating the required higher beam current in LITE. The anticipated neutral beam parameters both at the ion source and the target plasma are presented along with the impact on vacuum levels that is expected to result from the increased gas load.

Neutral Beam Source

The ion source most readily adaptable to the special requirements of the LITE neutral beam line (i.e., quasi-cw or long pulse operation) is the proven duoPIGatron ion accelerator developed at the Oak Ridge National Laboratories (Ref. 2). A 15 cm version of the ORNL source has been designed, constructed and preliminarily tested by ORNL to meet the LITE beam line requirements. A cross section drawing of the source is shown in Fig. 1.

Based on ORNL experience with the 10 cm ORMAK ion sources and on preliminary test stand experience at ORNL with the 15 cm LITE ion source, it appears that the ion source parameters shown in the following table are conservative estimates of anticipated performance (Ref. 3).

Table I

15 cm Ion Source Parameters

Net Accelerating Voltage	15-27 kV
Net Extracted Current	15-30 A
Atomic Component	60 %
Molecular Component	40 %
Beamlet Half-Angle Divergence	1°
Beamlet Stacking Factor	80 %
Gas Utilization Efficiency	50 %

Neutralization of the extracted ion beam will be accomplished by the usual method of self-neutralization in which a tubular gas cell is affixed to the downstream electrode of the ion source (Fig. 1); neutralization occurs by charge exchange of the ion beam with the un-ionized gas that effuses from the ion source. The neutralizer efficiency (defined as the ion flux fraction that emerges as fast neutrals) depends on the gas density-length product of the neutralizer in conjunction with an array of energy-dependent charge-exchange cross sections. It happens that the cross section for dissociative charge exchange of diatomic ions (the principle molecular ion component) is considerably higher than for the direct charge exchange of protons (Refs. 4 and 5). Consequently, the neutralizer length is established for proton neutralization. In the energy range of interest for LITE (Table I), it is found that a 100 cm gas cell neutralizer is adequate to provide near equilibrium proton neutralization (the condition where forward and reverse charge changing processes are just balanced). Employing the data of Table I in conjunction with calculated neutralization efficiencies for a 100 cm neutralizer, the following table was prepared to illustrate the neutral beam parameters that can be expected from the 15 cm ORNL ion source on LITE.

Table II

Expected Neutral Beam Parameters

	15 keV	27 keV
Net Input Current (to Neutralizer)	15 A	30 A
Atomic Component (60%)	9 A	18 A
Molecular Component (40%)	6 A	12 A
Neutralizer Efficiency (Atomic)	0.75	0.70
Neutralizer Efficiency (Molecular)	0.92	0.88
Full-Energy Atomic Current (Equivalent)	6.75 A	12.60 A
Half-Energy Atomic Current (Equivalent)	11.04 A	21.12 A
Total Atomic Current (Equivalent)	17.79 A	33.72 A
Full-Energy Beam Power	101.2 kW	340.2 kW
Half-Energy Beam Power	82.8 kW	285.1 kW
Total Beam Power	184.0 kW	625.3 kW
Average Beam Energy	10.35 keV	18.54 keV

It should be noted of Table II that approximately two-thirds of the total neutral current resides in the half-energy component. In a relatively small volume plasma such as LITE where 10-15 keV represents the adiabatic neutral beam energy limit (defined as the energy where the ion gyroradius becomes comparable to the plasma radius) it may be beneficial to operate the ion source at increased energy in order to take advantage of the larger half-energy component.

In designing a neutral beam injector, the extraction apertures are configured to "aim" the individual beamlets at a common point such as the center of the target plasma. However, practical machining tolerances limit the accuracy to which the beamlets can be made to superpose, resulting in a stacking factor (Table I). In addition, each beamlet diverges and, in so doing, assumes a transverse Gaussian intensity profile, the half-intensity radius of which defines the half-angle of the beamlet divergence (Table I). At large distances and with many beamlets (there are 861 beamlets in the 15 cm LITE source), the overall beam remains Gaussian with its width broadened by the stacking factor. On the basis of the anticipated ion source and neutral beam parameters (Tables I and II), it is possible to generate the expected neutral beam current density profiles at the center of the target plasma for various geometric focal distances. In LITE competing combinations of beam intensity fall-off, confinement magnet edge fields, and ion source cold gas streaming fluxes result in a compromise ion source focal length of between 250 and 350 centimeters. The radial profiles of neutral beam current density for both focal distances are shown in Fig. 2. Both the distance dependent beam broadening and the inverse square of distance fall-off are evident in the figure. Also shown in Fig. 2 are the polar integrals of current density to indicate the inventory of total current within a given radius. In order to satisfy physical constraints and match the effective radius of the LITE target plasma, the neutral beam will enter the LITE experiment chamber through a 10 cm diameter aperture. The penalty in beam current loss incurred by skimming the diverging beam with the aperture is evident in Fig. 2; the remaining current fraction will be 0.41 and 0.24 at 250 and 350 centimeters, respectively. Injection beam power, proportional to beam current, will be reduced accordingly from the levels indicated in Table II.

As indicated above stray magnetic fields from the LITE confinement magnet were a consideration in establishing a viable range of neutral beam focal lengths. Measurements of this field in the vicinity of the MATS III ion source (300 cm from the target plasma) have indicated transverse flux densities in excess of 10 Gauss. Therefore, in order to retain the inherent beam optical properties of the ion source and to prevent beam deflection it will be necessary to attenuate this field to lesser levels. The actual degree of attenuation necessary depends on the acceptable limit of beam deflection. For example, it is reasonable to limit beam deflection at the target plasma to 10 percent of the target diameter which corresponds to 2.9 milliradians at 350 cm. It is just as reasonable to limit deflection to 10 percent of the beamlet half-angle divergence (Table I) or 2 milliradians in order to preserve stacking factor and avoid complicated machining corrections of the extraction apertures.

An estimate of the required flux density attenuation may be derived assuming deflection occurs in the neutralizer. Beam ions must, on average, travel half the length of the neutralizer ($L/2$) before being neutralized. Using a small angle approximation, $\phi R = L/2$, where ϕ is the deflection angle and R is the gyroradius of an ion of energy V in field B. Considering a deflection limit of 2 milliradians and 15 keV protons, B in the neutralizer must be limited to 0.7 Gauss, corresponding to an attenuation factor in excess of 14. Since the degree of attenuation is not severe, shielding of the neutralizer and ion source will be accomplished with Co-netic* sheet metal. This material has sufficiently low retentivity to prevent progressive magnetization which would require periodic degaussing.

Power Conditioning System

The 15 cm ORNL ion source on the LITE beam line will be powered by a relatively sophisticated power condition system shown in block diagram format in Fig. 3. The system will be complete from power bus to ion source and will be operable either from a local control or in a subservient mode to the LITE master control. The following is a brief description of each subsystem of the power conditioning system shown in Fig. 3 beginning with a description of the ion source electrical characteristics which define the power conditioning system requirements.

---

*Designation of a particular product is by way of example and is not intended to imply that others equally suitable are not available.

a. Ion Source Characteristics

The ion source is a two-component device consisting of an arc plasma chamber for generating positive hydrogen ions and a three-electrode system for beam formation (Fig. 1). Since the ion acceleration must terminate at the laboratory ground potential, the arc chamber must be elevated to a potential equal to the desired net energy. Therefore, all of the power supplies and controls for generating the arc must float at the accel potential, and this common, floating reference is provided by the floating high voltage deck.

One of the most important components of the ion source is the decel grid which is positioned between the accel and ground electrodes (Fig. 1). The function of the decel electrode is crucial and is the reason for a strict control logic rule that "under no circumstances can the accel be on without a certain minimum level of decel potential." This results from the fact that high energy ions leaving the ground electrode enter the neutralizer colinear with unused gas jetting from the ion source, and passage of the beam through the jet results in significant ionization of the gas. If the above logic rule was violated, negatively charged particles including both low energy electrons and negative ions would form a back-directed beam which would stream into the ion source. Since the energy per particle would be equal to the accel potential, the resulting power and momentum deposited in the accel electrode and elsewhere would rapidly destroy the ion source.

Another important characteristic of the ion source is that the accel field exerts surface gradients on the accel and decel electrodes on the order of 100 kV/cm. The accel-decel spacing is significantly less than the mean-free-path for electrons ionizing hydrogen, thus precluding gas discharge breakdown. However, interelectrode vacuum sparks will occur, and the sparks may become power arcs if enough electrode material is vaporized to reduce the mean-free-path to less than the accel-decel electrode spacing. Such arcs usually will not self-extinguish and must be limited and, subsequently, controlled by the power conditioning system. However, sparks frequently do self-extinguish with a 0-100 percent fall time equal to the charged-particle transit time between the accel and decel electrodes. This time varies from 150 picoseconds for electrons (major charge carrier) to about 30 nanoseconds for copper ions. In both cases, current levels of up to several hundred amperes will be interrupted within nanoseconds. The resulting L(di/dt) in the interconnecting leads will be partially absorbed by the stray capacitance to ground of the leads, floating deck, accel switch, etc. However, very fast high voltage transients will propagate into every piece of equipment. Adequate transient protection has to therefore be included wherever sensitive components are used.

b. Accel Power Supply

The accelerator component of the ion source accounts for 90 percent of the neutral beam injector power. For example, the arc, filaments, and magnets of the source require approximately 60 kilowatts, collectively; the decelerator requires, at most, 20 kilowatts, but the accelerator requires 900 kilowatts.

Raw dc power is provided to the accelerator subsystem by the accelerator power supply (Fig. 3). In order to account for losses in the switch tube, the accelerator power supply is capable of delivering 30 kV at 30 A. Basically, the supply is a twelve-phase system with transformer primary control. The control range is 4-30 kV for the purpose of conditioning the ion source from initial low voltage to full operating levels.

c. Capacitive Filter

In order to absorb various transient voltage excursions in the accelerator subsystem, a capacitive filter is included. The energy storage capacity is adequate to absorb or provide current during switching of the accelerator and to absorb the inductively stored energy of the accelerator power supply (greater than 300 joules) with a voltage rise of less than 10 percent. In order to provide surge protection during snap-on or during a downstream fault, the filter contains appropriately selected current limiting resistors.

d. Crowbar

Downstream faults can occur by either wiring or switch tube failures. If such a failure should occur, catastrophic damage will be prevented by crowbarring both the capacitive filter and the power supply. By this procedure, the accelerator system can be aborted in a few microseconds. Basically, the crowbar is a triggerable pressurized gap. The firing trigger is initiated either locally in response to either an overvoltage or overcurrent condition or remotely in response to a command from the hardwired processor.

e. Accel Switch

Downstream of the series regulator is a high voltage hard tube switch. The primary purpose of this element is to serve as a fast disconnect between the power supply and the ion source. As indicated in the ion source description, internal breakdown frequently will occur between the accel and decel aperture grids of the ion source. Whenever such a breakdown occurs, the accel switch must sense the condition and, if warranted, open by switching to a nonconducting state. Subsequently, in a preprogrammed mode, the switch may reclose and sample for continuance of the arc. If the arc does not restrike, the ion source is automatically restored to normal operation, but, if the arc has not cleared or restrikes, the switch will recycle, repeating the procedure as frequently as dictated by the control system. Typical transition times for switching off and on are a few tens of microseconds.

f. Decel Power Supply

Negative voltage dc power is provided to the decelerator subsystem by the decel power supply. The unit is a conventional power supply capable of delivering 10 kV at 10 A, although normal loading will be on the order of 5 kV at 2 A. The surplus capability or stiffness will be required during accel turn-on and turn-off transitions. During such events, the ion beam will become highly defocused causing interception by the decel grid of high energy ions resulting in increased power dissipation. In order to prevent ion source damage, it is mandatory that the decel power supply be stiff enough to maintain decel voltage under all circumstances except a decel grid-to-ground fault.

g. Decel Switch

As indicated in the ion source description, the decel aperture grid of the ion source serves an extremely important protective role, and control of the decelerator grid voltage, accomplished by the decel switch, is critical. This is an extremely difficult task because essentially all ion source internal fault arcs originating on the accelerator grid will terminate on the negative decel grid, with a resultant tendency to drive the decel grid positive. To prevent such an occurrence, the decel grid will be electrically clamped to ground with a diode network. However, during an arc, the decel switch and power supply must be able to withstand a short-circuited condition since the decel switch cannot be opened anytime accel power is present. The only time the decel switch will be permitted to open is if there is both a decel fault to ground and the accel grid is unenergized. Whenever the accel grid is energized and the decel grid faults or for any other reason the decelerator grid voltage drops below a preset minimum value, fail-safe hardwired logic between the decel and accel switches forces the accel switch to disconnect the accel grid. Conversely, the accel switch is inhibited from turn-on until the decel grid achieves the preset minimum value.

h. High Voltage Deck

Power supplies for the arc, filaments and magnets of the ion source along with the hydrogen gas control must necessarily float at the accelerator potential. This is accomplished by installing the supplies on a high voltage insulated deck which receives three-phase 60 Hertz power through a high voltage isolation transformer. With the exception of the arc power supply, the high voltage deck supplies are conventional. The unconventional feature of the arc power supply results from the need to provide load (arc) stabilization. To accomplish this, the arc supply consists of a saturable reactor controlled transformer with a hybrid full-wave rectifier (half SCRs). The saturable reactor provides the nondissipative reactance ballasting necessary to control the arc and the hybrid rectifier serves to rapidly turn on and off the arc supply as required.

i. Status Monitor

Every subsystem of the netural beam injector power conditioning system (Fig. 3) will have status information of both interlock and diagnostic nature that must be collected and dispersed to appropriate parts of the control system. It is the function of the status monitor to accomplish this task. The bulk of the status information will be a myriad of interlocks on everything from enclosure doors to water flow switches. Information of this type will normally be used by the local control where it serves in an inhibit/enable capacity. However, occasionally, an interlock will signal a malfunction or "dangerous level" condition during a run. In this case, the information will be used by a hardwired processor, in which appropriate action is initiated. The remainder of the status information is diagnostic, appearing in both analog and digital form to serve both the control and data systems. Included are all time-varying signals such as temperature, pressures, vacuum levels, currents and voltages. Current and voltage information is available in wide bandwidth form to the hardwired processor as well as to the data acquisition system, thereby providing for high speed decision-making in the control system.

j. Local Control

It is the function of the local control to provide the means for operating the beam line independently of any other LITE system. From this point every aspect of the neutral beam line can be exercised (in proper order) including vacuum pumps, water, targets, and valves, as well as the neutral beam injector power conditioning system. The local control panel panel has all pertinent indicator lamps, gauges and meters enabling an operator to visually follow various events and to make manual parameter corrections.

k. Hardwired Processor

All commands issued from the local control to the neutral beam injector power conditioning system will be routed through a hardwired processor. Acting in a watchdog capacity, a partial function of the hardwired processor is to pass judgment on all commands and, on the basis of all (pertinent) status information, decide whether or not such commands can be allowed. Then, if the decision is negative, the processor provides a control panel indication of the reason for the disallowance such as an improper sequence, an inadequate level set, or an unsatisfied interlock.

It is also the responsibility of the processor to automatically initiate the proper shutdown sequence in the event of an abort. The decision as to which sequence to follow is made by the processor on the basis of the particular position in the run cycle sequence in conjunction with the status information. In general, because of the relative slowness of human responses, the operator will have no control over the sequence of events in an abort condition.

1. LITE Master Control

Whenever the neutral beam injector power conditioning system is to be operated in concert with the other LITE systems, the local control will become subservient to the LITE master control (Fig. 3). Under this condition, however, the hardware processor remains the watchdog and decision-maker. In this way, the power conditioning system is internally self-sufficient although slaved to the master control. Status information provided to the master control will be primarily for the purpose of cycle sequencing and for confirmation of having satisfied specific requests, e.g., an indication that the accel switch has applied power to the ion source accelerator.

Beam Line Vacuum System

Although the use of a larger ion source implies a proportionately larger gas loading there are no immediate changes of any significance in the vacuum system of the LITE beam line. As shown schematically in Fig. 4, the present system is pumped with various combinations of oil diffusion pumps and LN_2 cooled titanium getter pumps. In order to ascertain the impact that the increased gas loading will have, a particle balance computer program (Ref. 6) was applied to the system shown in Fig. 4.

It can be shown that an ion source operating with the species fractions and gas utilization efficiency indicated in Table I requires a gas input of 0.33 torr-liters per amp-second or about 5 torr-liters per second at 15 amperes. As an ion beam is generated, 41 percent of the gas will enter the neutralizer as ions, and the remainder as cold effusing gas. Assuming a 15 keV beam, passage through the neutralizer will result in 35 percent of the gas load exiting the neutralizer as fast atoms and the balance as cold gas. Assuming a 350 cm focal length, beam spreading and aperturing will result in only 8.4 percent of the original gas load passing through the target plasma as fast atoms. If no interaction with the plasma occurs, essentially all of this remaining 8.4 percent will become cold gas after impact on the beam dump target. As the above indicated gas loads enter the various chambers thereby causing pressures to rise, effusion will occur through the various chamber apertures from each chamber to every other chamber resulting in a redistribution of the gas loads. At equilibrium there will be a flux of cold gas from every chamber in the system to every other chamber in the system with the relative flux magnitudes determined by a balance between the aperture to every other aperutre gas transfer functions and the effective pumping speed of each chamber. Shown in the following table (III) are the aperture diameters, distances between apertures and the center of the LITE target plasma, and the pumping speeds of each region. Shown in the subsequent table (IV) are the cold gas densities and pressures of all regions for the two ion source operating conditions shown in Table II. In generating Table IV, the titanium getter pump regions were assumed to have sticking coefficients of 0.3 (Ref. 7).

Table III

LITE Vacuum System Parameters

Region	Inter-Region Aperture Diameter cm	Distance To Target Plasma cm	Temperature °K	Pumping Speed liters/sec
1. Neutralizer			300	0
	15.00	313.7		
2. Neutralizer Chamber			300	1.47(4)
	14.24	266.5		
3. Turning Magnet Chamber			300	4.90(3)
	13.94	200.0		
4. 1st Differential Stage			300	1.47(4)
	12.66	166.7		
5. 2nd Differential Stage			77	5.46(4)
	11.46	91.7		
6. Experiment Chamber			77	6.21(5)
	10.27	16.7		
7. Plasma Region			77	9.57(3)
	10.00	93.3		
8. Dump Isolation Chamber			77	8.01(4)
	10.00	166.7		
9. Beam Dump Chamber			77	1.50(5)

Table IV

LITE Vacuum System Pressure Balance

		15 keV, 15 A Condition		27 keV, 30 A Condition	
	Region	Density #/cm^3	Pressure Torr	Density #/cm^3	Pressure Torr
1.	Neutralizer	1.32 (13)	4.11 (-4)	2.71 (13)	8.44 (-4)
2.	Neutralizer Chamber	5.35 (12)	1.67 (-4)	1.07 (13)	3.34 (-4)
3.	Turning Magnet Chamber	2.30 (12)	7.15 (-5)	4.61 (12)	1.44 (-4)
4.	1st Differential Stage	5.31 (11)	1.66 (-5)	1.07 (12)	3.32 (-5)
5.	2nd Differential Stage	5.66 (10)	4.53 (-7)	1.14 (11)	9.09 (-7)
6.	Experiment Chamber	3.45 (8)	2.76 (-9)	6.81 (8)	5.44 (-9)
7.	Plasma Region	4.70 (8)	3.76 (-9)	9.35 (8)	7.48 (-9)
8.	Dump Isolation Chamber	1.75 (9)	1.40 (-8)	3.30 (9)	2.64 (-8)
9.	Beam Dump Chamber	8.09 (10)	6.47 (-7)	1.53 (11)	1.23 (-6)

Table V

Cold Gas Streaming Incident on Target Plasma

	15 keV, 15 A Condition			27 keV, 30 A Condition		
Originating Region	Streaming Flux #/sec	Streaming Flux Density #/sec-cm^2	Stream Gas Density #/cm^3	Streaming Flux #/sec	Streaming Flux Density #/sec-cm^2	Stream Gas Density #/cm^3
1	1.82 (16)	2.32 (14)	1.10 (9)	3.73 (16)	4.75 (14)	2.26 (9)
2	1.10 (16)	1.40 (14)	6.67 (8)	2.21 (16)	2.81 (14)	1.34 (9)
3	4.12 (15)	5.25 (13)	2.50 (8)	8.27 (15)	1.05 (14)	5.02 (8)
4	9.03 (14)	1.15 (13)	5.48 (7)	1.81 (15)	2.30 (13)	1.10 (8)
5	3.38 (14)	4.30 (12)	4.05 (7)	6.77 (14)	8.62 (12)	8.10 (7)
6	1.24 (14)	1.58 (12)	1.48 (7)	2.45 (14)	3.12 (12)	2.94 (7)
7	-	-	-	-	-	-
8	8.35 (12)	1.06 (11)	1.00 (6)	1.58 (6)	2.01 (11)	1.89 (6)
9	1.77 (14)	2.25 (12)	2.12 (9)	3.36 (14)	4.28 (12)	4.02 (7)
Total	3.49 (16)	4.44 (14)	2.15 (9)	7.08 (16)	9.01 (14)	4.37 (9)

Region 7 of the vacuum system (Fig. 4) represents the plasma region inside the confinement magnet. The density/pressure indicated there (Table IV) represents part of the cold gas load that can erode the plasma. The other part is due to the inter-region cold gas streaming mentioned above. Shown in Table V are the streaming fluxes and their associated densities originating from the various regions for the two ion source operating conditions.

The effect of the density of the cold gas stream (Table V) is to add to the effect of the equilibrium density (Table IV) as an eroding agent on the surface of the plasma. Comparing the total stream gas density to the gas density in the plasma region for each ion source condition reveals that streaming constitutes 82 percent of the total cold gas density in the plasma region.

The use of titanium gettering pumps represents a transient approach to pumping. The effective pump time of the vacuum system will be determined by region 5 (Table III) which has the largest gas load and the smallest pumping area. (Regions 2, 3, and 4 are diffusion pumped). If titanium replenishment is ignored and if the getter surface lifetime is assumed to be one monolayer (10^{16} #/cm^2) the pumping time of this region, and therefore of the overall system, is estimated to be 3.9 seconds. In view of the present operating times on LITE (order of 1 sec) it is felt that titanium getter pumping will suffice for the near term program.

Status and Schedule

The program for upgrading the injection capability of the LITE neutral beam line is in progress. The 15-cm ion source being supplied by ORNL has been completed and is presently undergoing electrode adjustment and testing. Delivery of the source to UTRC is expected by the end of this summer.

It is anticipated that all other components for the LITE beam line upgrade will be in-house by the end of September. If is further anticipated that the components will be assembled and/or integrated and the beam line ready for testing on LITE before the end of the calendar year.

Acknowledgments

The U.S. Energy Research and Development Agency (ERDA) assistance to UTRC for instituting the program for the LITE neutral beam line upgrade is greatly appreciated. ERDA support to ORNL for the design, construction and testing of the 15-cm ion source and ORNL assistance to UTRC in this endeavor are also greatly appreciated.

REFERENCES

1. Mensing, A. E. and T. L. Churchill: Neutral Beam Injection for LITE. Topical paper presented at the 17th Annual Meeting of the Division of Plasma Physics of the American Physical Society, St. Petersburg, Florida, Nov. 10, 1975.

2. Jernigan, T. C., et al: The DuoPIGatron Ion Source and Neutral Injection Heating in ORMAK. Topical paper presented at the Second Symposium on Ion Sources and Formation of Beams. Berkeley, California, October 22, 1974.

3. Stirling, W.L.: Private communication.

4. Tawara, H. and A. Russek: Charge Changing Processes in Hydrogen Beams. Reviews of Modern Physics, Vol. 45, No. 1, pg. 178, April 1973.

5. Barnett, C. F., et al.: Atomic and Molecular Collision Cross Sections of Interest in Controlled Thermonuclear Research. Oak Ridge National Laboratories, document ORNL-3113, revised, U.S.A.E.C. Contract No. W-7405-eng-26., August 1964.

6. Jong, R. A.: Self-consistent Background Gas Density Calculation - LITE Neutral Beam Line. UTRC 76-92, June, 1976.

7. Lewin G.: Fundamentals of Vacuum Science and Technology. McGraw-Hill, New York, pg. 148, 1965.

LIST OF FIGURES

ORNL 15 cm DUOPIGATRON SOURCE

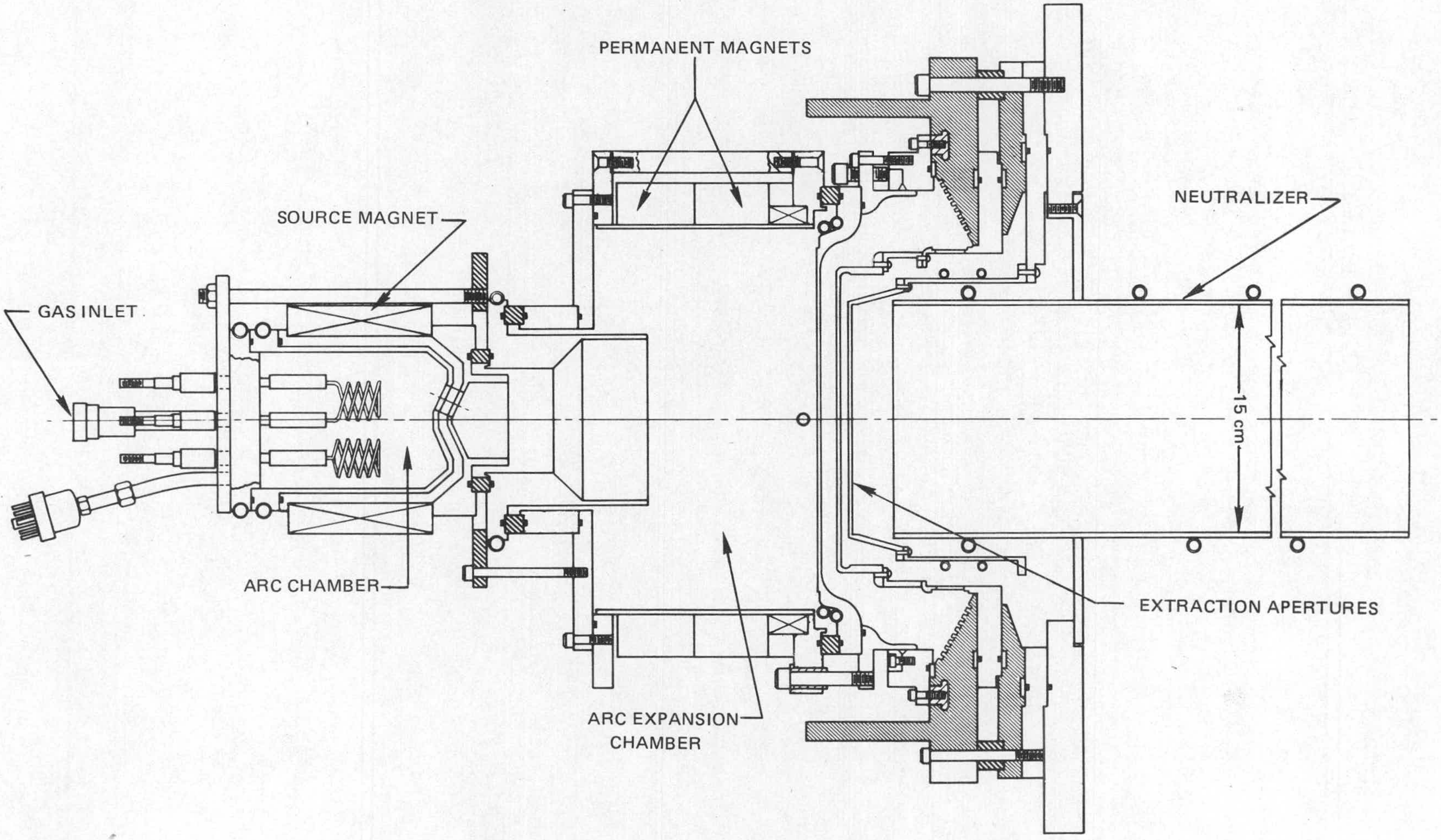

76–06–54–1

FIG. 1

FIG. 2

LITE NEUTRAL BEAM

CURRENT DENSITY PROFILE
AND
TOTAL CURRENT WITHIN RADIUS

15 KeV, 15A ION SOURCE
100 CM NEUTRALIZER

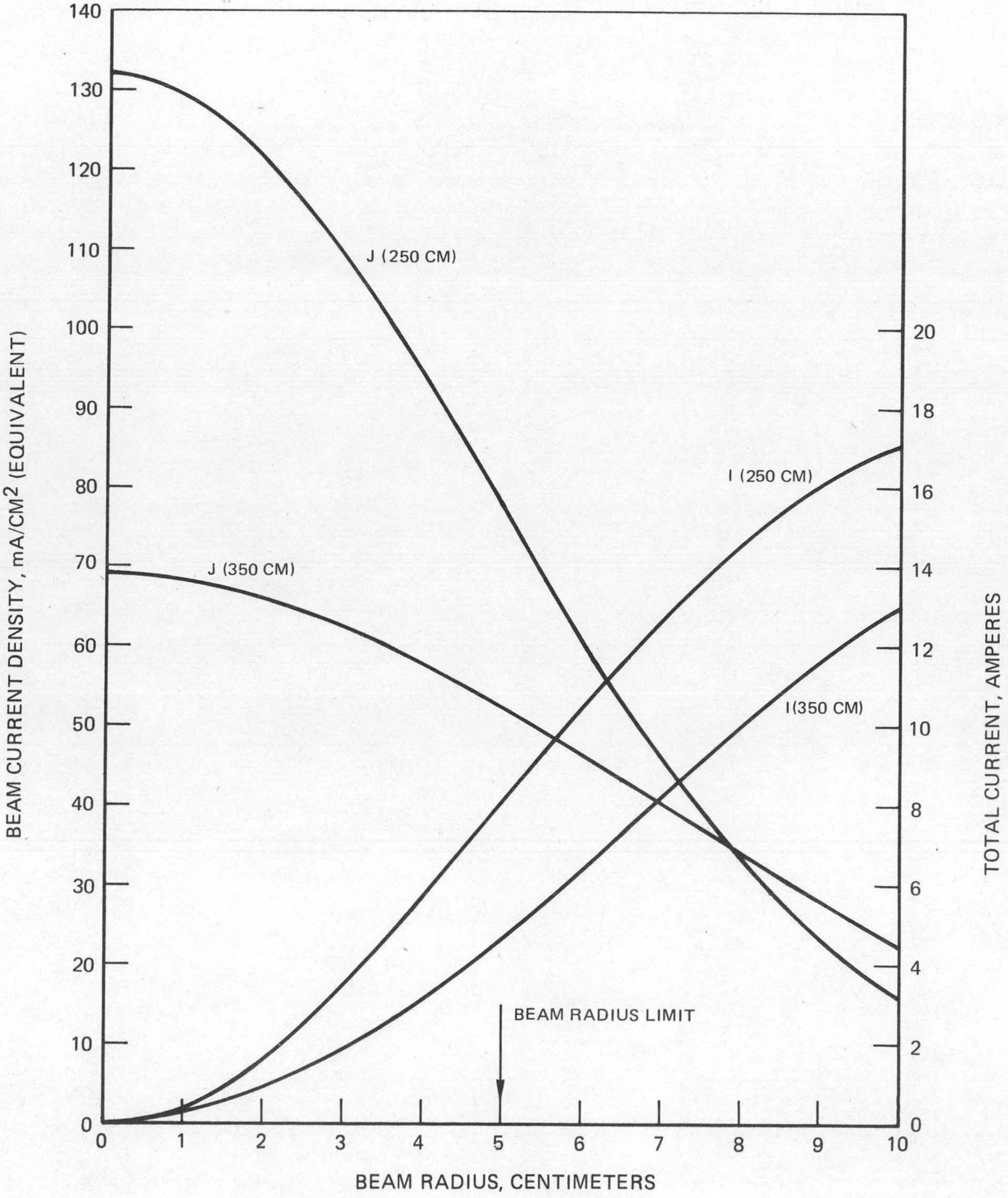

76—06—113—1

NEUTRAL BEAM INJECTOR POWER CONDITIONING SYSTEM

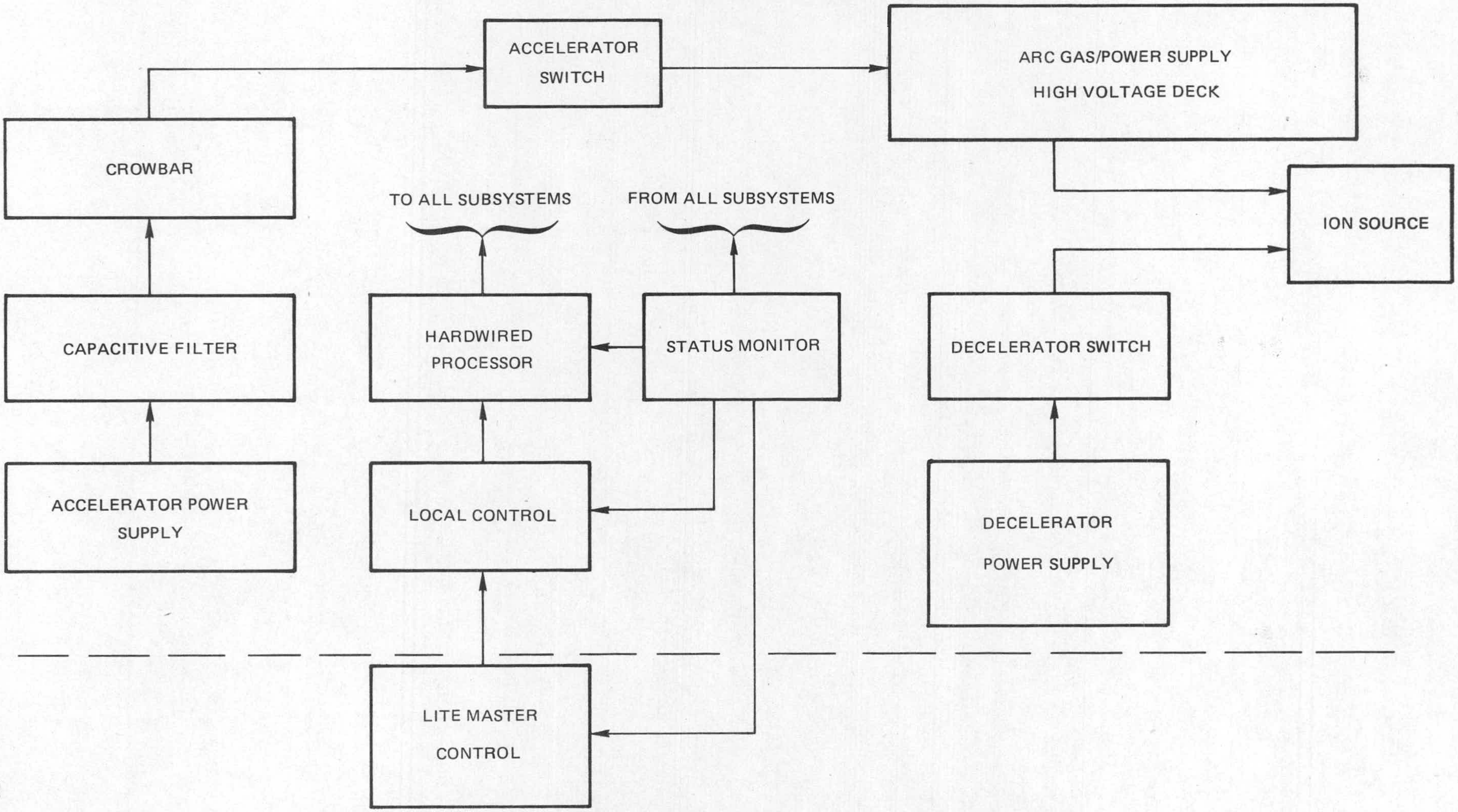

FIG. 3

76–06–54–2

LITE VACUUM SYSTEM

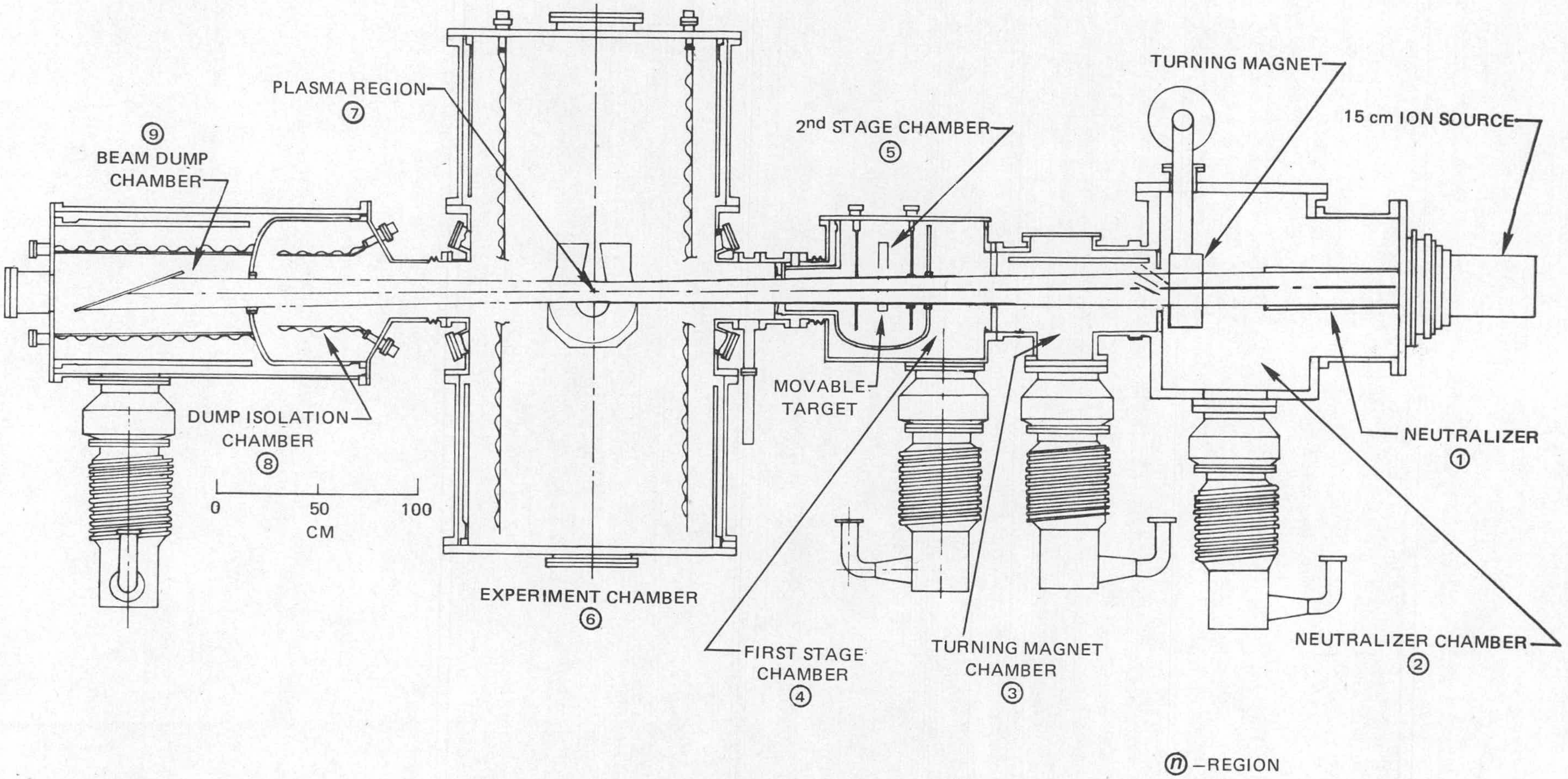

76–06–100–1

FIG. 4